T2R2 東京科学大学 リサーチリポジトリ
Science Tokyo Research Repository

論文 / 著書情報
Article / Book Information

題目(和文)	金属間化合物および準結晶の格子欠陥と変形機構 : Fe[3]Ge、Fe-Mn-Si合金中のχ相、Al[13]Fe[4]ならびにAl[65]Cu[20]Fe[15]準結晶
Title(English)	Lattice defects and deformation mechanism of intermetallics and quasicrystals : Fe[3]Ge, χ phase in Fe-Mn-Si alloy, Al[13]Fe[4] and Al[65]Cu[20]Fe[15] quasicrystals
著者(和文)	宮崎信弥
Author(English)	Shinya Miyazaki
出典(和文)	学位:博士（工学）, 学位授与機関:東京工業大学, 報告番号:甲第6510号, 授与年月日:2006年3月26日, 学位の種別:課程博士, 審査員:熊井真次
Citation(English)	Degree:Doctor of Engineering, Conferring organization: Tokyo Institute of Technology, Report number:甲第6510号, Conferred date:2006/3/26, Degree Type:Course doctor, Examiner:
学位種別(和文)	博士論文
Type(English)	Doctoral Thesis

Powered by T2R2 (Science Tokyo Research Repository)

G2005
M

TOKYO INSTITUTE OF TECHNOLOGY

Lattice defects and deformation mechanism of intermetallics and quasicrystals: Fe_3Ge, χ phase in Fe-Mn-Si alloy, $Al_{13}Fe_4$ and $Al_{65}Cu_{20}Fe_{15}$ quasicrystals

A Dissertation
for the degree of
Doctor of Engineering
Field of Materials Science and Engineering

by
Shinya MIYAZAKI

2005

Contents

Chapter 1 General Introduction

1.1. Back Ground 1
1.2. Aim of this Study 2
1.3. Outline of the Present Thesis 4
References 5

Chapter 2 Experimental Procedures

2.1. Special Methods for the Examination of Hardly Deformable Materials 7
2.1.1. Use of composite specimens 7
2.1.2. Semi-in-situ compression tests 7
2.2. On the Structural Analysis of the Intermetallics and Quasicrysatals 8
2.2.1. Diffraction conditions and imaging 9
2.2.2. Use of Convergent Beam Electron Diffraction (CBED) in Burgers vector analyses 9
2.2.3. Use of CBED in determining crystal structure 10
References 11

Chapter 3 Dislocation Motion on Octahedral and Cube Planes in Fe_3Ge Polycrystals

3.1. Introduction 13
3.2. Experimental Procedures 14
3.3. Experimental Results 15
3.3.1. Stress strain curves 15
3.3.2. Dislocations in as-annealed specimens 16
3.3.3. Dislocations introduced by bulk deformation 18
3.3.3.1. Deformation at 300K 18
3.3.3.2. Deformation at 700K 19
3.3.4. Dislocations introduced by semi-in-situ experiments 21
3.4. Discussion 22
3.4.1. Thermally activated dislocation motion 22
3.4.2. {001} slips at a low temperature 23
3.4.3. {001} slips at a high temperature 25
3.5. Conclusions 27
References 28

Chapter 4 Identification of χ Phase in Fe-Mn-Si Based SMA and the Estimation of Its Strength

4.1. Introduction · · · · · 55
4.2. Experimental Procedures · · · · · 55
4.2.1. Specimen preparations · · · · · 55
4.2.2. TEM observations · · · · · 56
4.3. Experimental Results · · · · · 57
4.3.1. TEM observations · · · · · 57
4.3.1.1. Non-deformed specimens · · · · · 57
4.3.1.2. Annealed at 1073 K after hammering · · · · · 58
4.3.1.3. Annealed at 1173 K after hammering · · · · · 58
4.3.1.4. Annealed at 1073 K before and after hammering · · · · · 58
4.3.1.5. As deformed specimen by hammering · · · · · 59
4.3.2. Crystal structure of the hardly deformable domains · · · · · 59
4.3.3. Semi-in-situ experiments · · · · · 60
4.4. Discussion · · · · · 61
4.4.1. On the formation mechanism of the χ phase domains · · · · · 61
4.4.2. Stress concentration at the χ phase domain · · · · · 62
4.5. Conclusions · · · · · 63
References · · · · · 65

Chapter 5 Plastic Deformation of Al-$Al_{13}Fe_4$ Thin Foils at Room Temperature

5.1. Introduction · · · · · 81
5.2. Experimental Procedures · · · · · 82
5.3. Experimental Results and Discussions · · · · · 83
5.3.1. Atomic structure of $Al_{13}Fe_4$ · · · · · 83
5.3.2. Dislocations and planner faults induced by heat treatments · · · · · 84
5.3.3. Deformation at 300K · · · · · 85
5.4. Conclusions · · · · · 87
References · · · · · 88

Chapter 6 Dislocation Generation and the Motion in a Monoclinic $Al_{13}Fe_4$ at 300~873K

6.1. Introduction · · · · · 100
6.2. Experimental Procedures · · · · · 100
6.3. Experimental Results · · · · · 102
6.3.1. Deformation at 300 K with Al_2O_3 particles · · · · · 102

6.3.2. Deformation at 473 K · 103
6.3.3. Deformation at 673 K · 104
6.3.4. Deformation at 873 K · 104
6.4. Discussion · 106
6.4.1. The plasticity detected prior to crack by semi-in-situ experiments · · · · 106
6.4.2. The sear systems in the monoclinic $Al_{13}Fe_4$ · · · · · · · · · · · · · 107
6.4.3. Temperature dependence and atomic diffusion · · · · · · · · · · · · · 109
6.5. Conclusions · 109
References · 111

Chapter 7 Plasticity of an $Al_{65}Cu_{20}Fe_{15}$ Quasicrystal Embedded in Al_2Cu
7.1. Introduction · 132
7.2. Experimental Procedures · 132
7.3. Experimental Results and Discussions · · · · · · · · · · · · · · · · · · 133
7.3.1. Non-deformed quasicrystals · 133
7.3.2. Deformation at 650K and 550K · 134
7.3.3. Room temperature deformation · 135
7.4. Conclusions · 135
References · 136

Chapter 8 Summary and Conclusions · · · · · · · · · · · · · · · · · · · 146

Chapter 1

General Introduction

1.1. Back Ground

Substances composed of two or more metallic elements are called 'Alloy.' Among them, compounds having structures with atoms located in ordered positions are called 'Intermetallic compound (IMC).' There are many IMCs classified to a relatively simple structure to extremely complicated ones. Fig. 1-1 (a) shows atomic locations in an $L1_2$-type compound as an example of a simple IMC, which is based on a fcc structure. Atoms A are located at corners of the fcc lattice points and atoms B are located at face center positions.

Brief explanation about deformation of the simple IMC of $L1_2$ is given as follows. Plastic deformation of metals is usually achieved by glide motion of dislocations on particular shear planes composed of densely packed atomic sites. Minimum magnitude of shear vector **b**, the Burgers vector, must be one of translational vectors if the crystal retain the same structure after deformation. In case of pure fcc metals such as Al, Cu, Au, etc., the minimum translational vector is a/2<110>. On the other hand, the translational vector in $L1_2$ must be twice of the a/2<110> and is a<110> as shown by an arrow in Fig. 1-1 (a).

Glide resistance for dislocation motion is generally attributed to a Peierls stress in absence of other obstacles. The stress is written in the form of exp(-h/b) by use of the plane spacing h and the magnitude of the Burgers vector b=|**b**|, according to the two dimensional model of the Peierls-Nabarro force [1]. It is clear that a small increase in **b** leads to a large increase in slip resistance and vice versa for the plane spacing as they are given in the exponent. However, in the recent studies of computer simulation, it has become apparent that the Peierls stress is determined by the atomic arrangement in the dislocation core: a planar core structure gives a small resistance against dislocation motion, whereas the core spread into non planar structure gives a large resistance [2]. Moreover it is well known that the elastic anisotropy and hence the elastic property of the material elements alters the strength notably focused on even in the simple $L1_2$ compounds [3].

In general, temperature dependence of the strength arises due to thermally activated overcoming of Peierls-Nabarro stress and/or other obstacles. In the case of $L1_2$ compound, the temperature dependence is divided in to three stages depending on the operation of <110> {111}, <112> {111} or <110> {001} types of slip systems [2]. Such a property is essentially governed by a dislocation core structure and is strongly dependent on the elements composing the $L1_2$

structure. Another important aspect of the plastic deformation is closely related to generation or multiplication of dislocations under an external stress. One of the subject in this study is focused on this question.

Next subject is concerned with plastic deformation of an $Al_{13}Fe_4$ IMC having a more complicated structure as shown in Fig. 1-1 (b). A unit cell is composed of 102 atoms [4][5] classified into 6 groups according to (13 Al + 4 Fe)×6. The minimum translational vector is [010] and its magnitude is about 0.81 nm as shown by an arrow in the figure. It is known that crystals having a larger Burgers vector than 0.5 nm show no ductility under usual deformation. Such a dislocation with a large Burgers vector must be dissociated and the mechanism of dislocation motion must be complex.

Although some hardly deformable materials become ductile in high temperature region by the help of atomic diffusion [6] [7] [8] [9], it is not known if such a crystal would deform by dislocation glide at a low temperature. There has not been any report which has attempted to reveal the low temperature deformation of the $Al_{13}Fe_4$ IMC.

Another intermetallic compound examined in this study is a bcc based IMC introduced into a FeMnSi SMA (shape memory alloy) in the course of development of a stronger SMA [10] [11]. The new IMC introduced in a Fe-Mn-Si-Cr-V-N alloy by hammering and heating will be analyzed by a microdiffraction method [12] [13] and its strength will be examined by the semi-in-situ method developed in this study. It is hoped that dislocation glide might be induced at a low temperature by application of a large stress if the $Al_{13}Fe_4$ and the bcc based IMC are protected from breaking apart.

In view of the absence of crystal periodicity in three dimensional space, a quasicrystal of $Al_{65}Cu_{20}Fe_{15}$ is another interesting material to be studied with special interest on the plastic deformation at a low temperature. The structure is typified by existence of periodicity in higher dimensional space [14]. Atomic sites in real space are, therefore expressed in terms of projection from the higher dimensional space. It is then questioned how the quasicrystal deforms in absence of periodicity by dislocation motion. Especially, plastic deformation at a low temperature is believed to be difficult without atomic diffusion. It is hoped here to get some insight into the deformability of such an alloy with a rather small Burgers vector defined in the higher dimensional space but without having normal crystalline periodicity.

1.2. Aim of This Study

It has been well known that any hardly deformable material including ceramics can be treated as a ductile material at sufficiently high temperatures. Such ductility is usually brought about in association with atomic diffusion. Among them the IMCs composed of metallic

elements are believed to deform by dislocation motion, where local phase change takes part in either to assist or retard the motion. At low temperatures, however, atomic diffusion does not affect the dislocation motion and plastic deformation must be governed totally by glide motion of dislocations. It is a key point in this study to introduce dislocations and let them glide before breaking the hardly deformable materials in absence of diffusion. For this purpose special experiments are designed so as to apply a large stress without breaking a specimen. Observation of the as-deformed microstructures, then lend a tool to visualize the mechanism of dislocation glide in a hardly deformable material.

In the past, very limited number of studies have been attempted for the purpose of clarifying the mechanism of dislocation glide in hardly deformable materials. For example, high speed deformation at room temperature enabled one to observe a group of dislocations introduced in $Al_{13}Fe_4$ [15]. In the high speed deformation, however, temperature raise during deformation is often questioned and the diffusionless deformation can be achieved only by special experimental set up as described later. Wollgarten *et al.* examined an $Al_{70}Pd_{20}Mn_{10}$ quasicrystal deformed by a Vickers indenter and subsequently thinned down to a thin foil for TEM observation just beneath the indentation mark [16]. Although use of a Vickers indenter is a useful method to apply a large stress, the applied stress is not simple under the indenter. It is important to know the magnitude of the applied stress upon comparison of the results of different types of hardly deformable materials.

Compression of a foil specimen for TEM observation is quite useful in estimating the stress and at the same time in protecting a specimen from breaking apart as it will become evident shortly. Thus, one of the purposes in this study is to develop a method to deform a specimen at a high stress level without breaking it and to introduce dislocations into such a specimen at a low temperature. The method is, of course, immediately applicable to a ductile material without difficulty. It is a kind of in-situ observation giving compression repeatedly at outside of a TEM, and is called "semi-in-situ deformation test" in this thesis.

Motivation of the present study is essentially based on the belief that any crystalline material must deform by glide motion of a dislocation at any temperatures, since a dislocation is defined as the moving front of the atomic displacements involved in the deformation. Once a proper method is established, aim of this study can be given in more specific manner as described later. The hardly deformable materials focused here are Fe_3Ge, χ-phase in Fe-Mn-Si based SMA, $Al_{13}Fe_4$ in Al and an $Al_{65}Cu_{20}Fe_{15}$ quasicrystal in Al_2Cu, as briefly described in 1.1. Cause of the non-deformability is expected to be quite different among the four materials.

1.3. Outline of the Present Thesis

In chapter 2, experimental procedures, for examining the hardly deformable materials are give with special interest on the four types of crystals including an icosahedral quasicrystal. The "semi-in-situ deformation test" is described together with the brief introduction of the methods of structural analyses achieved by using a 1000 kV HVEM (high voltage electron microscope) and a 200kV TEM.

In chapter 3, results of Burgers vector analyses are presented based on the CBED observations and exclusive operation of a cube slip is confirmed in deformed Fe_3Ge. The unique property of the absence of normal temperature dependence in this particular IMC is discussed in conjunction with the <112>/3 dislocations responsible for the $L1_2 \Leftrightarrow D0_{19}$ phase change.

In chapter 4, the crystal structure of χ phase in a Fe-Mn-Si-Cr-V-N SMA is determined by micro-diffraction method. Then, micro structural analysis is made on the SMA specimen containing the hardly deformable χ phase, before and after thin foil compression. Strength and deformation mechanism of the bcc based complex IMC is discussed in terms of generation and motion of dislocations.

In chapter 5, plasticity of Al-$Al_{13}Fe_4$ composite is examined at 300 K by HVEM. Shear deformation in the monoclinic $Al_{13}Fe_4$ is focused in the semi-in-situ compression of a thin foil specimen.

In chapter 6, dislocation generation in $Al_{13}Fe_4$ as well as the motion under a high external stress is examined and the deformation mechanism is discussed on the bases of structural and shear system analyses.

In chapter 7, $Al_{65}Cu_{20}Fe_{15}$ quasicrystals surrounded by Al_2Cu are examined on the specimens non-deformed, deformed at room temperature and at intermediate temperature. The icosahedral quasicrystals of $Al_{65}Cu_{20}Fe_{15}$ are shown to be deformable by dislocation motion according to TEM observation. The results are compared with those reported in literatures after deformations near the melting temperature.

In chapter 8, "General conclusions," new findings obtained by plastic deformation of hardly deformable materials are reviewed and the characteristic features are summarized on the ground of dislocation motion and multiplication.

References

[1] F. R. N. Nabarro: Theory of Crystal Dislocations (Oxford Univ. Press, 1967).

[2] Yamaguchi and Umakoshi, Progress in Materials Science **34** pp. 1 (1990).

[3] M. H.Yoo, Scripta Metall. **20** 915 (1986).

[4] P. J. Black, Acta Crystal. **8** 43, 175 (1955).

[5] J. Grin, U. Bukhardt and M. Elluner, Zeitshrift fur Kristallographie, **209** 479 (1994).

[6] B. N. Dey and W. R. Tyson, Phys. Stat. Sol. (a) **9** 215 (1972).

[7] L. Bresson and D. Gratias, J. non-crystalline Solids **153-154** 468 (1993).

[8] A. Inoue, Y. Yokoyama and T. Masumoto, Mat. Sci. Eng. **A 181-182** 850 (1994).

[9] T. Shibuya, T. Hashimoto and S. Takeuchi, Jpn. J. Appl. Phys. 29 **L349** (1990)

[10]A. Sato, H. Oonishi, Y. Yamaguchi, S. Kumai, T. Maruyama and H. Kubo, Proceedings of TMS annual meeting; Electron Microscopy: Its Role in Materials Science (Edited by J. R. Weertman, M. Fine, K. Faber, W. King and P. Liaw, 2003) p. 183.

[11] Y. Yamaguchi, S. Miyazaki, S. Kumai and A. Sato, Phil. Mag. submitted to publication (2005).

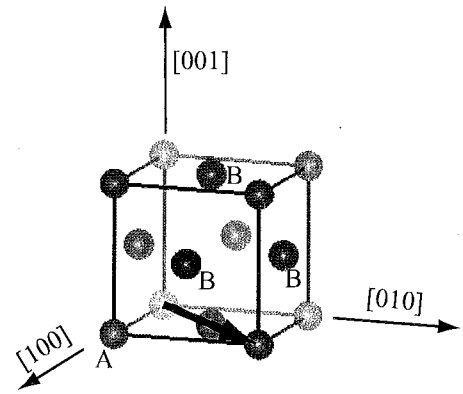
[12] J. P. Morniroli, and J. W. Steeds, Ultramicroscopy **45** 219 (1992)

[13] A. Redjaïmia and J. P. Morniroli 1994, Ultramicroscopy **53** 305.

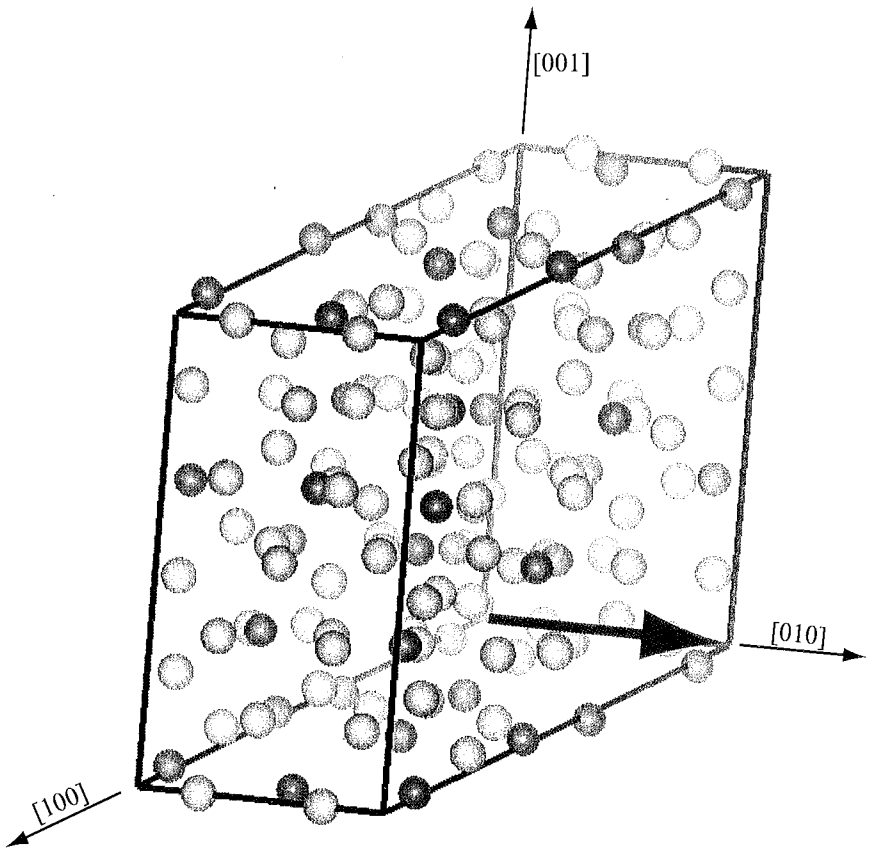
[14] V. Elser, Acta Cryst. **A 42**, 36 (1986).

[15] N. Yoneyama, K. Mizoguchi, S. Kumai, A. Sato and M. Kiritani, Mat. Sci. Eng. **A 350** 117 (2003).

[16] M. Wollgarten, H. Saka and A. Inoue, **A 79** 2195 (1999).



(a)



(b)

Figure 1-1

Chapter 2

Experimental Procedures

2.1. Special Methods for the Examination of Hardly Deformable Materials

In order to examine the four materials of the present interest (χ phase domains in Fe-Mn-Si based SMA, Fe_3Ge, $Al_{13}Fe_4$, $Al_{65}Cu_{20}Fe_{15}$ quasicrystals), special methods were developed and used as described below. The use of the composite specimens and the development of semi-in-situ compression tests played the key roles in clarifying the shear mechanisms involved in the plastic deformation, otherwise not detected in these materials due to a fracture. The special methods were designed by considering the two points related to the generation and preservation of dislocations contributed to the plastic deformation simultaneously on each material.

2.1.1. *Use of composite specimens*

One of the ways to introduce glide dislocations into a hardly deformable crystal is to compress the hard particles embedded in a ductile thin foil directly as reported previously [1] [2]. The dual phase materials examined in the previous studies are Al-Al_3Ni and Al-Al_3Ti, containing ordered alloy particles of $D0_{20}$ and $D0_{22}$ structures, respectively.

Specimens used in the present study are the composites containing proper sizes of the hardly deformable particles in ductile matrix, except in the case of Fe_3Ge. The matrixes are able to protect the particles from breaking apart during deformation. In the case when the hard particles are sheared off, the closest areas along the cracks containing various lattice defects were directly observable by the HVEM. However, the deformation structures introduced locally may not be examined after electro polishing since the electro polishing starts and proceeds preferentially in the heavily deformed regions at high energy states. This difficulty can be overcome by giving plastic deformation to a thin foil specimen transparent against electron beam for the observation. Hence, the HVEM shows the merit in the transparency. Then, the application of the semi-in-situ method to the present composite materials can elucidate the merit of the use of HVEM.

2.1.2. *Semi-in-situ compression tests*

One of the possible methods to detect the plastic deformation of a brittle material has been explored by Saka *et al.* [3]. In the study, the structure below an indentation mark is

examined by transmission electron microscopy (TEM) after thinning by a focused ion beam (FIB) milling. Despite that the ductility of a material generally increases in compression, compressive deformation is difficult to achieve dynamically during observation. Therefore, in-situ compression has not been attempted in the past. An in-situ experiment presented here differs from the usual methods of detecting dynamical processes in tensile tests. A semi-in-situ method developed here is a primitive but powerful way to examine the same area of a specimen repeatedly with intermittent mechanical treatments in between the successive observations. Although it is not easy to observe the same area repeatedly in the brittle materials, the present experiment of semi-in-situ compression using a foil specimen enables one to observe the state of proper deformation before complete break away due to the variation in the specimen thickness along the periphery of a hole introduced by electro polishing.

Meantime, various types of in-situ experiments have been advanced with development of the required design in manufacturing special holders to deform a thin foil during TEM observation [4] [5] [6] [7]. In these experiments, the single crystal specimens oriented at a desired orientation is usually required to set the proper diffraction condition in the limited degree of tilting freedom. Since the semi-in-situ compression method advanced in this study uses a double-tilt holder there is no limitation in the tilting angles.

A thin foil specimen jet-polished from one side and thinned down to perforation by final electrolytic polishing was set on a platform made of hard-steel/ZrO_2 as shown in Fig. 2-1. Proper load was applied at the bottom of a jet polished specimen through one of the variety of rods from a sharp tip to a rather flat tip, namely from the size of a Vickers indenter to more than one hundred μm in the tip diameter. Metallic foils made of Al or stainless steels were placed over the specimen to apply a stress uniformly. In some experiments, a sandpaper covered with SiC particles less than a few μm in the size was placed over a specimen for the two purposes; one is to avoid pasting of the specimen onto the apparatus, the other is to make a suitable stress condition in introducing dislocations into a brittle material without cracking. In the course of loading, the force was measured by a weighing device placed under the specimen stage. In some cases, when specimens were fractured into small peaces, they were collected and sandwiched by a double mesh for TEM observation.

In order to compress an aimed point accurately, a Vickers indentation machine or a drill press was used. The Vickers machine is especially advantageous to press specimen in pinpoint with an error of several micrometers. Deformation tests were performed in temperature range from RT (300K) to 873K. A hand made small furnace was used to surround the specimen and to raise the deformation temperature.

2.2. On the Structural Analysis of the Intermetallics and Quasicrystals

The materials focused in this study have a large unit cell [8] or even without having periodicity in the three dimensional physical space [9] [10]. Consequently, it is necessary to remind the points to be cautioned in analyzing the observations made in the following experiments. The special procedures used and the cautions made in the observations of the lattice imperfections in the rather unfamiliar materials are briefly described below.

2.2.1. *Diffraction conditions and imaging*

The TEM observations were made at the operating voltage of 1000 kV by using the H-1250S HVEM. A side entry type holder was used with the capability of double tilt by 45 degree. In the tilting experiment, use of a HVEM is especially beneficial in two major points. Firstly, the shift in electron beam by tilting is small even for a ferromagnetic material containing Fe. Secondly, as it is well known, the transmission is better and a thicker foil can be examined at the high accelerating voltage. It should be noted that the observable area increases roughly by a factor of 5 when the observable thickness increases by a factor of $(1000/200)^{1/2}$ upon increase in the accelerating voltage from 200 kV to 1000 kV. In order to analyze the observations unambiguously, a small objective aperture was used in both bright field and dark field microscopy so that contribution of the closely spaced diffraction spots can be differentiated in a quasicrystal as well as in the intermetallics of a large unit cell.

As mentioned above, the closely spaced diffraction spots tend to contribute to the imaging either by phase or by lattice distortion. In order to avoid the uncertainty due to the complex effects of the subsidiary electron waves, special care had to be exercised to minimize such an effect. One of the methods is to make the two beam condition by using a spot located not close to the incident beam and without accompanying the spots adjacent to it. In the analysis use of dark field microscopy was also advantageous to obtain better contrast from the defects in these complex crystals. Although application of a visibility criteria is difficult in the crystals of a large unit cell, it can be overcome by choosing proper diffraction condition. On the other hand, the principle of the criteria completely differs for the quasicrystal and may not simply be treated in the three dimensional physical space because of the lack of the crystal periodicity [11]. Then, the visibility criteria can be defined by addition of a component similar to an imaginary part (corresponding to the phase) for the three axes, resulting in the 6 dimensional analysis as explained later in chapter 7.

2.2.2. *Use of Convergent Beam Electron Diffraction (CBED) in Burgers vector analyses*

In the case of closely spaced dislocations or those attached to planner faults, the CBED method is some times quite useful [12] [13]. In this method, the local information about

the strain field can be obtained accurately, since the electron beam is focused into a small area with variety of the beam directions so that the diffracted beam contains the information of the local disturbance in the lattice through the Kikuchi lines. The convergent beams directed towards various angles from the small region is in contrast to the case of Kikuchi lines, which are formed by the interference of the scattered electrons from the rather large area in the usual selected diffraction. This method is applied in analyzing the dislocations in Chapters 3 and 7.

2.2.3. *Use of CBED in determining crystal structure*

The diffraction patterns obtained by the CBED method is also capable of determining the crystal structures but not of the local lattice disturbance mentioned above. The CBED method used here [14] utilizes the small angle convergent beams and is called a micro diffraction method. In this method, use of the convergent beams enables to confine the area of analysis as small as several tens of nm. Accordingly the area of the analysis can be reduced to less than 100 nm, being substantially smaller than the 500 nm attained usually by the selected area diffraction. The CBED method gives a reciprocal lattice with information in the three dimensional space composed of the zeros order Laue zone (ZOLZ), first order Laue zone (FOLZ) and so on. The information can be used to determine the unit cell, the crystal system, the point group, and the space group as it will be described in chapter 4.

References

[1] K. Yamashita, I. Fujimoto, T. Murakumo, S. Kumai and A. Sato, Phil. Mag. **A 80** 219 (2000).

[2] K. Yamashita, I. Fujimoto, S. Kumai and A. Sato, Mat. Tras. JIM **39** 824 (1998).

[3] H. Saka, A. Shimatani, M. Suganuma and M. Sprijadi, Phil. Mag. **A 82** 1971 (2002).

[4] U. Messerschmidt and F. Appel, Ultramicroscopy **1** 223 (1976).

[5] U. Messerschmidt and M. Bartsch, Ultramicroscopy **56** 163 (1995).

[6] G. Molenat, H. Rosher and D. Cailard, Mat. Sci. Eng. **A 258** 196 (1998).

[7] D. Baither, T. Pretorius and E. Nembach, Acta Mater. **51** 1229 (2003).

[8] P. J. Black, Acta Crystal. **8** 43, 175 (1955).

[9] T. Ogawa, J. Phys. Soc. Jpn. **54** 3205 (1985).

[10] J. W. Cahn, D. Shechtman and D. Gratias, J. Mat. Res. **1** 13 (1986).

[11] M. Wollgarten, D. Gratias, Z. Zhang and K. Urban, Phil. Mag. **A64** 819 (1991).

[12] M. Tanaka, J. Electron Microsc. **35** 314 (1986).

[13] R. Wang, Micron **31** 475 (2000).

[14] A. Redjaimia and J. P. Morniroli, Ultramicroscopy **53** 305 (1994).

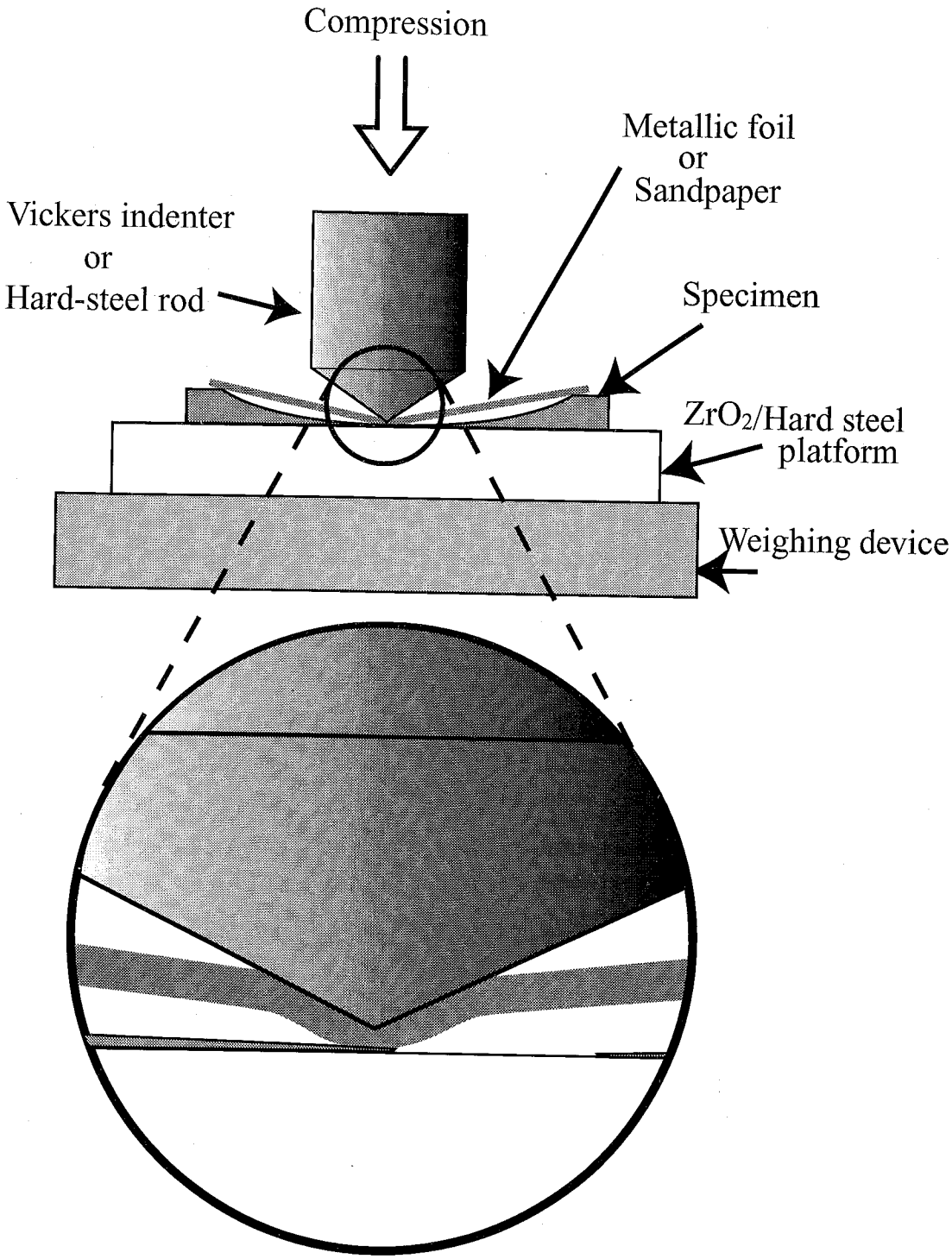


Figure 2-1

A compression device used in the semi-in-situ deformation of a thin foil specimen. Load was applied through a metallic foil/sandpaper to apply a stress uniformly/concentratively in a small area.

Chapter 3

Dislocation Motion on Octahedral and Cube Planes in Fe_3Ge Polycrystals

3.1. Introduction

A stoichiometric Fe_3Ge is known to adopt two types of structures; $L1_2$ below 973 K and $D0_{19}$ between 973 and 1395 K [1]. Strength of this alloy exhibits monotonic decrease with increase in temperature [2] [3] [4] [5] [6]. It differs from the well known other $L1_2$ alloys which exhibit positive (anomalous) temperature dependence due to thermally activated cross slip from {111} to {001} [7] [8] [9], the cross slip coupled with elastic anisotropy [10] [11], the cross slip coupled with dislocation climb [12] and exhaustion of mobile dislocations [13] [14] [15] [16] [17] [18] [19] [20] [21] [22], governed by Kear-Wilsdorf mechanism [23]. The origin of the cross slip has commonly been attributed to the structural change in the antiphase boundary (APB) [24]. On the other hand, the unique temperature dependence of the monotonic decrease in Fe_3Ge has been attributed to the operation of cube slips in a wide temperature range [3] [4] [5] [6]. It is based on the instability of APB (antiphase boundary) on {111} plane [25] and non-planner core of the <112>/3 dislocation on a {111} plane [26] [27] [28] bounding the super intrinsic stacking fault (SISF). On the other hand, another report discusses the instability of the $L1_2$ with respect to the $D0_{19}$ to explain the positive or negative temperature dependence [2] [29]. The origin of the monotonic temperature dependence in Fe_3Ge has been discussed mostly on the ground of individual dislocation motion and extensive review has been given on this subject [30].

There is, however, an issue to be examined by transmission electron microscopy (TEM). One problem encountered in the earlier studies is the difficulty in preparing the $L1_2$ ordered Fe_3Ge of a single phase since the $D0_{19}$ phase domains remain even after long period of annealing at 873 K below the $D0_{19} \rightarrow L1_2$ transformation temperature [31] [32]. The presence of the $D0_{19}$ phase leaves ambiguity in describing the strengthening mechanism of the $L1_2$ ordered Fe_3Ge. It is aimed in the present study to clarify the effects of $D0_{19}$ phase on the plastic deformation of Fe_3Ge by minimizing the residual $D0_{19}$ phase.

As it has been well known in the usual ductile metals, generation of dislocations play an important role in determining the early stages of stress strain behaviors [33]. However, even if the material is ductile to some extent, generation of the dislocation is likely to be affected by the presence of the other phase in the dual phase $L1_2$-$D0_{19}$ of Fe_3Ge focused in this Chapter.

Fortunately, the $L1_2$ ordered Fe_3Ge is sufficiently ductile and the present method of semi-in-situ compression of a thin foil specimen is expected to be promising in examining dislocation generation and the motion, since the compressive stress can be applied locally at a pin point by avoiding the influence of the surrounding $D0_{19}$. A major point focused in this study is the dislocation generation on cube planes, the subsequent motion and their multiplication.

3.2. Experimental Procedures

Fe_3Ge polycrystals were prepared by melting 3 parts of 99.9 % pure Fe and one part of 99.999 % pure Ge in an alumina crucible in Ar gas atmosphere. The melt mixture was solidified in a mold made of Cu so that the ingot could be cooled rapidly from the melting point [34]. In this way, homogeneity of the element distribution could be improved so as to reduce the amount of $D0_{19}$ phase in the final stage of heat treatments. The ingot was cut into rectangular pieces of 2.0 x 2.0 x 5.0 mm^3, vacuum-sealed, homogenized at 1273 K for 24 h and furnace-cooled. The homogenized specimens of $D0_{19}$ phase were finally annealed at 873 K for 672 h to let the $D0_{19}$ transform to $L1_2$. The surface morphology was examined by optical microscopy on a specimen polished electrically at 223 K in a mixture of 1 part of perchloric acid and 20 parts of ethyl alcohol. The rapid cooling by a Cu mold was effective to eliminate the $D0_{19}$ phase of observable size as examined by an optical microscope. These specimens are called "A" and used for both bulk and semi-in-situ deformation.

Some of the specimens solidified in an alumina crucible were also used for comparison. These specimens contained residual $D0_{19}$ phase (domains) of 10~100 μm in diameter and a few % in volume fraction even after annealing at 873 K for 672 h. The ingot was cut into either 2.7 x 2.7 x 6.0 mm^3 or 0.8 x 0.8 x 1.5 mm^3 to see size effect on the strength in the presence of the $D0_{19}$ domains. The large and small specimens are called "B" and "C", respectively. The strength is expected to vary from specimen to specimen for C due to fluctuation in the amount and orientation of the dispersed $D0_{19}$ domains.

Foil specimens for electron microscopy were prepared from both of the ingots cooled rapidly in Cu mold (A) and solidified at a slower cooling rate in an alumina crucible (B). The electrical polishing condition was same as that adopted for surface observation. In order to examine deformation behaviors repeatedly in the same area under the same diffraction condition, semi-in-situ compression tests were made on the foil specimen prepared by electrical jet polishing to leave one side of the surfaces flat. Figure 2-1 shows a simple device used for the semi-in-situ compression tests. A few layers of Al foils were placed over the specimen a foil sample to apply a stress evenly. Heavy deformation imposed on the Al foils enabled the TEM

foil specimen to deform gradually by dislocation motion under a controlled load. The area force acting on the specimen was measured by a device placed below the specimen platform as shown in Figure 2-1. Then, the stress was estimated from the area of a dimple mark formed on the deformed specimen as well as from the flattened area on the backside of the pressed Al foil .

In the semi-in-situ experiments, a deformed Fe_3Ge foil was observed repeatedly after increasing the load step by step, so that generation of dislocations could be detected successively in the same areas. Specimens deformed in bulk were also sliced perpendicular or inclined by 45° to the compression axis, so as to make the geometry same for the bulk and the semi-in-situ experiments or to increase a possibility of finding wider slip planes. The deformed specimen foils were examined by stereo microscopy and the equal thickness contour method [35] using a H-1250S at 1000 kV, and by a convergent-beam electron diffraction (CBED) method [36] [37] using a JEM-2010 at 200 kV. Burgers vectors could thus be determined unambiguously with three-dimensional information of the dislocation configurations. Use of HVEM was especially advantageous in the tilting experiments of the ferromagnetic Fe_3Ge, since a thicker region can be examined with good resolution and beam deflection due to Lorenz force was much smaller in HVEM.

3.3. Experimental Results

3.3.1. *Stress strain curves*

Stress strain curves for the bulk specimens B (2.7 x2.7 x 6.0 mm^3) were obtained at different temperatures and shown in figure 3-1(a). Strain rate sensitivity can be found on the flow stress change upon increase or decrease in the strain rate by a factor of 10. The slower base strain rate was set at $1.4 \times 10^{-4} s^{-1}$. The rapid work hardening at a small strain can be attributed to the presence of $D0_{19}$ domains embedded in the $L1_2$ matrix. The contribution of the $D0_{19}$ phase is evidenced more clearly in the results of small specimens C (0.8 x 0.8 x 1.5 mm^3) in Figure 3-1(b). The large fluctuation in the stress level in the small specimens C (but not in the large specimens B) can be attributed to the variation in the volume fraction of the $D0_{19}$ domains from specimen to specimen, due to the relative coarsening in the domain size with respect to the specimen. The stress level is lowest for the specimens A in which the amount of $D0_{19}$ phase was minimized by rapid cooling and is nearly same as the lowest value of the small specimens C.

The yield strength defined at 0.2 % offset strain is plotted against test temperature in figure 3-2 where the data used are the lowest values for the small specimens C and the average values for the larger specimens B. Difference in the yield stress between the two is, however, not so distinct, implying that the residual $D0_{19}$ domains mainly contribute to the work hardening.

The yield stress of the $L1_2$ ordered Fe_3Ge is thus confirmed to decrease without exhibiting the positive temperature dependence which is usually observed in the other $L1_2$ intermetallics, being independent of the presence of $D0_{19}$ domains.

Furthermore, the temperature dependence curve is found to change from a concave down to a concave up shape at a higher temperature in Figure 3-2. Decrease in strain rate sensitivity with increase in test temperature up to ~500 K noted in Figure 3-1 (a) is natural trend in thermally activated dislocation motion and the curve is concave down below a critical temperature in Figure 3-2. As it is known in the theoretical analyses [38] [39] [40] [41] [42] the temperature dependence of the yield stress at a given strain rate can be regarded as a force-distance curve (stress-activation area curve) and usually shows a concave down curvature in a simple case. The concave up behavior appeared at a higher temperature may not be attributed to a simple mechanism. Thus, the sudden increase in strain rate sensitivity upon approaching the $L1_2 \rightarrow D0_{19}$ transformation temperature suggests transition in the mechanism of dislocation motion as discussed later.

3.3.2. *Dislocations in as-annealed specimens*

Figure 3-3 shows an example of the residual stacking faults corresponding to a $D0_{19}$ phase and dislocations in the same area of a specimen A annealed at 873 K for 672 h after the rapid solidification by a Cu mold. (a) is viewed nearly along the [001], (b) along the [101], and (c) and (d) along the $[1\bar{1}1]$. The surface normal, the beam directions and other geometrical information are given by a stereographic projection in Figure 3-3(e). In the figures (b), (c) and (d), it is clearly noted that the stacking faults are formed preferentially on one type of the $(\bar{1}11)$ planes running along the 10-16 O'clock direction in the upper right area and fewer along the 12-18 and 8-14 O'clock directions in the lower area. From the angle of ~71° between the $(\bar{1}11)$ and $(11\bar{1})$ planes viewed edge-on in (b), the fewer faults are judged to have been introduced after the $D0_{19} \rightarrow L1_2$ phase transformation. Namely, the dominant variant in the upper right area might have been introduced upon $D0_{19} \rightarrow L1_2$ phase transformation due to the incomplete operation of the (2/3) $<\bar{1}100>$ shears on the basal planes. Lack of shear systems in the $D0_{19}$ structure has been pointed out to retard the $D0_{19} \rightarrow L1_2$ transformation because of the incompatibility [31]. Production of the second and third variants of the {111} faults, which are energetically not favored in the $L1_2$ phase could have been introduced with expense of the elastic energy to release the incompatibility. The absence of the $(\bar{1}11)$ fault among the four possible variants in Figure 3-3 may then be ascribed to the absence of the relevant stress component.

In Figure 3-3, the **g** vectors of 200, $20\bar{2}$, $0\bar{2}2$ and $20\bar{2}$ are excited for (a), (b), (c) and (d), respectively. The contrast disappears when the **g** vector is parallel to the fault plane. Most of

the dislocations are stopped at {111} planes and aligned along the <110> intersections. The thermal APB's on {001} planes such as reported by Ngan *et al.* [4] were, however, not observed in this specimen. According to the visibility and the shear system geometry, the dislocations were identified to be mostly of either the <112> or <110> type as reported in the literature [3] [4] [5] [31]. For example, the Burgers vectors of the dislocations lying on the widest (111) planes marked by A~F in Figure 3-3 were determined to be $\pm[2\bar{1}1]/3$ for A and F, $\pm[011]/3$ for D and E, and $\pm[\bar{1}12]/3$ for B and C, according to the matching between the **g** • **b** values and the visibility as shown in Table 3-I. Here the magnitude of the Burgers vector of the <110> type was assigned with the knowledge of the earlier studies [3] [4] [5] [31]. The magnitude of the <112> type was confirmed as shown later by the equal thickness fringe method [35]. Since a small change in the deviation vector **s** from the exact Bragg condition alters the dislocation image [43], it was important to adjust the tilting angle to obtain a proper **s** without exciting the other **g** vectors. Another point to be cautioned is the residual contrast due to the edge component of **b**, which can be found by the dislocation directions given below the notations A~F in the Table 3-I. The results are given in the bottom low together with the dislocation types. Note that E showed residual contrast for **g** • **b** $=(022) \cdot [0\bar{1}1] = 0$ and the every images showed good matching with the **g** • **b** values.

Although dislocations A ~ E are similar to the ones reported in the literature [3] [4] [5] [31], the dislocation F in Figure 3-3 differs from the ones ever reported in the following points: (1) The dislocation line is not aligned along any of the <110> directions although it is straight. (2) The image of F is not of a single dislocation but has a dipole-like character with the same intensity as shown in Figure 3-3(a). According to the visibility shown in Table 3-I, it is judged to be composed of two superpartial dislocations $\pm[2\bar{1}1]/3$. They lie on two parallel {111} planes separated by several nanometers and the line contrasts are aligned along the $[\bar{1}21]$ direction. It is then postulated that the partial components of $\pm[\bar{1}01]/2$ and $\pm[\bar{1}21]/6$ separated from the $\pm[2\bar{1}1]/3$ will trap each other by forming an edge and a screw dipole segments along the $[\bar{1}2\bar{1}]$. Formation of such a dislocation dipole may have prevented the {111} faults to disappear.

The equal thickness fringe method [35] used here in determining the magnitude of the Burgers vector is described below. Figure 3-4 demonstrates jumps in thickness fringes induced by a <112>/3 partial dislocation. The beam direction is aligned nearly along the [001]. The dark field micrograph was taken by $\bar{2}20$ reflection lying on the shear plane of a partial dislocation with $\mathbf{b}=[2\bar{1}1]/3$. In this diffraction, the (111) fault attached to the partial dislocation was made invisible so that the jumps in the thickness fringes are visualized as shown in Figure 3-4. The Burgers vector of the dislocation at A satisfies

$$n=\mathbf{g} \cdot \mathbf{b}=(\bar{2}20) \cdot [2\bar{1}1]/3=-2, \qquad (1)$$

to give the jumps of 2 in the fringe.

On the other hand, the <110> type of dislocations generated at the corners of the intersecting {111} planes such as D in Figure 3-3(c) and E in Figure 3-3(a) are assigned as reaction products with the Burgers vectors of the <110>/3 as reported by Chen et al (1998). However, such a dislocation alone does not fit to the periodicity of the fcc lattice in the magnitude of the Burgers vector. It is, thus, confirmed that there are no perfect dislocations readily available for glide on either the {001} or {111} planes in the as-annealed specimen. Glide dislocations must be introduced by some means for macroscopic deformation to proceed in the $L1_2$ ordered Fe_3Ge. This point is focused in the following sections as to account for the observed stress-strain behaviors.

3.3.3. *Dislocations introduced by bulk deformation*

3.3.3.1. *Deformation at 300 K*

Figures 3-5(a), (b) and (c) are stereo pairs showing dislocation structures in a specimen A deformed at 300 K to 1.4 %. The geometry of the grain under observation is shown by a stereographic projection in (d). The surface normal of a thin foil sliced perpendicular to the compression axis is shown at the center and denoted by S(C) in Figure 3-5(d). The beam direction is aligned nearly along the [011], [143] and [010] with the operating **g** vectors, $200,1\bar{1}1$ and $\bar{2}02$ for (a), (b) and (c), respectively. Although (b) and (c) show the area shifted by several μm from (a), slip bands are the same ones extended from (a). The foil was tilted around the **g** vector mutually by 8~10° between the left and right side photographs. The slip plane traces indexed in the figure indicate projections of the intersection lines formed at the top surface of the foil.

Many dislocations A and B are introduced as groups on the (010) planes forming bands as marked by Ⓐ and Ⓑ in Figure 3-5(a). Gently curved dislocations C are also introduced on the isolated (010) planes. It is thus confirmed that plastic deformation of Fe_3Ge at 300 K is practically carried by cube slips as reported by Ngan *et al.* [3] [4] [5]. S in (a) is a stain mark remained at the top surface after electro-polishing and used as a marker to hold the viewing area in the tilting experiments. Burgers vectors of the dislocations lying on the (010) and (001) planes determined by visibility tests are listed in Table 3-II with judgment of the image matching given at the bottom row together with the dislocation types. The Schmidt factors are largest for the most highly populated dislocations of group A $[\bar{1}01]$ on (010) and group B [101] on (010) for the stress axis oriented along the S(C) in Figure 3-5(d). The magnitude of the Burgers vector was confirmed to be <110> by a CBED method as shown later.

Another important feature noted in Figure 3-5 is the generation of one type of dislocations

as a group on each band. It means that once a <110> dislocation is formed on a {001} plane, the multiplication is easy on the {001} plane. In the absence of perfect dislocations on either {001} or {111} planes in the as-annealed specimen (Figure 3-3), generation of a perfect dislocation on a {001} plane would play a critical role in continuing macroscopic deformation. Curved partial dislocations were also observed at the ends of the (111) stacking faults as shown by arrows in Figure 3-5(b). It is apparent from the sense of the bow out direction that they have contributed to eliminate the energetically unfavorable $D0_{19}$ phase under the applied stress. But the strain gained by the glide motion of the partial dislocations on the {111} planes must be limited by the amount of {111} faults corresponding to a $D0_{19}$ phase. In the regions ① and ② marked by double arrows, the <112> partial dislocations moved on the (111) and $(1\bar{1}\bar{1})$ planes and on the $(\bar{1}\bar{1}1)$ and $(\bar{1}11)$ planes are assumed to have reacted at the intersections. In Figure 3-5(c), the (010) planes on which both of the dislocations $[\bar{1}01]$ and [101] lie are taken nearly perpendicular to the beam direction and the $[\bar{1}01]$ and [101] are observed mutually orthogonal as pointed by double arrows corresponding to ① and ② in (b). They are assumed to be the sources of the cube slip dislocations. The area marked by white-broken-line squares in (b) and (c) is hypothesized to be the early stage structure of the origin of the glide dislocations A and B (Table 3-II) and will be examined later in more details by considering a possible dislocation reaction.

3.3.3.2. *Deformation at 700 K*

Figures 3-6(a) ~ (d) show a representative dislocation structure in a specimen B deformed at 700 K to 2.3 % by compression in bulk. Geometrical information of the grain under observation is shown by a stereographic projection in Figure 3-6(e). Note that this foil was sliced at an angle with respect to the compression axis. As the consequence, the (010) planes are cut by surfaces wider in this grain. The Figures 3-6(a) and (b) are stereo pairs viewed nearly along the [011] direction by operating the **g** vector $11\bar{1}$ for (a) and 200 for (b). Note that (a) and (b) are rotated mutually by 54.7° so that the **g** vector is aligned vertical for stereo microscopy. In contrast to 300 K, dislocations did not form a band structure along any of {001} planes. The figures (c) and (d) show the same area as (a) viewed nearly along the $[\bar{1}10]$ direction by operating the **g** vectors $11\bar{1}$ for (c) and 002 for (d). Upon examination of the geometrical factors, it must be noted that the $[\bar{1}10]$ beam direction in (c) and (d) is tilted by 60° from the $[01\bar{1}]$ in (a) and (b).

There are many superpartials on {111} planes accompanying stacking faults and the fault planes are marked by Ⓐ for (111) and Ⓑ for $(\bar{1}\bar{1}1)$. Some of the partials are curved such as at A_1 in Figure 3-6(a), showing that they have moved to eliminate the faults in similar way as observed after deformation at 300 K in Figure 3-5. Other partials are straight and directed

along <110> on a {111} plane as marked by A_2 and A_3 in Figure 3-6(a). The superpartials moved on the {111} planes are apparently split into partials of smaller Burgers vectors dividing the faults into narrow pieces as seen clearly in the faults Ⓐ in (a). The $(\bar{1}\bar{1}1)$ planes marked by Ⓑ are viewed nearly edge on in (a) and (b), and wider in (c) and (d) so that the partial dislocations B_1, B_2 ... become visible in the latter. The dislocation structures with the split configuration are similar in the two {111} planes Ⓐ and Ⓑ.

Various kinds of straight dislocations are recognized along the $[\bar{1}01]$ and $[10\bar{1}]$ directions corresponding to the intersections between $(\bar{1}\bar{1}1)$ and (111) planes and between $(\bar{1}\bar{1}1)$ and $(\bar{1}11)$ planes, respectively. An important feature that differs from 300 K is the introduction of finely distributed partials on {111} planes with weaker contrasts in comparison with <112>/3 partials shown in Figures 3-3 and 3-5. Some of the partials are shrunk into narrow pairs of <112>/3 superpartials on Ⓐ about to disappear as marked at A' in Figures 3-6(a) and (c). This explanation is supported by the visibility loss of the pair contrasts of A' upon slight change in the $1\bar{1}\bar{1}$ reflection in (c). Thus, in the absence of glide dislocations on the {111} planes, motion of the individual <112>/3 partials on {111} planes is assumed to have generated the <110>/2 partial dislocations on {001} planes as discussed later.

According to the stereomicroscopy shown in (a) and (b), some dislocations were identified to lie on a {001} plane or aligned along a low index direction. D is directed along the $[\bar{1}01]$ corresponding to the zone axis of $(\bar{1}\bar{1}1)$, (010) and (111) planes, E is directed along the [100] corresponding to the intersection between (010) and (001) planes, F is curved nearly on the (010) planes in (a), G is curved exactly on the (001) planes in (b), H is directed along [010] corresponding to the intersection between the (100) and (001) planes and I is directed along the $[\bar{1}10]$ corresponding to the zone axis of $(1\bar{1}\bar{1})$, (001) and (111) planes. Besides the dislocations mentioned above, there are curved dislocation images with small steps in the circled area at the right side bottom in Figure 3-6(a). Presence of these dislocations together with the dislocations F suggests that deformation at 700 K involves dislocation climb governed by atomic diffusion.

The Burgers vectors were analyzed on the basis of visibility as listed in Table 3-III. Geometrical information about the Burgers vectors, dislocation lines, slip planes and **g** vectors is given in Figure 3-6(e). The most highly populated dislocations G are curved on (001) planes with the Burgers vector of a <110> type as shown in Table 3-III. The dislocations F are curved nearly on the (010) planes but the Burgers vector [010] is perpendicular to the (010) planes. The faint contrasts of F in Figure 3-6(d) may come from the edge components under the Bragg condition of (002) • [010]=0 in Table 3-III. The <100> type of dislocations have been found after high temperature deformation in other $L1_2$ compounds [44] [45]. On the other hand the dislocations G with smooth contrast may be assigned as glide dislocations since the Burgers

vector $[\bar{1}10]$ lies on the (001) planes and the Schmidt factor is ~0.5 for the $[\bar{1}10]$ (001) as found in Figure 3-6(e). The change in the dislocation structure from the heterogeneous to the homogeneous one upon temperature raise must also be incorporated with the rapid decrease in the flow stress accompanying increase in the strain rate sensitivity (Figures 3-1 and 3-2). Absence of dislocations as a group and presence of the curved dislocations such as G lying on the (010) planes suggest that deformation at 700 K is also governed by cube slips but possibly involving atomic diffusion in the dislocation generation as discussed later.

3.3.4. *Dislocations introduced by semi-in-situ experiments*

In order to understand the effects of $D0_{19}$ phase remained as {111} faults on the operation of cube slips, a thin foil specimen was deformed using a simple apparatus shown in figure 2-1. Figures 3-7(a), (b), (c) and (d) show successive stages of plastic deformation observed in the same area by HVEM. The photographs were taken after loading to 6.0, 8.5 and 10.0 kg for (b), (c) and (d). All the figures were taken under the similar Bragg condition by use of a double tilt specimen holder. As the {111} faults corresponding to the $D0_{19}$ phase were distributed in fine scale as shown in Figure 3-3, the information obtained in Figure 3-7 should represent the general behavior of the dislocation generation and their motion. It is apparent that structural change has occurred dominantly between 8.5 and 10.0 kg, by dislocation motion on both {111} and {001} planes. Introduction of dislocations at the foil surfaces in the form of partials is obvious from the weak intensity of the individual dislocations. The yield stress of ~400 MPa estimated from the size of a dimple mark (Figure 2-1) is somewhat smaller due to stress concentration. In reality, deformation is not uniform in the beginning because of the non-uniformity in the surface. For example, the deformed area is concentrated at bottom part in (b) at 6.0 kg. Partial dislocations absent in (b) were, then, introduced in the center portion on the inclined {111} planes from the surfaces as shown by arrows in (c) at 8.5 kg. After increasing the load to 10,0 kg in (d), the partials introduced in (c) have expanded and new dislocations were created on both {111} and {001} planes at the surfaces. There is a clear tendency that dislocations are formed on the {111} faults in advance such as observed in (c) and later on the {001} planes at the intersections between {111}-{111} planes as marked by allows in Figure 3-7 (d). On the contrary, slip bands were never observed on {111} planes. Instead, the pre-existed {111} faults were wiped away rather slowly. This observation leads to a proposal that nucleation of a slip dislocation on a {001} plane plays a key role in the plastic deformation of the $L1_2$ ordered Fe_3Ge at 300 K as discussed later in more details.

Since CBED method is a simple way to determine the Burgers vector by use of defocused diffractions, the Burger vector of <110> type introduced in the semi-in-situ experiments was examined at 200 kV after loading to 10 kg as shown in Figure 3-8. Here, a defocused

diffraction taken from the small area marked by a circle in (a) is shown in (b). From the number of jumps on the dark and white lines in the defocused circles such as marked by faint lines, the Burgers vector was confirmed to be [101]. The jump along the line contrasts is, however, distorted due to splitting and quite different from the clear multiple jumps reported for a simple dislocation (Tanaka 1986). The shear systems operated in this semi-in-situ compression tests were thus confirmed to be the <110> perfect dislocations split on {001} planes in agreement with the results by Ngan *et al.* [3] [4] [5]. Then, the next question is to find out what are the critical processes relevant to the measured strength and the activation volume (v*).

3.4. Discussion

3.4.1. *Thermally activated dislocation motion*

The origin of the sudden drop in the strength upon approaching the transformation temperature in Figure 3-2 is discussed by analyzing the thermally activated dislocation motion.

By writing a strain rate $\dot{\varepsilon}$ as

$$\dot{\varepsilon} = \rho b v = A \exp(-G^*/kT), \tag{2}$$

the activation volume v* defined by

$$v^* = -\partial G^*/\partial \sigma \tag{3}$$

can be written as

$$v^* = kT/(\partial \sigma/\partial \ln \dot{\varepsilon}) \tag{4}$$

by use of equation (2) where ρ is the mobile dislocation density, b the magnitude of the Burgers vector, v the dislocation velocity, G* the activation energy for a dislocation to overcome an obstacle, k the Boltzmann constant, T the absolute temperature and σ the applied stress. The v* was calculated by use of equation (4) from Figure 3-1(a) and plotted against the yield stress in Figure 3-9. In the v*-σ plot, the decrease in the v* at a higher stress level is a typical behavior in a thermally activated dislocation motion (Orowan 1940, Basinski 1959, Schoeck

1965, Nabarro 1967, Mori and Kato 1981). Moreover, the rapid increase in v* at 600 MPa implies that a long-range stress must be superimposed on the thermally activated deformation. The sudden decrease in v* and the concurrent decrease in the stress level at high temperatures indicates a transition in the deformation mechanism. The results of Figure 3-9 suggests that the thermally activated deformation involves a long range stress which might be taken over by some other mechanism above a critical temperature.

At this point it is interesting to compare the dislocation structures introduced at 300 K and 700 K shown in Figures 3-5, 3-6 and 3-7. Glide dislocations were observed as groups in the {001} slip bands separated apart by 3 ~ 50 μm at 1.4 % strain after bulk deformation. Figure 3-5 shows an example of the closely separated bands. A similar band structure was confirmed by the semi-in-situ deformation at 300 K as shown in Figure 3-7. Deformation is, thus, controlled by successive generation of slip bands at special sites at a low temperature where v* exhibited usual stress dependence. On the other hand, in association with drastic decrease in v* and the stress level at a higher temperature, homogeneous slip was observed on {001} planes, for example, after deformation at 700 K, in Figure 3-6. The origin of the transition in v* is discussed in more details later on the ground of TEM observations.

3.4.2 *{001} slips at a low temperature*

Figures 3-10(a) and (b) are the areas surrounded by white-broken-line squares in Figures 3-5(b) and (c), respectively. The intersection between the $(11\bar{1})$ and (111) faults is viewed by operating the **g** vector $\bar{1}\bar{1}1$ for (a) and $\bar{2}0\bar{2}$ for (b) where the $(11\bar{1})$ faults are viewed nearly edge on in (a). The foil specimen was tilted by ~ 45° around the $[\bar{1}01]$ from (a) to (b). The geometrical information is given in Figure 3-5(d). Fresh dislocations are apparently generated at the intersection A shown by arrows in Figures 3-10(a) and (b). Interestingly, the dislocations are arranged to form a rectangular parallelepiped composed of <110> lines lying on {001} planes. The dislocations lying on a (010) plane are viewed widely in this beam direction. Other dislocations pointed by arrows in Figure 3-10(b) also lie on the flat (010) planes. These dislocations visible by $\bar{2}0\bar{2}$ in (b) are the same as the [101] dislocations observed in the band Ⓐ in Figures 3-5(a), (b) and (c). The [101] direction is parallel to the intersection between the (111) and $(11\bar{1})$ planes where the $(11\bar{1})$ faults visible in (a) are out of contrast in (b). It means that the [101] dislocations introduced at the intersection A marked in Figures 3-10(a) and (b) are of screw character. A dislocation reaction is conceivable as a consequence of elimination of the {111} faults by partial dislocation motion. The faint dislocation contrasts remained near the intersection may be of the partials left after some reaction. A similar description applies for the $[\bar{1}01]$ dislocations observed in the band Ⓑ in Figures 3-5(a), (b) and (c).

Introduction of partial dislocations on both {111} and {001} planes were evidenced in the

semi-in-situ experiments shown in Figure 3-7, whereas <110> perfect dislocations introduced on {001} planes were also confirmed by a CBED method in Figure 3-8. Turning back to the dislocations formed at A in Figures 3-10(a) and (b), production of a $[\bar{1}01]/2$ dislocation on a (010) plane is possible by the dissociation

$$[\bar{2}11]/3 \rightarrow [\bar{1}\bar{2}1]/6 + [\bar{1}01]/2 \quad (5)$$

on a (111) plane. Another $[\bar{1}01]/2$ dislocation may be formed on a (010) plane by the dissociation

$$[\bar{1}12]/3 \rightarrow [121]/6 + [\bar{1}01]/2 \quad (6)$$

on a $(\bar{1}\bar{1}1)$ plane. Thus, a perfect $[\bar{1}01]$ dislocation may be formed as a split configuration on a (010) plane at the intersection such as at A in Figure 3-10(b) and at other similar intersections such as shown by double arrows ① and ② in Figures 3-5(b) and (c).

Upon considering a specific mechanism of the macroscopic yielding, the following characteristic properties must be taken into account: 1) The two <110>/2 partials moved on the different {111} planes might have reacted at a point such as A in Figure 3-10(b). 2) The stress level decreased slowly with a concave down shape at a low temperature but decreased rapidly at a higher temperature to form the concave up shape with discontinuous drop in the v* as shown in Figures 3-2 and 3-9. 3) As confirmed in the semi-in-situ experiments the {001} slip started preferentially at the intersections of {111} planes after motion of the <112>/3 partial dislocations eliminating the {111} faults. 4) The Schmidt factor was largest for the predominant slip of the <110>{001}. In accordance with the above characteristics, a critical process at a low temperature is hypothesized to involve a step to let the two $[\bar{1}01]/2$ partials cross slip on to the (010) plane, resulting in formation of the $[\bar{1}01]$ perfect dislocations according to the possible reactions given by equations (5) and (6). The long range stress required for reactions to occur is estimated to be 600 MPa from the stress level at which the sudden change in v* was noted in Figure 3-9. Such a process will leave either two partials of $[\bar{1}\bar{2}1]/6$ and [121]/6, or their reaction products of [020]/3 or [101]/3 at the intersection. The complex and heavy contrasts remained at the {111} and {001} intersections such as marked by the double arrows ① and ② in Figures 3-5 (b) and (c) may contain these immobile dislocations. The temperature dependent component of the stress in the concave down region in Figure 3-2 may thus be attributed to the thermally activated over coming of the Peierls stress for the cube slips in addition to the long range stress required to cause such a dislocation reaction.

The critical process of the dislocation generation as well as the thermally activated cube slip must be related to various properties such as elastic anisotropy [10], fault energies [6] [25] and the core structures of either <112>/6, <112>/3, <110>/2 and/or <110> dislocations. Further study is needed to pin down the critical process, which explains the magnitude of the v* and the strong tendency of the partial dislocations to lie on the {001} planes as noted by arrows in Figure 3-10 (b). For this purpose more detailed and precise TEM observations such as tried in the other $L1_2$ ordered alloys [46] [16] [47] [48] must be conducted for the dislocations found in the Figures 3-5, 3-7 and 3-10.

3.4.3 *{001} slips at a high temperature*

As it was demonstrated in Figure 3-6, dislocations were introduced randomly without forming a band at 700 K. According to the Burgers vector analyses given in Table 3-III, the major dislocations contributed to the deformation are judged to be the curved ones G lying on the (001) glide planes as observed in Figure 3-6 (b). H and I have the same Burgers vector as G and lie on the (001) planes. They might also have been active with a relatively large Schmidt factor as found in Figure 3-6(e). On the other hand, E and J are identified as pure edge dislocations immobilized by cube locking [46] similar to the Lomer-lock [49] as shown in Table 3-III. Introduction of the immobile dislocations may have contributed to activate other dislocation sources to make the structure homogeneous.

In order to understand the origin of the small v* and generation mechanism of the dislocations G, the area surrounded by a white-broken-line square in Figure 3-6(b) is magnified in Figure 3-11. The <112>/3 partial dislocations are apparently split into smaller Burgers vectors on the (111) planes and some of them have cross slipped on to the (001) planes such as pointed by arrows at P and P' in Figure 3-11. The dislocations P are judged to be $\pm\bar{[}110]/2$ partials with weaker contrast in comparison with P' and G marked by heavy arrows in Figure 3-11 and the visibility is coincident with that of G given in Table 3-III. This observation suggests a possibility that a <110>/2 partial may have cross slipped from {111} plane to a {001} plane, by either one of the dissociation reaction (5) or (6). In the presence of the high density of $D0_{19}$ plates (Figure 3-3), the <110>/2 partials will meet each other to become a <110> glide dislocation on a {001} plane such as pointed at P' in Figure 3-11, possibly assisted by climb.

Another point to be noted is that the glide dislocations on the {001} planes changed the shape from the straight screw type of A and B in Figure 3-5 (Table 3-II) to the curved type of G at 700 K as shown in Figures 3-6 (b) and 3-11 (Table 3-III). This fact implies that the Peierls mechanism such as double kink nucleation for the cube slip may not be the rate controlling process at this high temperature. It is well known that a dislocation tends to align along the Peierls valley at a low temperature [50] when the motion is controlled by the Peierls mechanism.

Then, the responsible mechanism may be assigned as the generation of the <110> glide dislocations, which is presumably governed by atomic diffusion with a small v* (Figure 3-9).

Turning our attention back to the dislocations other than G, various types of the dislocations introduced at 700 K are assumed to be the immobilized reaction products in the sense of glide since Schmid factor is zero as found in Figure 3-6(e) and Table 3-III. Also, the curved dislocations F and those in the circled area in Figure 3-6(a) are found not to lie on unique planes. These observations suggest that they must have been subjected to climb motion. The joggy contrasts of these dislocations apparently differ from the smooth contrasts of the glide dislocations G shown in Figures 3-6 and 3-11. Furthermore, as noted in 3.3 the Burgers vector [010] of the curved dislocations F (Table 3-III) is nearly perpendicular to the curved dislocation line. Therefore, the applied stress may promote the glide on the (001) planes since the Schmidt factor is ~0.5 for the [010](001) as found in Figure 3-6(e). In addition or more predominantly climb motion will take place on the (010) planes. The (010) planes are observed wider in this particular grain because of the sliced angle as mentioned in section 2, the change in the projected shape of the dislocations F can be examined on the long dislocations in Figures 3-6(a) and (c).

Presence of the high density of the immobilized dislocations indicates the easy exhaustion of the glide dislocations induced by atomic diffusion and by the resultant dislocation reaction to decrease the self energy. It follows that fresh glide dislocations such as G must be supplied successively for the deformation to proceed. Once the glide dislocation is introduced presumably by the cross slip coupled with the subsequent climb to become a glide dislocation such as pointed at P' in Figure 3-11, the motion would be spontaneous in the sense of overcoming of the Peierls stress. Therefore, the rate controlling process may be the dislocation generation involving atomic diffusion. For example, the dislocation segment P at the edge character in Figure 3-11 might have climbed locally to meet the partner to become a <110> glide dislocation at P'. Stability of the $D0_{19}$ phase may come into the local climb controlled by the atomic diffusion, thus leading to the drastic decrease in the yield stress (Figure 3-2).

Alternatively, dragging of a pinning point such as noted at the ends of the bowed out dislocations G in Figure 3-11 could be the another possibility controlled by atomic diffusion. The third possibility is that the dislocations F may contribute to the deformation although the generation mechanism of the <100> dislocation is not known from the present observation. Further study is obviously needed to identify the origin of the transition in the rate controlling process upon approaching the $L1_2 \rightarrow D0_{19}$ transformation temperature. Nevertheless, it may be stated that the mechanism of the <110>{001} glide, which is responsible at a low temperature, will be taken over at a higher temperature by a different mechanism involving atomic diffusion, possibly along or in the immediate vicinity of a dislocation.

3.5. Conclusions

By preparing a polycrystalline Fe_3Ge without having the $D0_{19}$ domains, mechanism of {001} slips in the $L1_2$ ordered Fe_3Ge has been studied by means of bulk and thin foil deformation. According to the three-dimensional analyses of the dislocation structure and the Burgers vector determination by visibility tests coupled with an equal thickness contour method and a CBED method, the following conclusions have been drawn for the {001} slips in Fe_3Ge.

1) Before deformation glide dislocations were not readily available for the {001} slips, nor for the {111} slips.
2) Absence of the anomalous temperature dependence was confirmed in the temperature range from 77 K to 900 K with rapid decrease in the yield stress above 600 K.
3) The strain rate sensitivity showed normal temperature dependence at low temperatures but it increased suddenly above 600 K.
4) The {001} glide dislocations were introduced preferentially at the intersections of the two {111} planes and the possible dislocation reactions are suggested on the bases of the bulk and thin foil experiments at 300 K.
5) The glide dislocations were introduced as groups to form slip bands at 300 K whereas various types of dislocations including the <110> glide dislocations were introduced uniformly at 700K involving atomic diffusion possibly in the immediate vicinity of a dislocation.
6) Generation of the <110> glide dislocations is tentatively assumed as a critical process, which involves the cross slip and climb of the <110>/2 partials at 700 K.

References

[1] E. Kato and S. Nunoue, Binary alloy phase diagrams, ASM Handbook **3** 2.195 (Materials Park, Ohio, USA, 1992).

[2] T. Suzuki, Y. Oya and D. M. Wee, Acta Met. **28** 301 (1980).

[3] A. H. W. Ngan, I. P. Jones and R. E. Smallman, Mat. Sci. Eng. **A 153** 387 (1992).

[4] A. H. W. Ngan, I. P. Jones and R. E. Smallman, Phil. Mag. **A 65** 1003 (1992).

[5] A. H. W. Ngan, I. P. Jones and R. E. Smallman, Phil. Mag. **A 66** 55 (1992).

[6] T. J. Balk, M. Kumar and K., J. Hemker, Acta Mater. **49** 1725 (2001).

[7] V. Paider, D. P. Pope and V. Vitek, Acta Metall. **32** 435 (1984).

[8] P. B. Hirsch, Phil. Mag. **A 65** 569 (1992).

[9] M. I. Mills and M. I. Chrzan, Acta Metall. **40**, 3051 (1992).

[10] M. H. Yoo, Scripta Metall. **20** 915 (1986).

[11] M. H. Yoo and C. H. Liu, J. Mater. Res. **3** 845 (1988).

[12] P. Veyssiere, Phil. Mag. **A 50** 189 (1984).

[13] P. H. Thornton, R. V. Davies and T. L. Johnston, Metall. Trans. **1** 207 (1970).

[14] A. E. Staton-Bevan and R. D. Rawlings, phys. stat. sol. (a) **29** 613 (1975).

[15] A. Korner, Phil. Mag. **A 58** 507 (1988).

[16] A. Korner, Phil. Mag. **A 63** 407 (1991).

[17] A. Korner, Phil. Mag. Lett. **72** 21 (1995).

[18] X. Shi, G. Saada and P. Veyssiere, Phil. Mag. A 73 1159 (1996).

[19] K. Jumonji, S. Ueta, A. Miyahara, M. Kato and A. Sato, Phil. Mag. **A73** 345 (1996).

[20] S. Ueta, K. Jumonji, K. Kanazawa, M. Kato and A. Sato, Phil. Mag. **A75** 563 (1997).

[21] T. Murakumo, S. Kumai and A. Sato, Mater. Trans. JIM **41(2)**, 279 (2000).

[22] T. Murakumo, S. Ueta, A. Miyahara, T. Hannuki and A. Sato, Phil. Mag. **A80**, 893 (2000).

[23] B. H. Kear and H. B. F. Wilsdorf, Trans. metall. soc. AIME, **224** 382 (1962).

[24] P. A. Flinn, Trans. metall. soc. AIME **218** 145 (1960).

[25] M. Yamaguchi, V. Vitek and D. P. Pope, Phil. Mag. **A 43** 1027 (1981).

[26] M. Yamaguchi, V. Paidar, D. P. Pope and V. Vitek, Phil. Mag. **A 45** 867 (1982).

[27] V. Paidar, M. Yamaguchi, D. P. Pope and V. Vitek, Phil. Mag. **A 45**, 883 (1982).

[28] G. Tichy, V. Vitek and D. P. Pope, Phil. Mag. **A 53** 467 (1986).

[29] D. M. Wee, O. Noguchi, Y. Oya and T. Suzuki, Trans. JIM **21** 237 (1980).

[30] M. Yamaguchi and Y. Umakoshi, Progress in Materials Science **34** 1 (1990).

[31] Q. Z. Chen, H. W. Ngan and B. J. Duggan, J. Mat Sci. **33** 5405 (1998[a]).

[32] Q. Z. Chen, H. W. Ngan and B. J. Duggan, Intermetallics **6** 105 (1998[b]).

[33] W. G. Johnston and J. J. Gilman, J. Appl. Phys. **30** 129 (1959).

[34] T. Izumi, M. Taniguchi, S. Kumai and A. Sato, Phil. Mag. **84** 3883 (2004).

[35] Y. Ishida, H. Ishida, K. Kohra and H. Ichinose, Phil. Mag. **A 42** 453 (1980).

[36] R., W. Carpenter and J. C. H. Spence, Acta Cryst. **A 38** 55 (1982).

[37] M. Tanaka, J. Electron Microsc. **35** 314 (1986).

[38] E. Orowan, Pro. Phys. Soc. London **52** 8 (1940).

[39] Z., S. Basinski, Phil. Mag. **4** 393 (1959).

[40] G. Schoeck, phys. stat. sol. **8** 499 (1965).

[41] F. R. N. Nabarro, Theory of Crystal Dislocations, Int. Ser. Monographs on Physics, ed. by N. F. Mott, E. C. Bullard and D. H. Wilkinson (Oxford University Press, 1967) p. 704.

[42] T. Mori and M. Kato, Phil. Mag. **A 43** 1315 (1981).

[43] P. B. Hirsch, A. Howie, R. B. Nicholson, D. W. Pashley and M. J. Whelan, Electron Microscopy of Thin Crystals (Butterworth & Co. Ltd., London, 1971) p. 247.

[44] P. Veyssiere and J. Douin, Phil. Mag. **A 51** L1 (1985).

[45] T. Suzuki, M. Ichihara and S. Miura, ISIJ Intern. **29** 1 (1989).

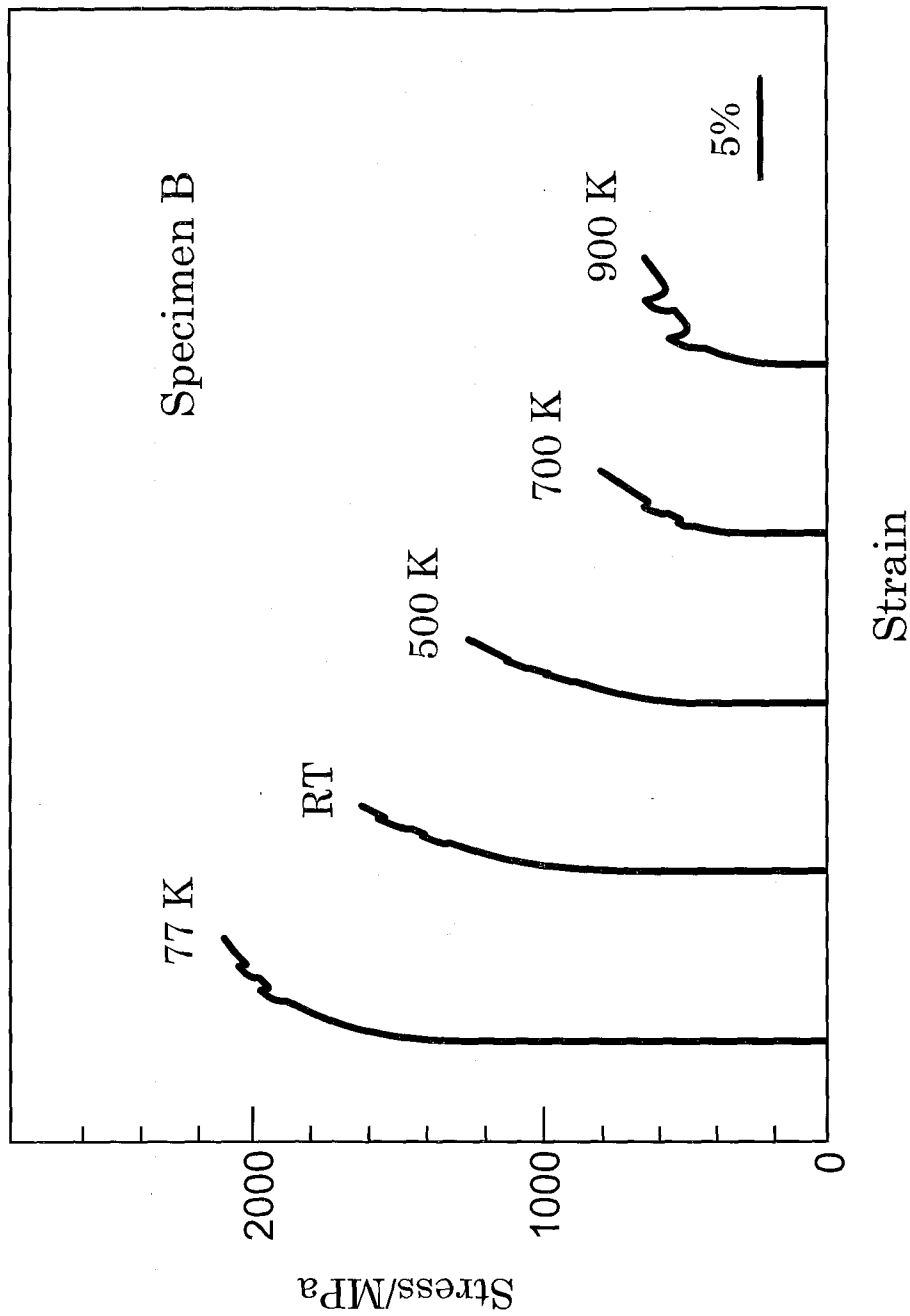
[46] Y. Q. Sun, P. M. Hazzledine, M. A. Crimp and A. Couret, Phil. Mag. **A64** 311 (1991).

[47] Y. Q. Sun and P. M. Hazzledine, in Dislocations in Solid, vol. 10, edited by F. R. N. Nabarro and M. S. Duesbery (Elsevier Science B. V, Amsterdam, Netherlands, 1996).

[48] P. Veyssiere and G. Saada in Dislocations in Solid, vol. 10, edited by F. R. N. Nabarro and M. S. Duesbery (Elsevier Science B. V, Amsterdam, Netherlands, 1996).

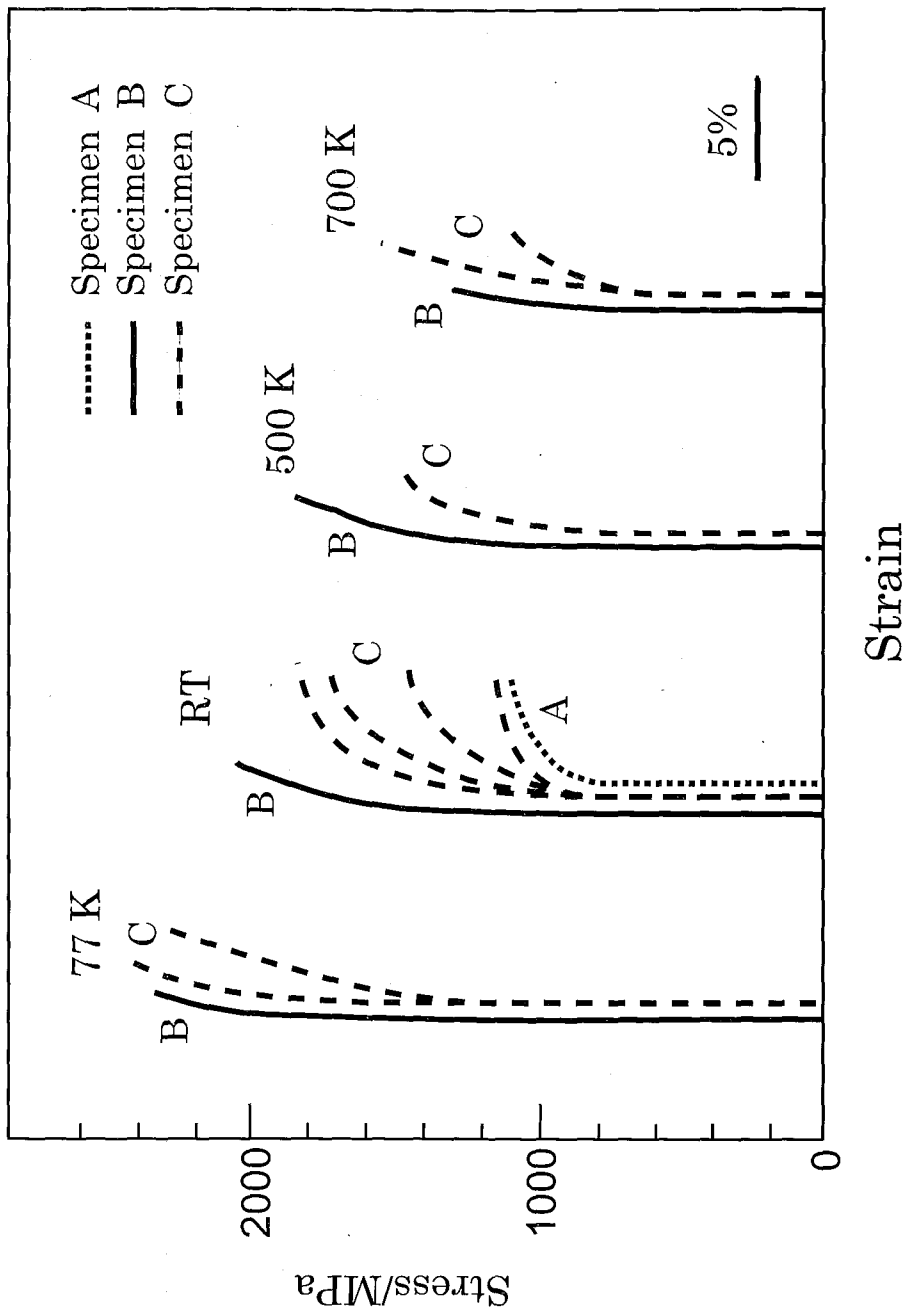
[49] W. M. Lomer, Phil. Mag. **42**, 1327 (1951).

[50] W. A. Spitzig and L. E. Thomas, Phil. Mag., **24** 1041 (1971).



(a)

Figure 3-1
(a) Stress strain curves obtained at various temperatures in bulk tests of the specimens B containing $D0_{19}$ domains. Strain rate sensitivity can be seen on the curves upon change in the strain rate between 1.4×10^{-4} and 1.4×10^{-3} s^{-1}. (b) Stress strain curves compared among the specimens A (rapidly quenched), B (large size) and C (small size).


Specimen A
Specimen B
Specimen C
77 K
RT
500 K
700 K
5%
Stress/MPa
Strain
2000
1000
0

(b)

Figure 3-1

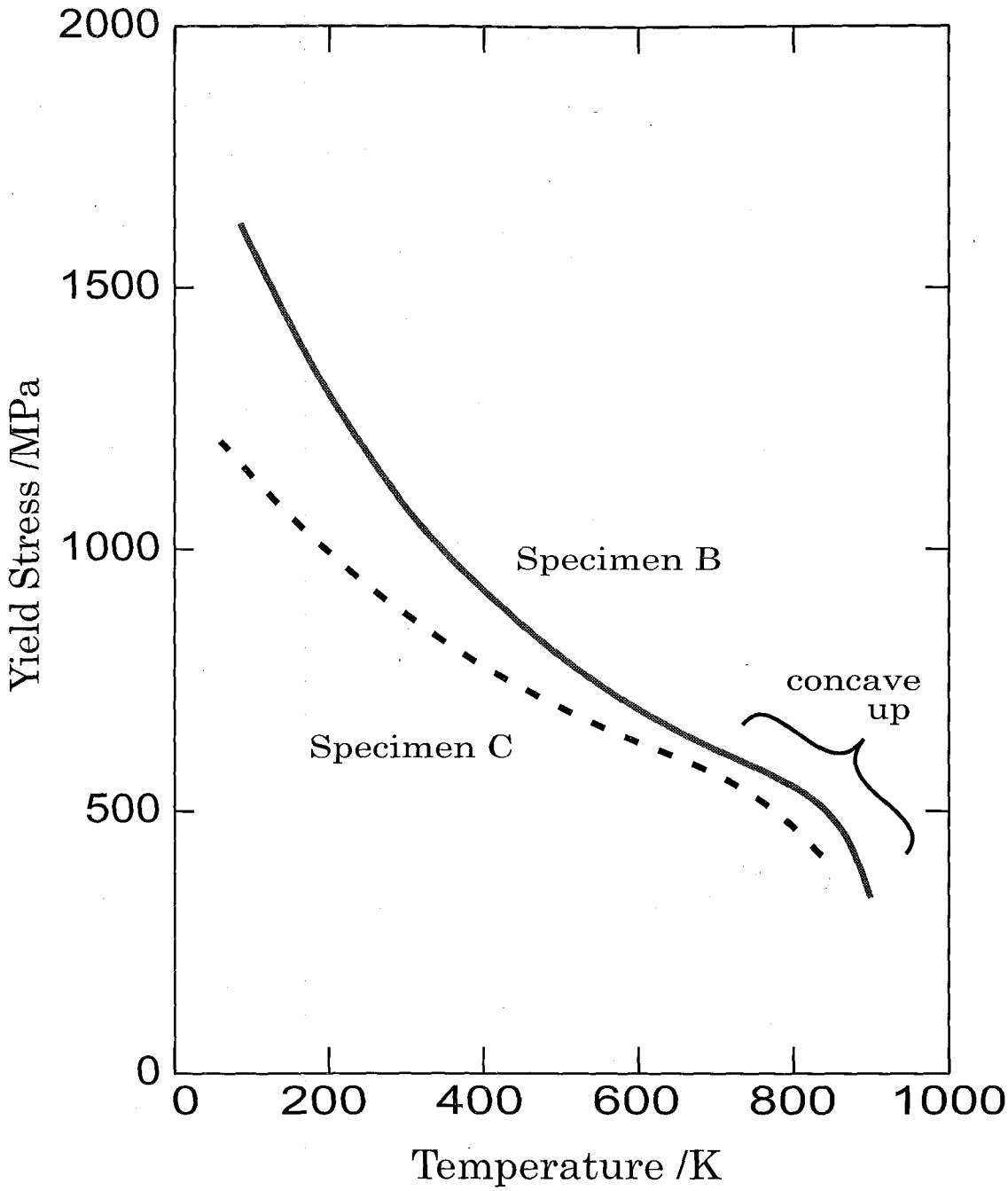
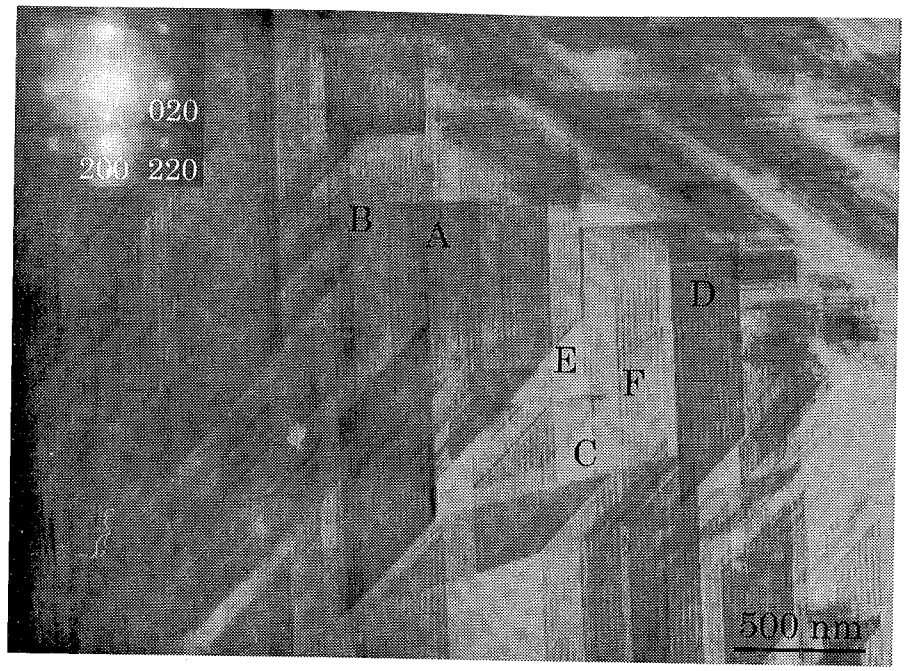
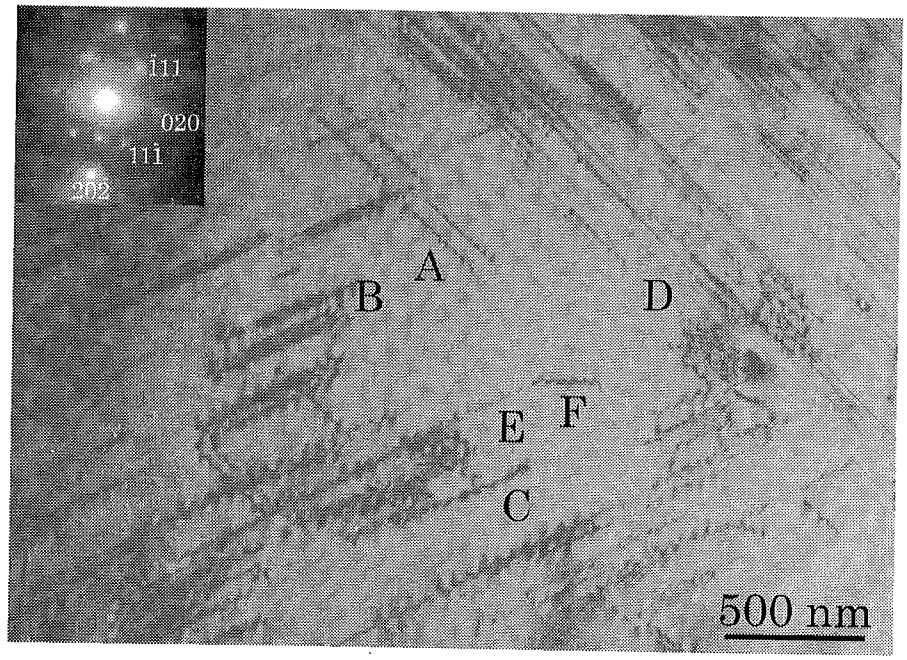


Figure 3-2

Temperature dependence of yield stress defined at 0.2 % offset strain. The solid and broken lines are the results with and without $D0_{19}$ domains.



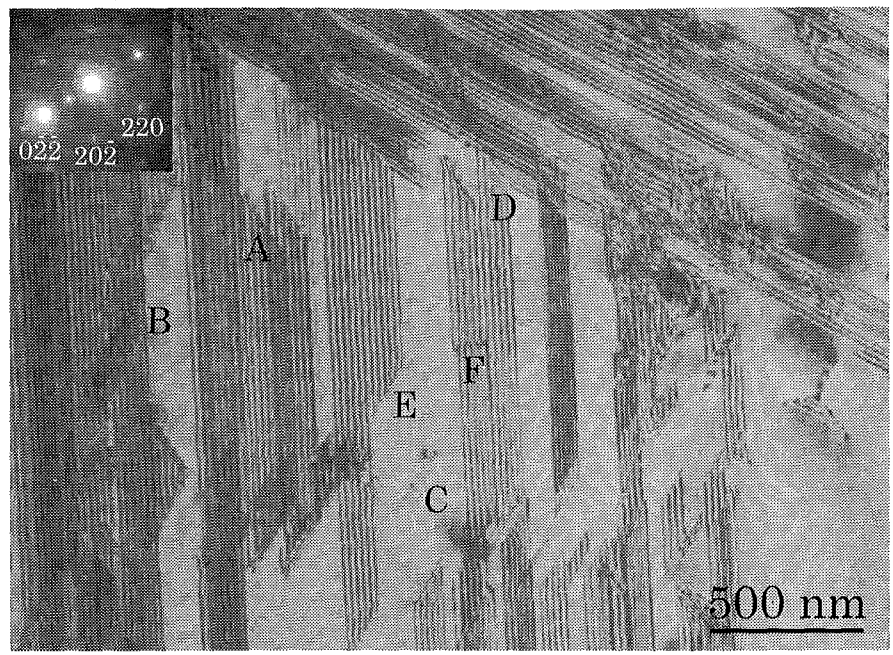
(a)



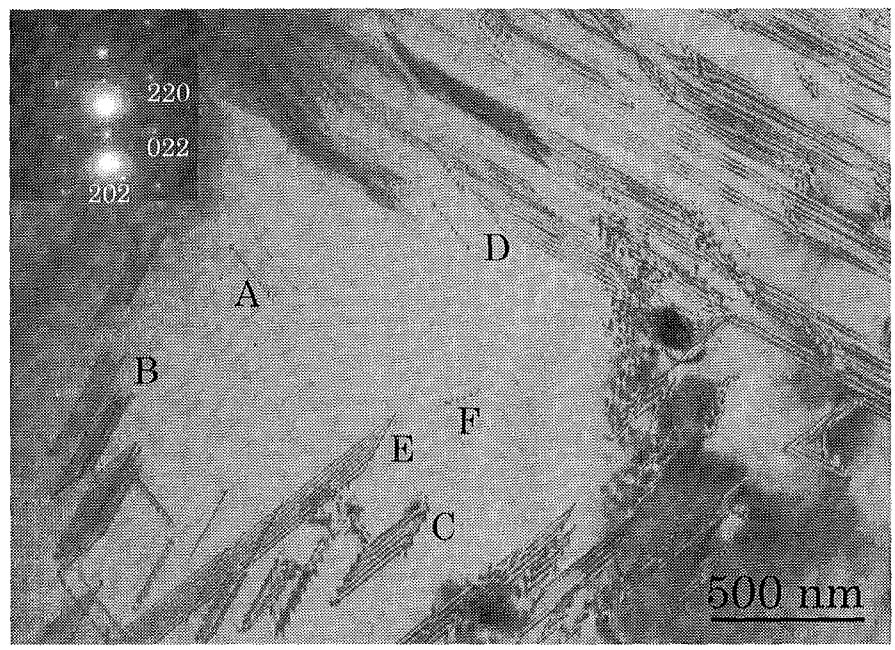
(b)

Figure 3-3

Dislocations and {111} faults observed in the as-annealed specimen A. Beam directions (BD) are (a) [001], (b) [101], and (c) and (d) $[1\bar{1}1]$. **g**=200, $20\bar{2}$, $0\bar{2}\bar{2}$ and $20\bar{2}$ for (a), (b), (c) and (d), respectively. Geometrical information is given by a stereographic projection in (e).

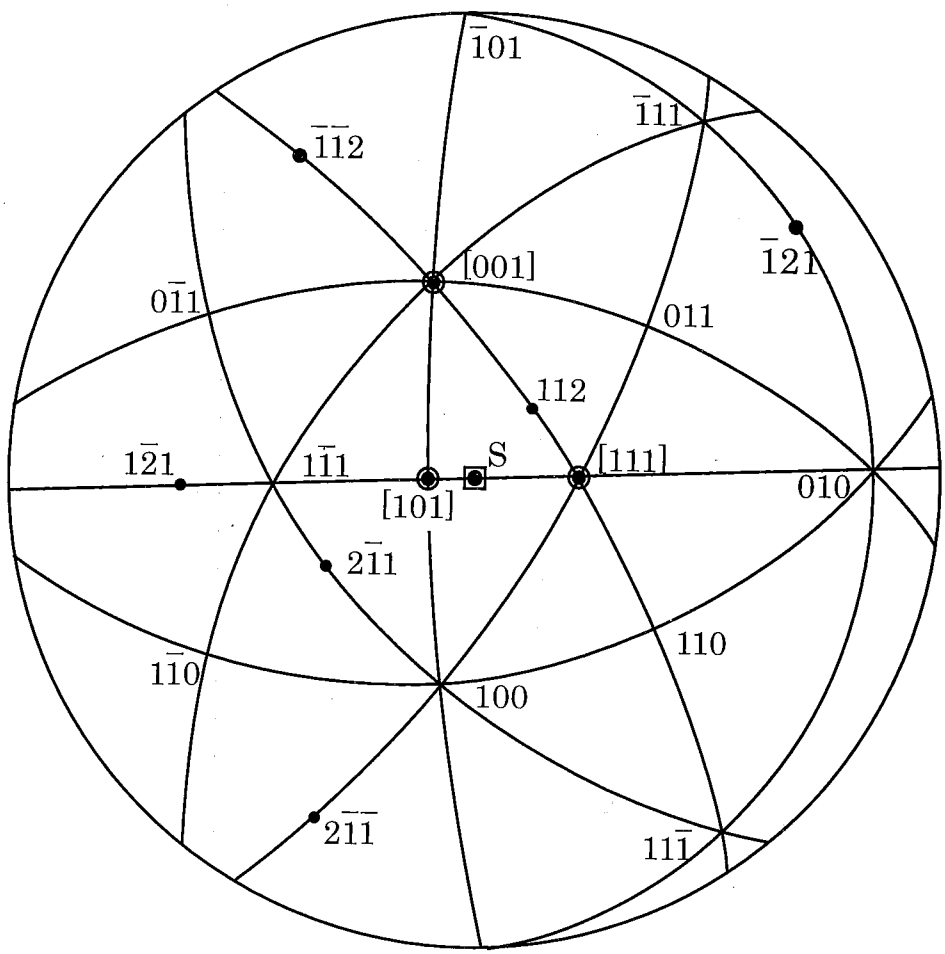


(c)



(d)

Figure 3-3


$\bar{1}01$
$\bar{1}\bar{1}1$
$\bar{1}\bar{1}2$
$\bar{1}21$
[001]
$0\bar{1}1$
011
112
$1\bar{2}1$
$1\bar{1}1$
S
[111]
[101]
010
$2\bar{1}1$
110
$1\bar{1}0$
100
$2\bar{1}\bar{1}$
$11\bar{1}$

(e)

Figure 3-3

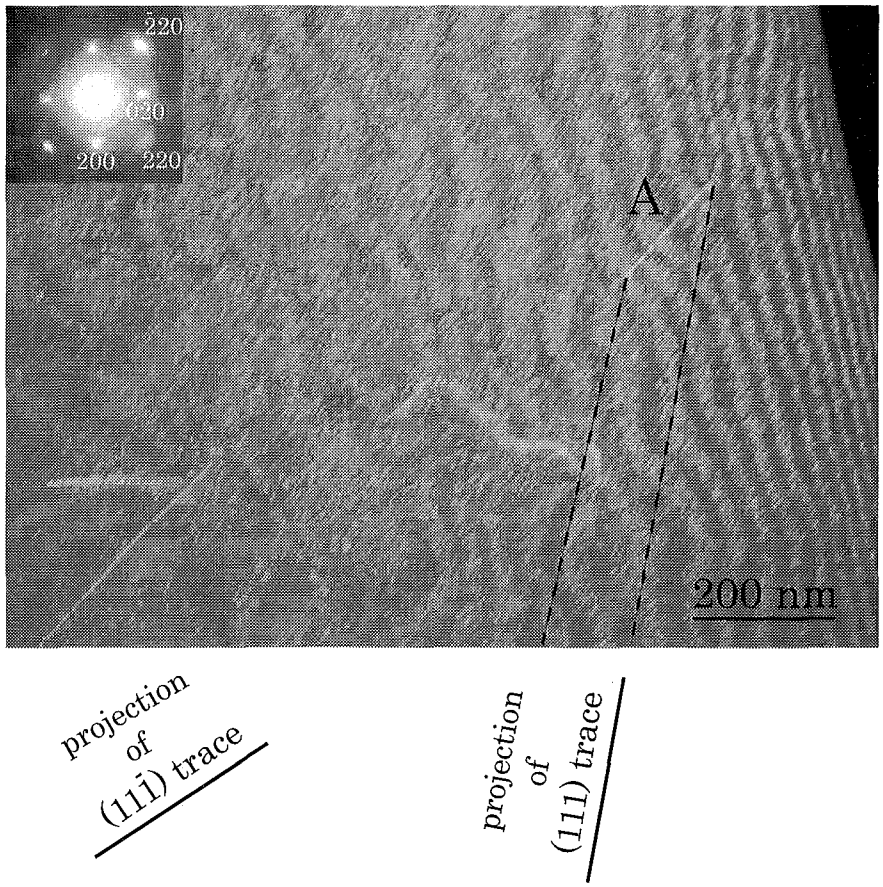
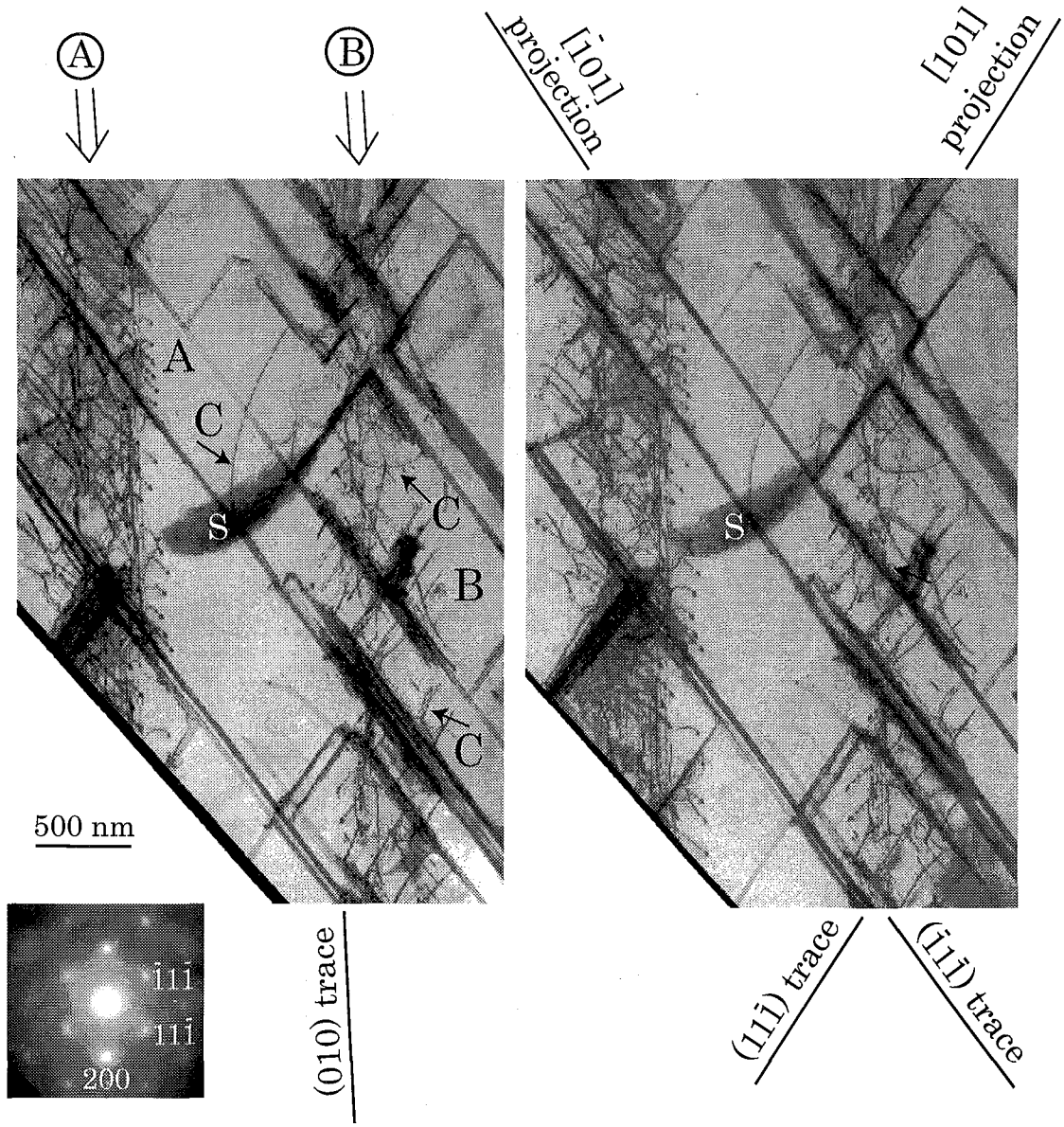


Figure 3-4

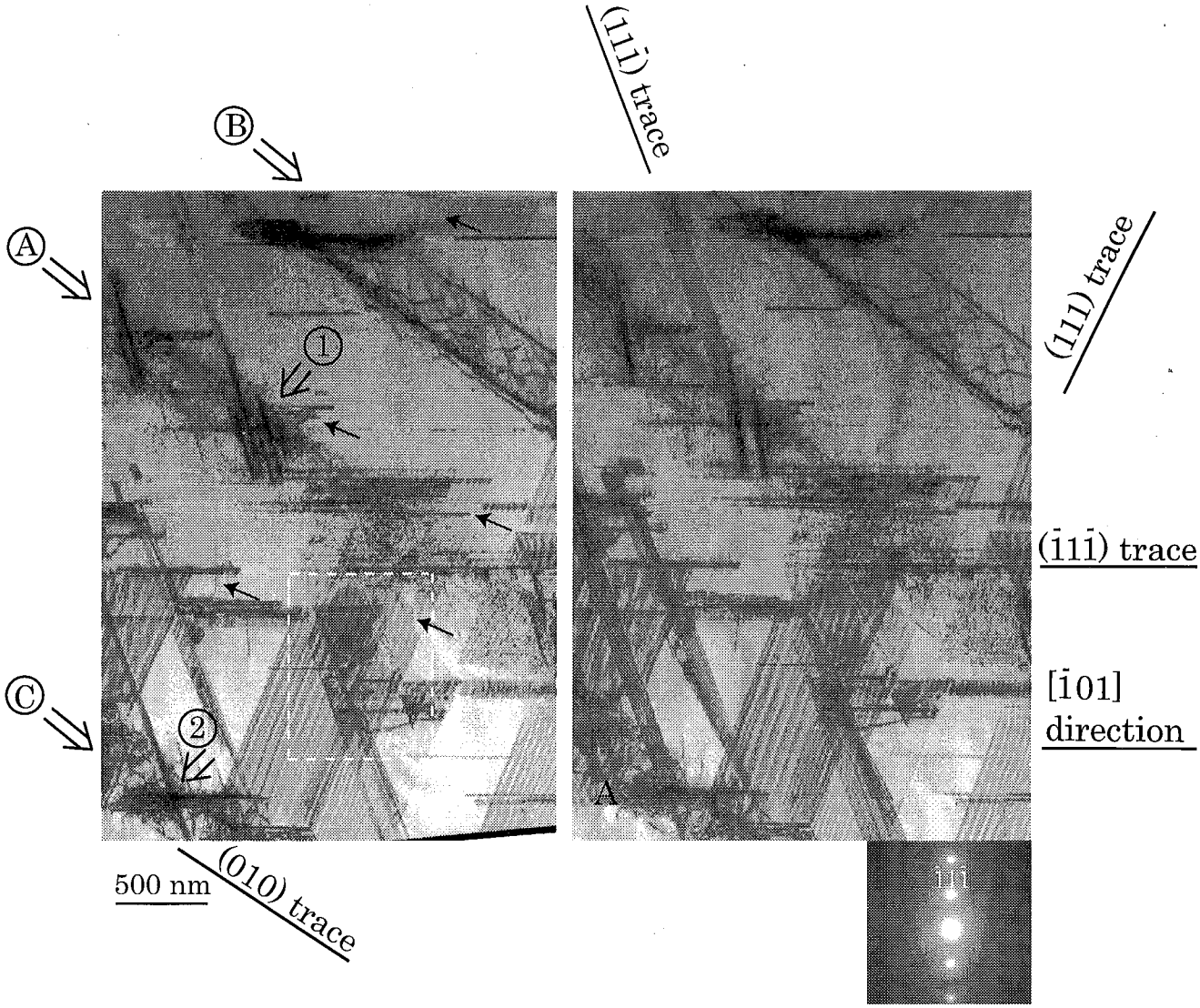
Jumps in thickness fringes induced by a <112>/3 partial dislocation. BD= [001]. **g**= $\bar{2}$20 lying on the shear plane (111) of a partial dislocation with **b**=[2$\bar{1}\bar{1}$]/3. This observation gives the jumps of 2 in accordance with n=**g** · **b**=($\bar{2}$20) o [2$\bar{1}\bar{1}$]/3=-2.



(a)

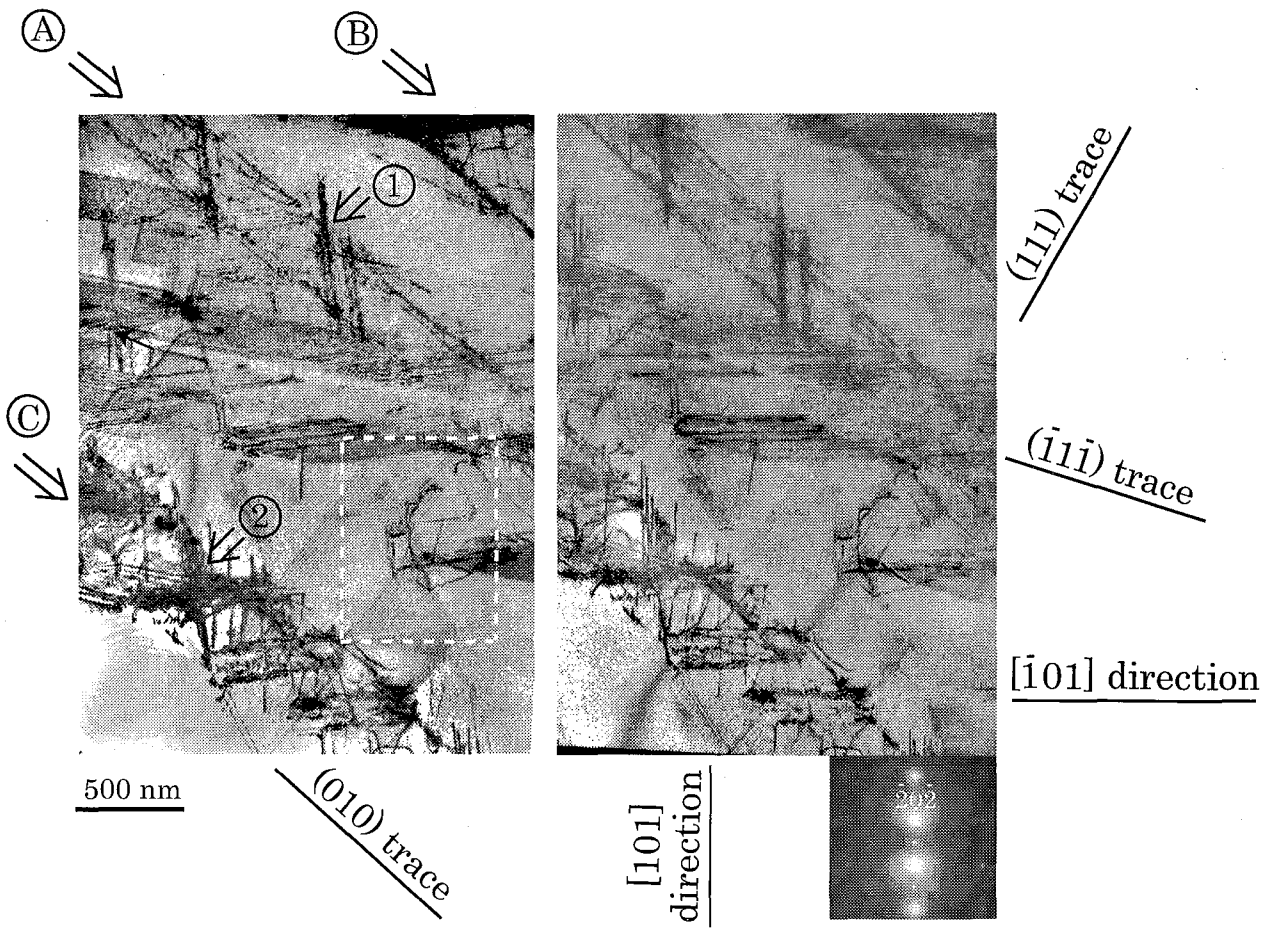
Figure 3-5

Stereo pairs showing dislocation structures in a specimen A deformed at 300 K to 1.4 %. BD= [011], [143] and [010] with **g**=200, $\bar{1}1\bar{1}$ and $\bar{2}0\bar{2}$ for (a), (b) and (c), respectively. Geometrical information is given by a stereographic projection in (d). The surface normal and compression axis are denoted by S(C) in (d).


(11$\bar{1}$) trace
B
A
(111) trace
1
($\bar{1}$11$\bar{1}$) trace
[$\bar{1}$01]
direction
C
2
A
500 nm
(010) trace
111

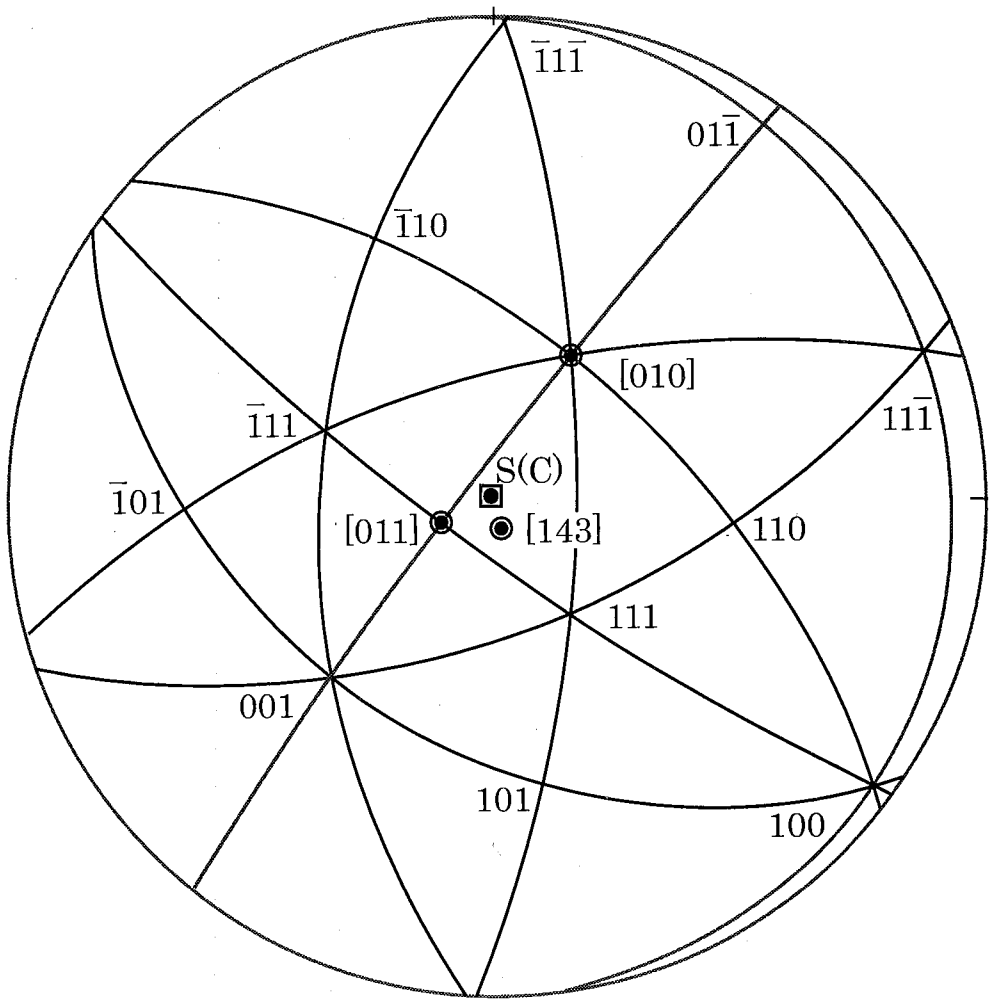
(b)

Figure 3-5


A
B
C
1
2
500 nm
(010) trace
[101] direction
(111) trace
(1̄11̄) trace
[1̄01] direction

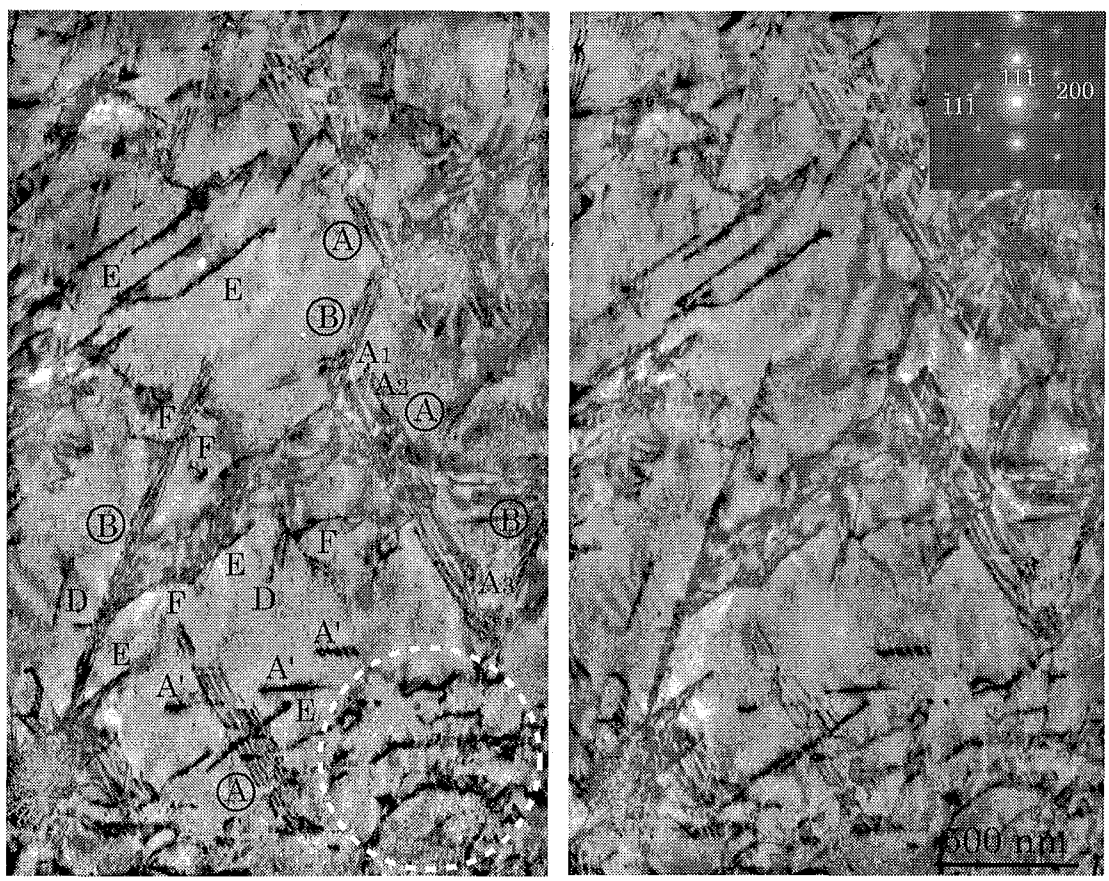
(c)

Figure 3-5


$\bar{1}\bar{1}\bar{1}$
$01\bar{1}$
$\bar{1}10$
[010]
$\bar{1}11$
$11\bar{1}$
S(C)
$\bar{1}01$
[011]
[143]
110
111
001
101
100

(d)

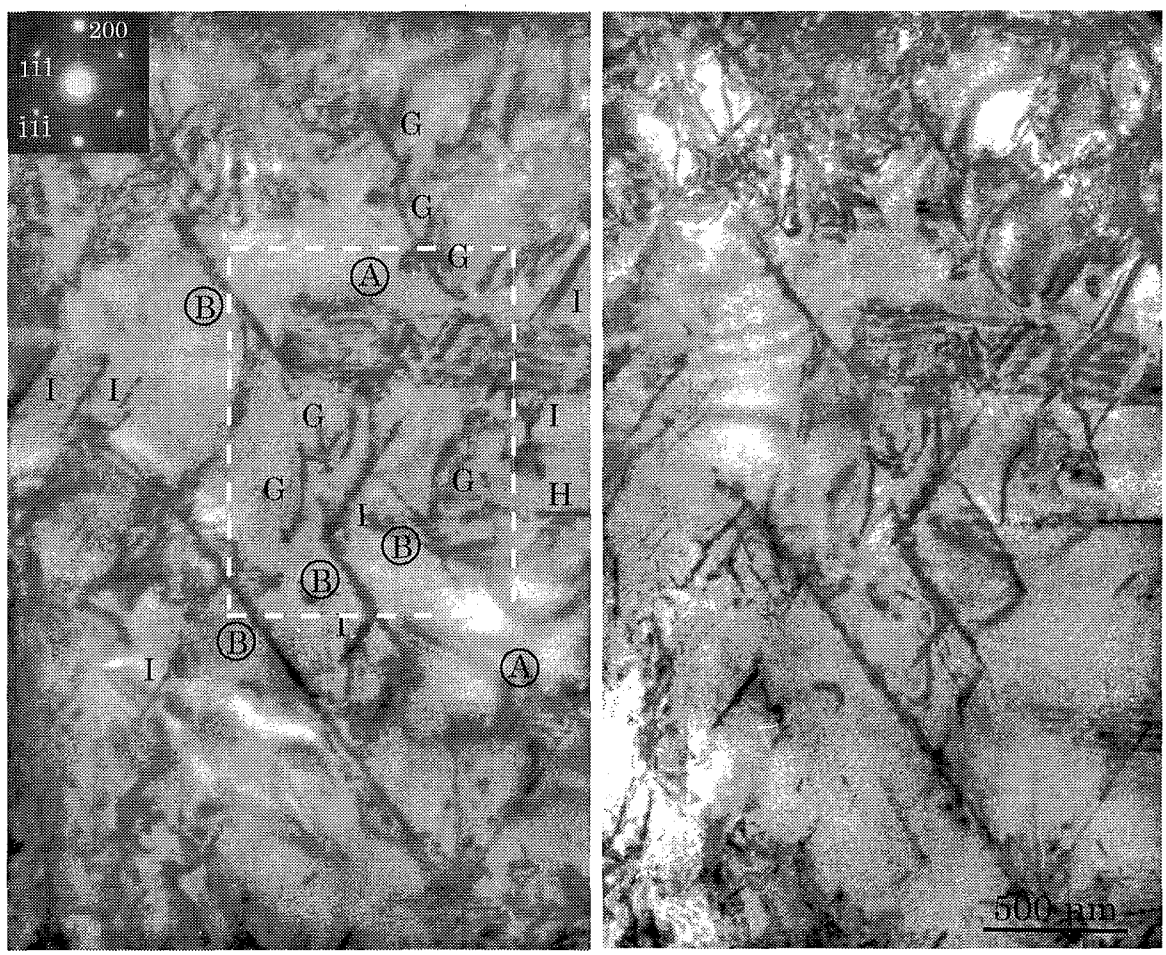
Figure 3-5



(a)

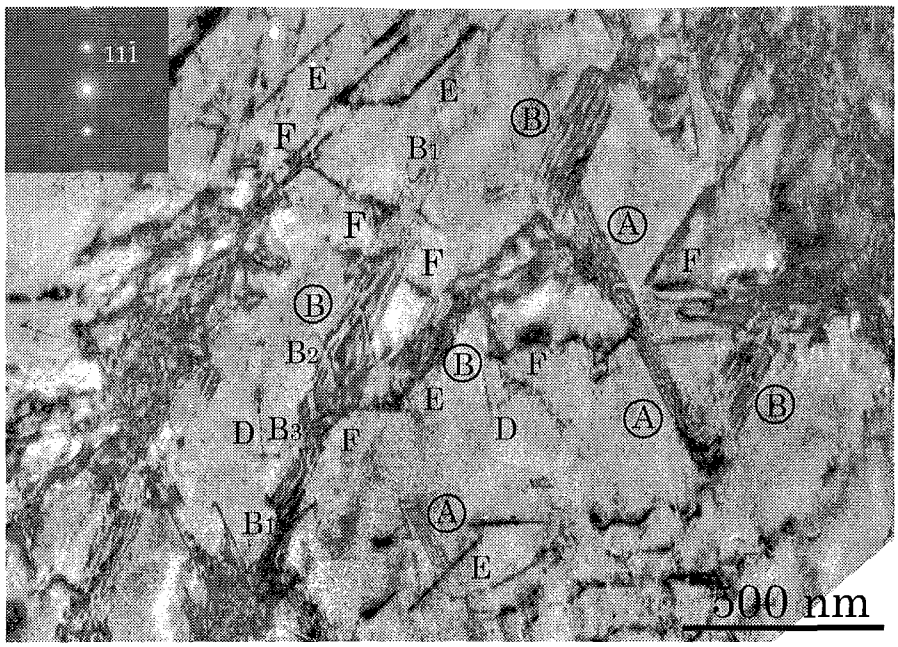
Figure 3-6

Dislocations in a specimen B deformed at 700 K to 2.3 % by compression in bulk. (a) and (b) are stereo pairs: (a) BD=[011] with **g**=11$\bar{1}$. (b) BD= [011] with **g**=200. (c) BD=[$\bar{1}$10] with **g**=11$\bar{1}$ (d) BD=[$\bar{1}$10] with **g**=002. Note that (b) is rotated by 54.7° with respect to (a), (c) and (d) for stereo microscopy and that the BD=[$\bar{1}$10] is tilted by 60° from the BD=[011].

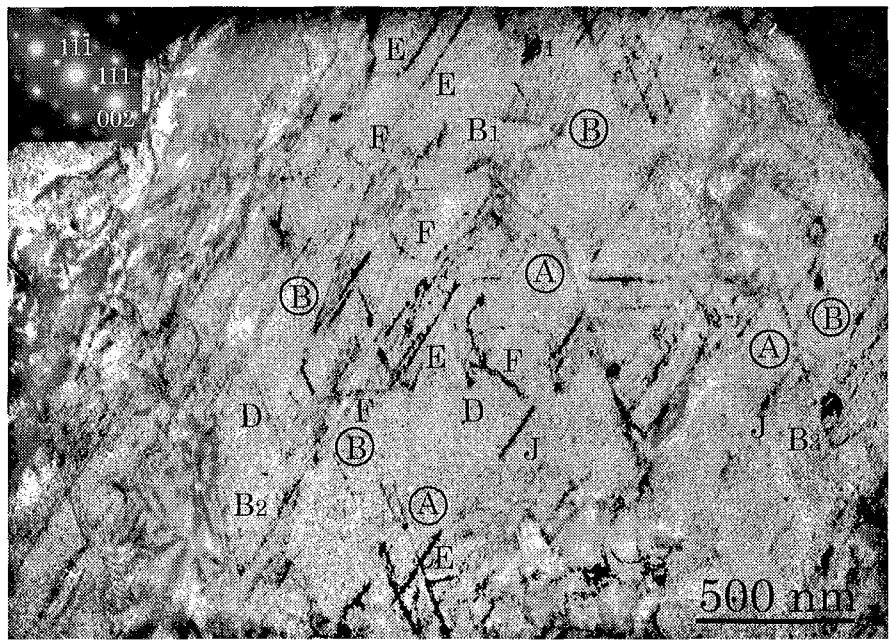


(b)

Figure 3-6

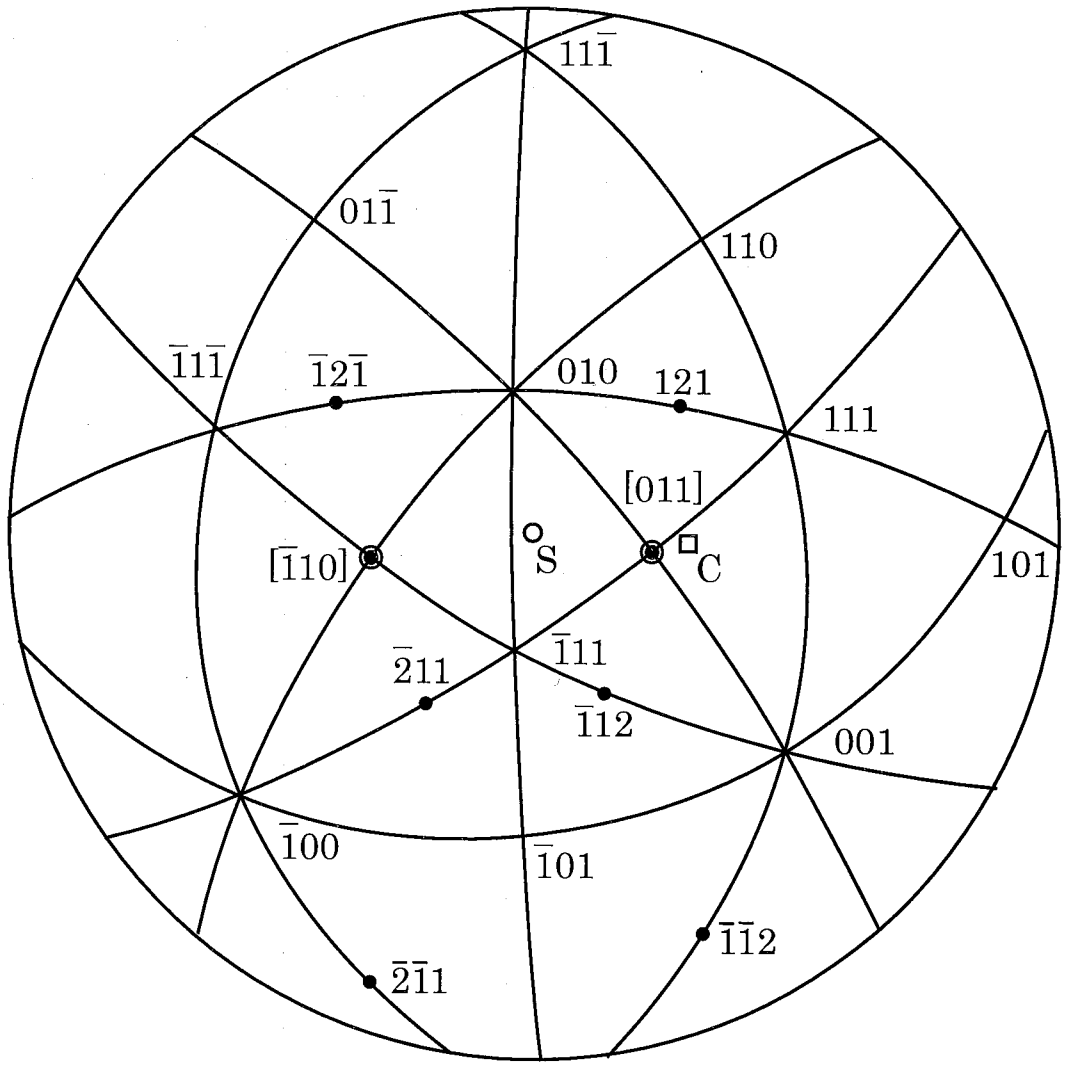

111
E
E
F
B1
B
A
F
F
F
B
B2
B
F
E
D
B3
F
D
A
B
B1
A
E
500 nm

(c)


111
111
002
E
E
F
B1
B
F
A
B
E
F
D
F
D
J
B3
B
B2
A
E
500 nm

(d)

Figure 3-6


$1\bar{1}\bar{1}$
$01\bar{1}$
110
$\bar{1}1\bar{1}$
$\bar{1}2\bar{1}$
010
121
111
[011]
S
C
$[\bar{1}10]$
101
$\bar{2}11$
$\bar{1}11$
$\bar{1}12$
001
$\bar{1}00$
$\bar{1}01$
$\bar{1}\bar{1}2$
$\bar{2}\bar{1}1$

(e)

Figure 3-6



(a)



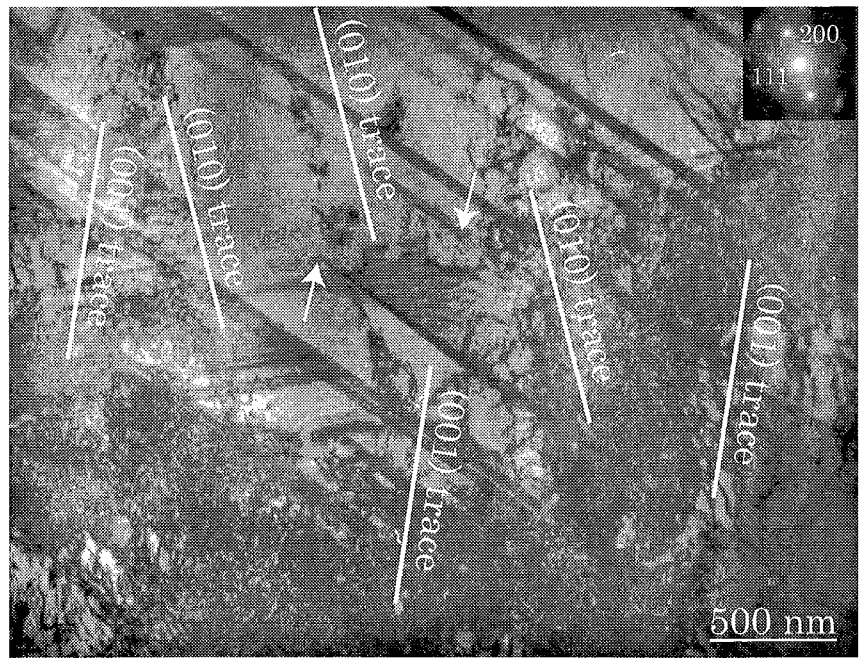
(b)

Figure 3-7

Successive stages of plastic deformation observed in the same area of a specimen A by HVEM at 1000 kV. Observed after loading to 0, 6.0, 8.5 and 10.0 kg for (a), (b), (c) and (d). BD=[0$\bar{1}$1] with the **g**=200 adjusted at a similar value of s for all the photographs.

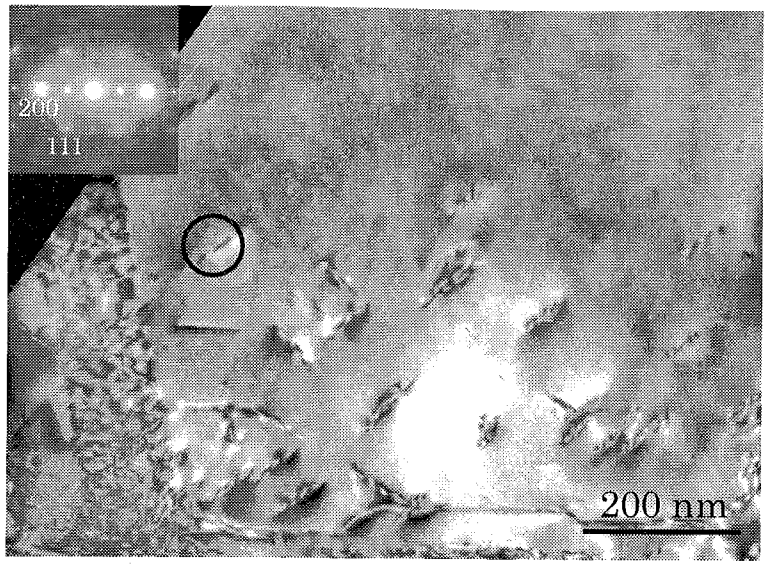

200
111
(001) trace
500 nm

(c)

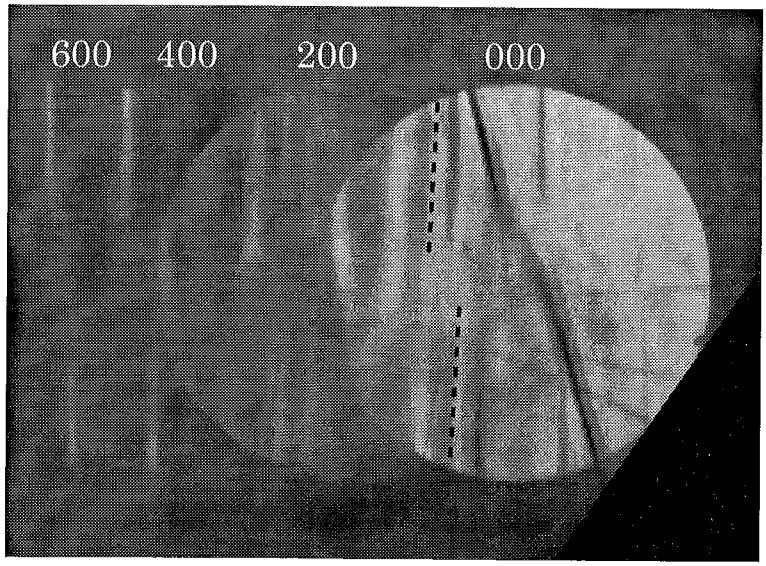

200
111
(010) trace
(010) trace
(010) trace
(010) trace
(001) trace
(001) trace
500 nm

(d)

Figure 3-7



(a)



(b)

Figure 3-8

<101> dislocations examined by a CBED method. (a) Dislocation structure in a specimen A after loading to 10 kg. BD=[0$\bar{1}$1] with **g**=200. (b) Defocused diffraction from the small area marked by a circle in (a). From the jumps on the dark and white lines in the circle, the Burgers vector was determined to be [101] in total but the image of the jump is disturbed by splitting of the [101] into two [101]/2 partials.

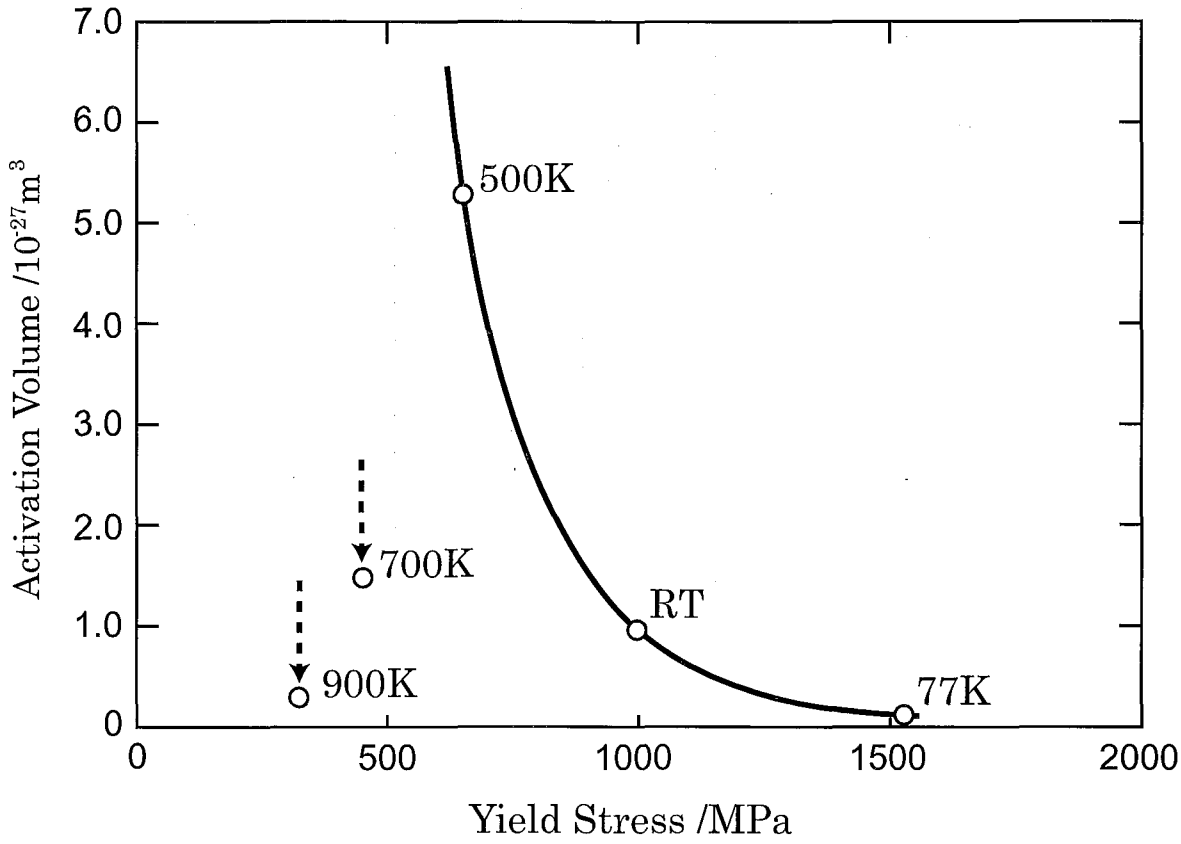
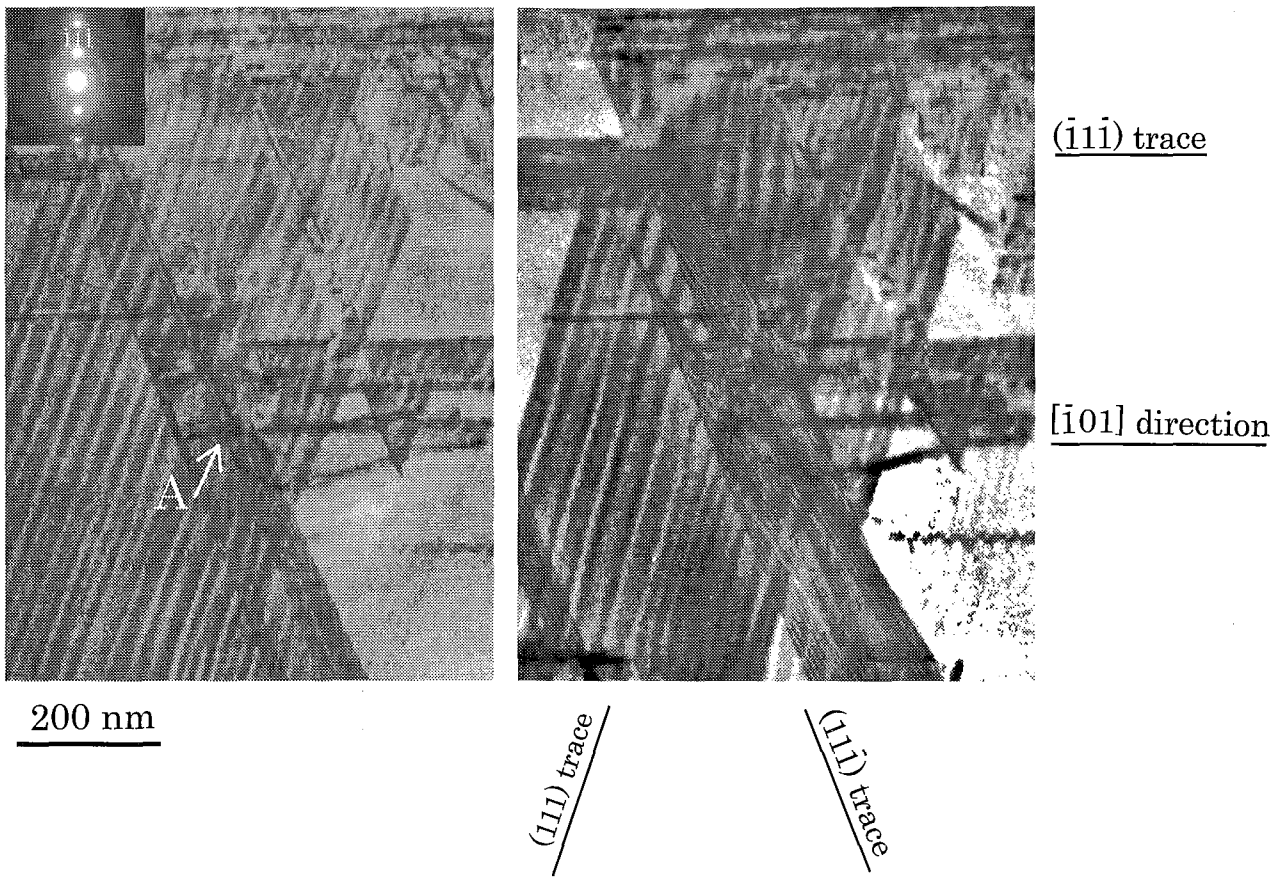


Figure 3-9

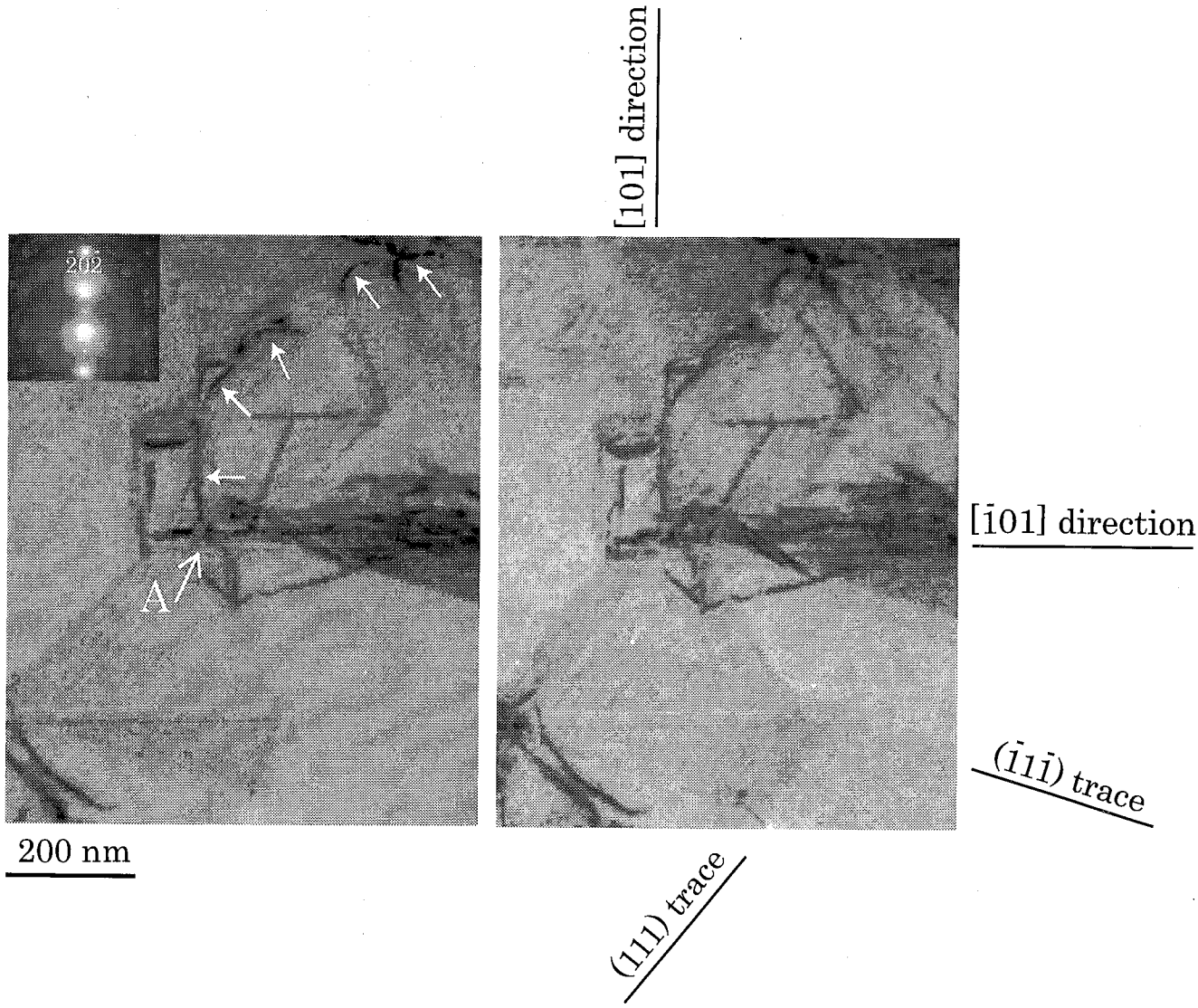
v*-σ plot of a specimen B obtained from Figure 3-1(a). The deformation temperature is denoted at each data point. The sudden decrease in v* below the critical stress of 600 MPa indicates transition in the deformation mechanism at the corresponding temperature.



(a)

Figure 3-10

(a) and (b) are the same area surrounded by a white-broken-line square in Figures 3-5(b) and (c), respectively. (a) BD=[341] with **g**=$\bar{1}1\bar{1}$. (b) BD=[010] with **g**=$\bar{2}0\bar{2}$. The foil specimen is tilted by ~ 45° around the [$\bar{1}$01] from (a) to (b) as found in Figure 3-5(d).


[101] direction
2$\bar{1}$2
A
200 nm
[$\bar{1}$01] direction
($\bar{1}$1$\bar{1}$) trace
(111) trace

(b)

Figure 3-10

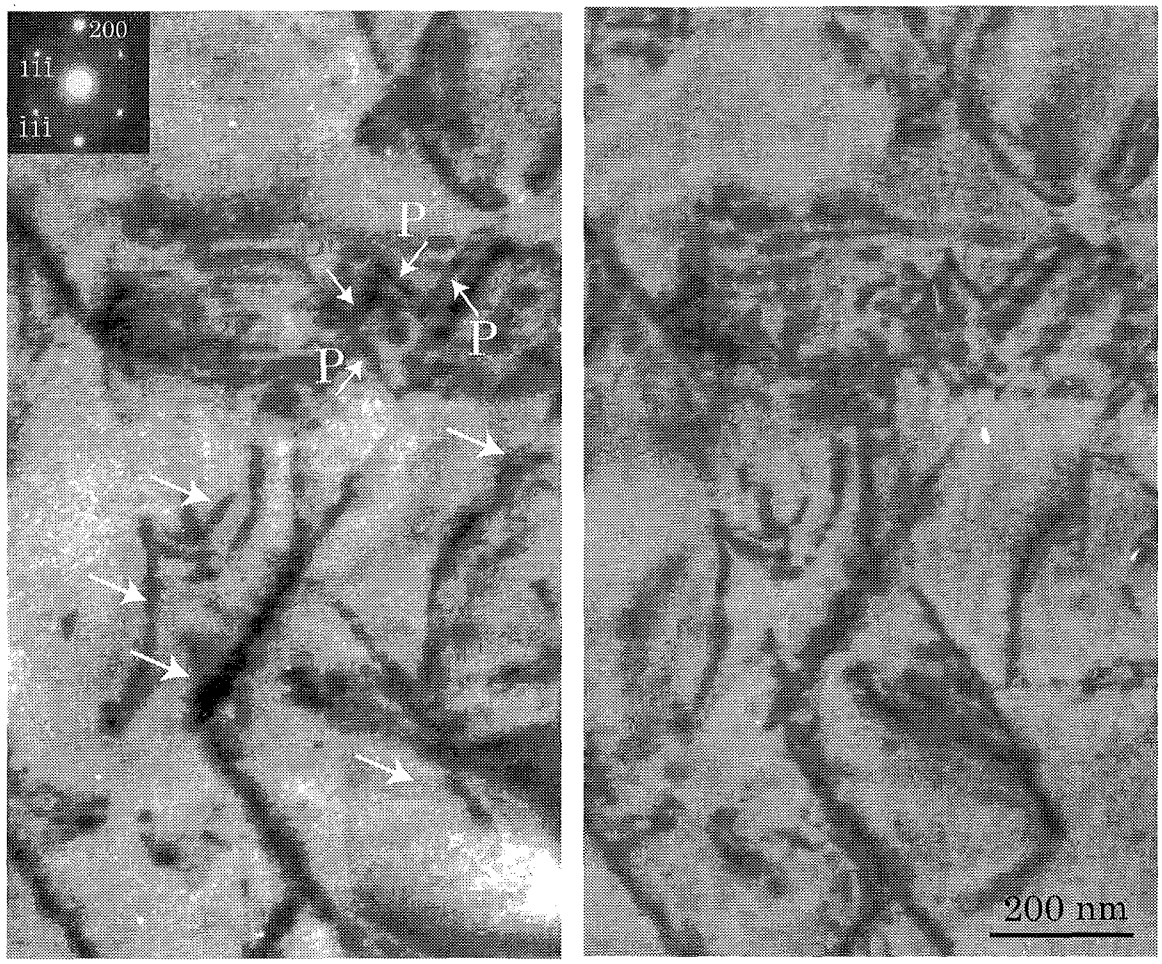


Figure 3-11

Magnified view of the area surrounded by a white-broken-line square in Figure 3-6(b). BD= [011] with **g**=200. Note that dislocations have cross-slipped on to (001) planes at P (with weak contrast) and P' (with strong contrast). The glide dislocations shown by heavy arrows are curved on the (001) planes corresponding to G in Figure 3-6 (b).

Table 3-I

Burgers vectors of the dislocations in the as-annealed specimen A. The alphabet letters correspond to those marked in Figure 3-3. Direction of the dislocation line is indicated below the alphabet. ○, Δ and × indicate visible, weakly visible and invisible cases, respectively. The dislocation images matched with the **g** · **b** values are listed at the bottom line with the types of the dislocations found after the image matching.

g vector /Beam direction /Photos in Figure 4	**g** · **b** value for **b** on a (111) plane						Image intensity					
	$[\bar{1}01]/3$	$[\bar{1}\bar{1}2]/3$	$[0\bar{1}1]/3$	$[1\bar{2}1]/3$	$[1\bar{1}0]/3$	$[2\bar{1}\bar{1}]/3$	A $[0\bar{1}1]$	B $[1\bar{1}0]$	C $[1\bar{1}0]$	D $[0\bar{1}1]$	E $[1\bar{1}0]$	F $[1\bar{2}1]$
(200)/[001]/(a)	-2/3	-2/3	0	2/3	2/3	4/3	○	△	△	×	×	△
$(20\bar{2})/[101]$/(b)	-4/3	-2	-2/3	0	2/3	2	○	○	○	○	○	○
$(022)/[1\bar{1}1]$/(c)	2/3	2/3	0	4/3	2/3	-4/3	○	△	△	×	△	○
$(20\bar{2})/[1\bar{1}1]$/(d)	-4/3	-2	-2/3	0	2/3	2	○	○	○	○	○	○
Image matching	—	B, C	D, E	—	—	A, F	edge	edge	edge	screw	mixed	mixed

Table 3-II

Burgers vectors of the dislocations introduced by deformation at 300 K. The alphabet letters correspond to those marked in Figure 3-5. ○ and × indicate visible and invisible cases. Matching between the **g** · **b** value and the observed intensity is good for all of the dislocations. The directions of the straight dislocations (A, B) and the slip planes of the curved dislocation C are noted by [] and () below the alphabet letters.

g vector /Beam direction	**g** · **b** value for **b** on (010) and (001) planes				Image intensity		
	[110]	[$\bar{1}$10]	[$\bar{1}$01]	[101]	A [$\bar{1}$01]	B [101]	C (010)
(200)/[011]	2	-2	-2	2	○	○	○
($\bar{1}1\bar{1}$)/[143]	0	-2	0	-2	×	○	×
($\bar{2}0\bar{2}$)/[010]	-2	2	0	-4	×	○	×
Image matching	—	—	A, C	B	screw	screw	nearly screw

Table 3-III

Burgers vectors of the dislocations introduced by deformation at 700 K and marked in Figure 3-6. ○, Δ and × indicate visible, weakly visible and invisible cases. Matching between the **g** · **b** value and the observed intensity is good for all of the dislocations. Orientations of the straight dislocations and the planes on which curved dislocations lie are noted by [] and () below the alphabet letters.

g vector / Beam direction	**g** · **b** value for **b** of <110> and <100> types									Image intensity						
	$[01\bar{1}]$	$[\bar{1}10]$	$[\bar{1}01]$	[011]	[101]	[110]	[100]	[010]	[001]	D $[\bar{1}01]$	E [100]	F nearly (010)	G (001)	H [010]	I $[\bar{1}10]$	J [100]
$(11\bar{1})$/ [011]	2	0	-2	0	0	2	1	1	-1	○	○	○	×	×	×	×
(200)/ [011]	0	-2	-2	0	2	2	2	0	0	×	×	×	○	○	○	×
(002)/ $[\bar{1}10]$	-2	0	2	2	2	0	0	0	2	○	○	△	×	×	×	○
Image matching	D, E	G H, I	—	J	—	—	—	F	—	mixed	edge	curved	curved	mixed	screw	edge

Chapter 4

Identification of χ Phase in Fe-Mn-Si Based SMA and the Estimation of Its Strength

4.1. Introduction

In the recent studies, it has been demonstrated that the strength is increased up to ~600 MPa in the yield stress and over 1 GPa in the ultimate strength by introduction of the hardly deformable domains [1] [2]. It means that this particular SMA can be controlled in its strength and ductility by beating and heating treatments. The mechanical property is altered strikingly by introduction of the second phase particles and precipitates [1] [2]. One of the aims focused here is the determination of the crystal structure of the hardly deformable domains by means of micro diffraction method utilized in the earlier studies [3] [4]. Use of the CBED method in microdiffraction analysis gives important information about the three dimensional structure in the reciprocal space (ZOLZ, FOLZ and so on) whereas the usual selected diffraction provides the ZOLZ pattern only.

One of the purposes in this study is to clarify the origin of the change in the mechanical properties by analyzing the unit cell structure of the hardly deformable domains by means of the micro-diffraction method. The microstructures of the SMA containing V and N will be investigated in details on the bases of the stereo microscopy coupled with the 2½D method [5] by using a high voltage electron microscope (HVEM). Particular interest will be put on the grain size refinement, precipitation of the VN and introduction of the non-deformable domains by means of beating and heating treatments.

It is another important aspect of the present study to seek for the ultimate strength of the hardly deformable phase introduced by the beating and heating of the SMA with the size as large as refined grains. Introduction of the hardly deformable secondary phase is known to increase the SME strength remarkably [1] [2]. The rather uniform compression given by the semi-in-situ method described in Chapter 2 is expected to provide quantitative information in the stress level.

4.2. Experimental Procedures

4.2.1. *Specimen preparations*

The base material used in this study is a Fe-Mn-Si-Cr-V-N shape memory alloy (SMA)

supplied by Awaji Sangyo K. K. The composition of the alloy is listed in Table 4-I. The cast alloy was rolled to 6 mm, solution treated at 1423 K for 1 h. and cooled in air. The alloy was cut and mechanically polished into rectangular pieces of 1.0 x (2.1~3.1) x (14~15) mm^3. The further annealing at 1073 K or 1173 K introduced VN precipitates into the alloy and it was important to have C to some extent for the VN to precipitate [6]. High-speed deformation was given by a hammer with the weight of 0.9 kg through a Cu tube, surrounding the specimen so that the SMA was thinned down evenly. The thickness change could be estimated easily from the shape of the SMA visible on the steps formed at Cu surfaces. The strain rate was approximately 2 x 10^3 s^{-1} as estimated from the falling speed of the hammer.

The conditions for the specimen preparation are listed in Table 4-II. Heat treatments of the fresh and deformed specimens were made at 1073 K or 1173 K for 30 min and subsequently cooled in air. The specimens from B to J were treated by annealing, hammering and annealing after hammering as listed in Table 4-II. The specimen I was pre-annealed at 1073 K before the hammering, in order to examine the effects of the coexistence of the VN precipitates and the hardly deformable domains. The approximate grain sizes measured in the deformation bands varied as given in the Table whereas the grains in the non-deformed regions remained locally in the same size as of the non-deformed specimens of A and B.

4.2.2. *TEM observations*

Specimens for transmission electron microscope (TEM) observations were thinned down to 100 μm thick by mechanical polishing, followed by jet polishing at 30 V in a mixture of HClO4 : CH3(CH2)3OCH2CH2OH : CH3OH = 6 : 60 : 34 at 253 K. After stopping the jet polish at the thickness of 10~20 μm, final electro-polishing was made to perforation at the same temperature in the same polishing solution. TEM observations were made by a JEM 2010 and an H-700 at the operating voltage of 160 and 200 kV, and by the H-1250S high voltage electron microscope (HVEM) at the operating voltage of 1000 kV with a double tilt specimen holder.

The crystal structure of the hardly deformable domains introduced by the beating and heating treatments was determined by the method of micro diffraction [3] [4] as described below. The micro diffraction patterns were obtained to contain ZOLZ (zero order Laue zone) and FOLZ (first order Laue zone) by a nearly parallel beam with a small spot size. Information from ZOLZ and FOLZ patterns gives the following crystallographic features: (i) The crystal system can be deduced from the ZOLZ and FOLZ patterns. (ii) The Bravais lattice and the glide planes are revealed from the ZOLZ / FOLZ shift coupled with the differences in the two patterns. (iii) Point group is identified by examining the ZOLZ and FOLZ patterns simultaneously with the knowledge of the intensities. Combination of the itemized

information leads to deduction of the space group or a set of conceivable space groups. It requires the most symmetrical patterns of two or three kinds viewed along different directions. The micro diffraction patterns were taken by a JEM 2010 at 160 kV.

Another TEM imaging technique used here is the 2½D method described by Bell [5]. It utilizes the image shift that occurs in the dark field microscopy upon change in the focus due to the difference in the vectors from the transmitted beam to the diffraction spots. When the two dark field images obtained at two different focusing conditions, over- and under- focus, are observed using a stereo viewer, the objects formed by the different spots will appear at deferent depths because of the relative shift in the image positions. In this way we can find out the local lattice rotation as well as the structural change in a heavily deformed specimen. These observations were made by the H-1250S HVEM.

Some of the TEM specimens were deformed by a simple apparatus designed for pin point compression at the periphery of a hole perforated in the final electro polishing. Figure 2-1 shows a scheme of the compression test. This is called semi-in-situ experiment [7] [8] and used to estimate of the strength of the non-deformable χ phase identified in this study. The specimen loaded to different stress levels was examined repeatedly in the same area under the similar diffraction conditions by the H-1250S HVEM at 1000 kV.

4.3. Experimental Results

4.3.1. *TEM observations*

The microstructures of the deformed and non-deformed specimens were examined by using HVEM. Among the 9 specimens A~J examined in this study, the results of the specimens D (E) and G with the similar microstructures as of the specimens F and H are not shown here to save the space. The specimen J was examined to know the structure at the as-hammered state without annealing.

4.3.1.1. *Non-deformed specimens*

In the specimen A, a very few and small precipitates were already formed in the as-solution treated alloys as shown by arrows in Figure 4-1. The stereographic pair of micrographs in Figure 4-1 also show the ε plates and equivalently stacking faults on {111} planes with Shockley partials attached to them. They are either the stacking faults left after annealing (A) or the ε plates introduced by cooling down to 253 K for electro polishing (B). The two types of the partial dislocations are bowed out towards opposite directions with respect to the fault; the former types of A is to remove the fault and the latter B to form the fault (ε plate), as distinguished by the double arrows A and

B in the figure.

In the specimen B, the heat treatment introduced a large number of well grown precipitates distributed homogeneously in the matrix and heterogeneously on dislocations as shown in Figure 4-2(a). The small precipitates introduced by simple heating have been studied in details and identified as VN compounds to have a NaCl type of the crystal structure satisfying a cube-to-cube orientation relationship with respect to the matrix [6]. It is also found that domains of an intermetallics phase are formed along the grain boundaries as shown by arrows in Figure 4-2(b). This phase was identified to have a much larger unit cell than the γ matrix as analyzed later and is judged to be the hardly deformable entity to increase the strength of the present SMA as discussed later.

4.3.1.2. *Annealed at 1073 K after hammering*

In the specimen C, the annealing at 1073 K after hammering also induced the VN precipitates distributed in the similar manner as in Figure 4-2(a) although not shown here. The important effect of the hammering before the annealing is the introduction of the hardly deformable domains in the refined γ matrix as shown in Figure 4-3. It was found in the specimen F that the hardly deformable domains increased both in number and volume fraction with increase in the amount of deformation. The local structure of the most highly populated region is shown in Figure 4-4. Another typical feature is that the high density of dislocations and the sub grains introduced in γ matrix did not recover by the annealing at 1073 K. The specimen D had the similar structure as the Figures 4-3 and 4-4. These observations can be well correlated with the stress-strain curves of the specimens C, D and F in work of Yamaguchi *et al.* [9]. The increase in the amount of the hardly deformable domains is effective in the strengthening. However, it causes reduction in the ductility.

4.3.1.3. *Annealed at 1173 K after hammering*

In the specimen H, annealed up to 1173 K after hammering, γ matrix was cleaned by annihilation of dislocations as shown in Figure 4-5, indicating that the weakening of the specimen G (the same as H and tensile tested) in the yield stress comes from the structural recovery of the γ matrix, whereas the hardly deformable domains remained the same both in number and volume fraction causing the similar work hardening. The weakening in H also comes from the grain growth as it is well documented in the low magnification micrograph in Figure 4-6 and listed in Table 4-II. Another point to be noted in Figures 4-4 and 4-6 is the tendency of segregation of the hardly deformable domains along the deformation bands traced by dashed lines. The preference in the formation of these domains along the bands is judged to come from the introduction of bcc phase by hammering as shown later.

4.3.1.4. *Annealed at 1073 K before and after hammering*

The specimen I, which explored good SME of nearly 90 % without training, had quite different structure from the specimen C (Figure 4-3) as shown in Figure 4-7 due to the pre-annealing given prior to the hammering. It is typified by introduction of the VN precipitates distributed in finer scale and the thin ε plates in higher density. Instead, the hardly deformable domains are not observed in Figure 4-7. The small spots arrowed just inside the 200 spots of the γ phase in Figure 4-7(b) confirms the VN precipitates satisfy the cube-to-cube orientation relationship [6]. Another important point to be noted is that introduction of the VN precipitates suppresses formation of the hardly deformable domains so that a good ductility could be maintained with reasonable increase in the strength as shown by the curve I [9]. It suggests that the thin ε plates and dislocations introduced by hammering in the presence of fine VN precipitates have contributed to the good deformability and the good SME without training in the specimen I.

4.3.1.5. *As deformed specimen by hammering*

In the as-deformed state by a hammer in the specimen J, the microstructure was composed of heavily deformed γ phase, high density of ε plates and small bcc particles as described below. The γ and ε spots were elongated by heavy deformation. The indices of the γ (fcc), ε (hcp) and α' (bcc) spots are denoted in the diffraction pattern in Figure 4-8. A pair of micrographs shown below the diffraction pattern is a dark field image taken by using a few diffraction spots within the objective aperture marked by double exposure in the diffraction. The bcc images coming from the different spots can be identified on the stereo pair as shown by arrows in the Figure by the 2½D method [5]. As it is observed by a stereo viewer in Figure 4-8, the small images marked by arrows at the intersections of the shear bands are located at the top layer and identified to come from the bcc spot located at right most in the objective aperture. It is therefore hypothesized that the bcc phase introduced by the hammering before annealing acts as the nucleation sites for the hardly deformable domains. As mentioned in 4.3.1.4, comparison of the specimens C and I, however, suggests that introduction of the VN precipitates before the hammering suppresses formation of the hardly deformable domains. It implies that the deformation mode is altered and formation of the bcc phase is suppressed by introduction of the VN precipitates in advance.

4.3.2. *Crystal structure of the hardly deformable domains*

Figures 4-9(a), (b) and (c) show the micro-diffractions obtained from the hardly deformable domains viewed along the three different zone axes <001>, <111> and <110>,

respectively. The space group of the phase was identified following the analysis proposed by Morniroli and Steeds [3] as follows.

Firstly, the highest symmetry observed for this phase is 4mm as shown in the ZOLZ of Figure 4-9(a). This phase also has 6mm as shown in the ZOLZ of Figure 4-9(b). Presence of these two high symmetry axes implies that the crystal corresponds to a cubic system according to the Table 7 in the reference [3]. Secondly, two sets of perpendicular mirrors m1-m2 and m1'-m2' are identified as drawn on the <001> zone axis pattern in Figure 4-9(a). By comparing the ZOLZ and FOLZ patterns and in agreement with Figure 9(d) in the reference [3], the individual partial extinction symbol is judged to be either I-.. or F-.. . Furthermore, the <110> zone axis pattern in Figure 4-9(c) exhibits 2mm symmetries both in the ZOLZ and FOLZ patterns. The ZOLZ / FOLZ shift and the difference in the two patterns by arrows in Figure 4-9(a) lead to the extinction symbol to be I..-, according to Figure 9(d) in the reference [3]. Addition of the two individual partial extinction symbols leads to I--- which is in agreement with the 7 space groups associated with the 5 point groups as given in the Table 3.2 in the reference [10]. Lastly, to make distinction among these seven possible space groups, the point group must be identified. This can be done by observation of the <001> zone axis pattern with the information of the intensities. This <001> zone axis pattern exhibits a 4mm ZOLZ symmetry, whereas the pattern in total has only 2mm symmetry since the mirrors m1'-m2' are not mirrors any more if the intensity of the reflection is taken into account. According to the Table 8 in the reference [9], the point group corresponding to this phase is identified to be $\bar{4}3m$, which is concluded to be of the space group of the present hardly deformable phase. By examining the diffraction patterns, the lattice parameter of the hardly deformable domain is determined to be 0.87 ~ 0.89 nm. The crystal structure of α-Mn has a similar lattice parameter [11] among the well known materials with the $I\bar{4}3m$. This structure is commonly called χ phase in the case of other Fe based compounds [12].

4.3.3. *Semi-in-situ experiments*

In order to estimate the strength of the above mentioned χ phase domains, semi-in-situ compression was conducted for a specimen F by using a hand made apparatus shown in Figure 2-1. A foil specimen prepared from the specimen F was compressed to the higher stress levels step by step and the structural change was observed successively by a HVEM.

A typical example of the semi-in-situ deformation is shown in Figures 4-10(a), (b) and (c). (a) is a bright field image taken after loading to 700 MPa and (b) is the diffraction pattern taken from the circled area in (a). Fine diffraction spots with good symmetry come from the χ phase domain with black contrast noted by the arrow directed up in (a). The domain with bend contours inside the square in (a) is apparently free from dislocations and the diffraction spots

coming from this domain in (b) are sharp and not disturbed in contrast to those coming from the γ matrix. The dark area satisfying the Bragg condition in the matrix in (a) has the strain contrast coming from the overlapped dislocations as usually observed in the heavily deformed crystals. The diffraction spots in (b) coming from the top right in the circled area in (a) are elongated to display the lattice rotation as well as the change in the lattice constants due to the introduction of the high density of dislocations by the sever deformation.

Upon increasing the compressive stress to 1.2 GPa, some of the χ phase domains were found to break as shown in Figure 4-10(c). The actual stress acted on the χ phase domain is, however, suspected to be higher than the stress estimated from the contact area, since a high stress concentration is expected at the χ phase domain practically in direct contact with the hard steel rod (Figure 2-1). This point will be discussed later in more details.

It is also important to note that presence of the hardly deformable χ phase contributes to the recovery strength in the SME through the rapid work hardening. At the same time, evolution of the large pseudo-elasticity for the specimens E, F and G [9] can also be attributed to the presence of the hardly deformable χ phase domains. Concurrently, the VN precipitates play an important roll in increasing the homogeneously distributed Shockley partials when hammered and heated after introduction of the precipitates. Then, the proper combination of the VN precipitates and the χ phase domains is expected to give a good SME at a high stress level with good ductility.

4.4. Discussion

4.4.1. *On the formation mechanism of the χ phase domains*

The χ phase has a structure of α-Mn type that appears in pure Mn below 1000 K when Mn concentration exceeds 50 wt. % in Fe-Mn binary alloy [13]. In a nonequilibrium phase diagram shown by Sumiyama *et al.* [14], α-Mn structure exists in $Mn_{1-y} - Fe_y$ binary alloys for $y \leq 0.8$ by vapor quenching. Schüle and Lang [15] found that α-Mn phase forms in a Fe-rich region of a Fe-Mn-Cr alloy in equilibrium diagram. Formation of the α-Mn type phase in the present Fe-Mn-Si-Cr-V-N SMA is in good accordance with the earlier studies mentioned above.

As shown in Table 4-III, the α-Mn type of χ phase domains were not observed in the as-solution treated state, but they were found occasionally at grain boundaries after annealing at 1073 K and more commonly in the matrix by annealing after hammering, especially at intersections of the shear bands. Formation of the small bcc particles by hammering was identified by the 2½D method [5] in Figure 4-8. Introduction of the small bcc phase by heavy cold rolling has also been discussed in details by Inamura *et al.* [16]. Formation of the small bcc particles may commonly be attributed to the atomic motion involved in the stress induced

martensitic transformation from fcc to bcc [17]. The situation by hammering is thus well linked to the formation of the χ phase domains as groups presumably from the small bcc particles at the intersections of shear bands (Figure 4-6). It is then hypothesized that the α-Mn type of the $I\bar{4}3m$ domains nucleated preferentially along the shear bands have grown into the observed size with expense of the elastic energy induced by the hammering. It is also found in Figure 4-7 that formation of the χ phase domains is suppressed in the specimen I pre-annealed for introduction of the VN precipitates prior to the hammering, increasing the ductility [9]. The over all results suggest the importance of the combination of the beating and heating treatments in optimizing the SME strength with reasonable ductility or in producing a high dumping alloy by motion of Shockley partials.

4.4.2. *Stress concentration at the χ phase domain*

As mentioned in 3.3.3, the stress acting on the χ phase domain must be higher at the contact with the compression rod in absence of the plasticity of the domain at a high stress level due to the weaker γ phase matrix surrounding it. The materials placed under the high stress are the hard steel rod, the hard steel platform, Al foils and the γ phase matrix besides the χ phase domain in the present set up shown in Figure 2-1. Since the weaker materials compressed over the ultimate strength will be squeezed out away from the χ phase domain, it is easily imagined that the applied force will be supported more strongly at the non-deformable χ phase domain. In the following discussion, the χ phase domain is assumed flat and circular with the same thickness as the surrounding γ phase matrix. Since the χ phase domain tended to remain thicker than the γ matrix due to the slower polishing rate, the flat assumption adopted below will provide a lower limit of the stress concentration.

The geometrical situation at a high stress level is depicted schematically in Figure 4-11 with recognition of the yield strength and the work hardening of the constituent materials. The compression rod and the platform made of a hard steel are known to have the yield stress exceeding 3 GPa, whereas the yield strength is substantially lower for the γ matrix and the Al foils. The large force applied by the rod was found to squeeze the Al foils (Figure 2-1) out towards the periphery of a hole locally in the TEM specimen. Therefore, the Al foils are not drawn in Figure 4-11. Although the stress is not uniform over the flat χ phase domain and will reach infinite value at a sharp corner in absence the surrounding material [18], the stress concentration at the edge portion of the hardly deformable χ phase domain will be released locally by plastic deformation of the γ matrix and the hard steel rod. In reality, the stress concentration at the edges may be smaller since the corner is rounded by the slower electro polishing rate at the χ phase. Accordingly, the compression rod and the platform made of a hard steel are hypothesized not to exceed the yield strength upon drawing Figure4-11. Since

the γ matrix deforms heavily at this stress level, the stress concentration at the χ phase will determined by the work hardening of the surrounding γ phase matrix, which suppresses the elastic distortion of the hard steel rod and the platform.

The quantitative description of the stress concentration requires the knowledge of the yielding and flow of the hard steel used in the present study and the stress strain behavior of the γ matrix. According to the macroscopic stress strain curve of the as-annealed specimen A [9], the specimen thickness at sufficiently far from the χ phase domain may be estimated by extrapolation of the work hardening curve to the stress level estimated from the dimple mark under the compression rod. By assuming the stress strain curve to take a parabolic form [19], the thickness d can be estimated from

$$\sigma = \sigma_0 + \alpha\sqrt{\varepsilon} \tag{3}$$

and

$$d = d_0/(1+\varepsilon). \tag{4}$$

The values of σ_0 = 250 MPa and α=1340 MPa were found for the specimen A in the report of Yamaguchi *et al.*[9], according to the Eq. (3). Then, one obtains $\varepsilon \cong 0.5$ corresponding to the applied stress of 1.2 GPa and hence $d/d_0 \cong 2/3$ from Eq. (4). The schematic drawing of Figure 4-11 is given on this base. Apart from the precise arguments, a crude value of the stress concentration may be given by S/s where s is the area of the direct contact with the χ phase domain. Here, the area S, where the plastic deformation was protected by the non-deformable χ phase domain can be found, for example, by tracing change in the distorted diffraction spots from the deformed γ phase matrix such as shown in Figure 4-10(b) around the χ phase domain. This information was taken into account in the drawing of Figure 4-11. Since the aerial ratio is proportional to the square of the radius, a typical value of S/s was found to be ~4. From the above consideration and the fact that the χ phase did not deform at 700 MPa but fractured at 1.2 GPa as shown in Figure 4-10, the strength of the χ phase domain was estimated to be in the range of 3~5 GPa. The actual strength could be higher than the above estimation since the χ phase domain remained thicker than the γ phase matrix after electro polishing. Introduction of such a strong domain increases the strength by work hardening and the strengthening effect would be more pronounced with better ductility, provided that the χ phase domains are distributed more uniformly. This problem is left for future study.

4.5. Conclusions

1) By analyzing the ZOLZ and FOLZ micro diffraction patterns, the hardly deformable phase is identified to have a bcc based unit cell of $I\bar{4}3m$, called χ phase of the α-Mn type.

2) Introduction of the χ phase domains, which are considered to determine the strength and ductility of the present SMA, is shown to be controlled by the small bcc embryos induced at the intersections of the shear bands.

3) Strength of the χ phase domain was estimated to be in the range of 3~5 GPa from the semi-in-situ deformation of a thin foil specimen.

4) Introduction of the precipitates into the Fe-Mn-Si based SMA is found to decrease the χ phase domains to improve the ductility by proper combination of the high speed deformation and the heat treatment.

References

[1] Y. Yamaguchi, BE Thesis, Tokyo Institute of Technology (2003).

[2] A. Sato, H. Oonishi, Y. Yamaguchi, S. Kumai, T. Maruyama, and H. Kubo, The Mike Meshii Symposium on Electron Microscopy: Its Role in Materials Research, TMS Annual Meeting, (2003) p.183.

[3] J. P. Morniroli, and J. W. Steeds, Ultramicroscopy **45** 219 (1992).

[4] A. Redjaïmia and J. P. Morniroli, Ultramicroscopy **53** 305 (1994).

[5] W. L. Bell, J. Appl. Phys. **47** 1676 (1976).

[6] S. Farjami, K. Hiraga and H. Kubo, Mat. Trans. **45** 930 (2004).

[7] S. Miyazaki, A. Kawachi, S. Kumai and A. Sato, Mat. Sci. Eng. **A 400-401** 294 (2005).

[8] M. Taniguchi, K. Morizumi, S. Miyazaki, S. Kumai and A. Sato, Phil. Mag. in press (2005).

[9] Y. Yamaguchi, S. Miyazaki, S. Kumai and A. Sato, Phil. Mag. submitted for publication.

[10] T. Hahn, International Tables for Crystallography vol. A Fourth Edition, The International Union of Crystallography 47 (1995).

[11] C. P. Gazzara, R. M. Middleton, R. J. Weiss and E. O. Hall, Pearson's Handbook of Crystallographic Data for Intermetallics Phases vol.3, American Society for Metals 2710 (1967).

[12] J. S. Kasper, Acta Met. **2** 456 (1954).

[13] H. Okamoto, Alloy phase diagrams ASM Handbook Vol. 3 2.197 (1992).

[14] K. Sumiyama, N. Ohshima and Y. Nakamura, Phys stat. sol. (a) **98** 229 (1986).

[15] W. Schüle and E. Lang, Effects of Radiation on Materials: 15th International Symposium, (ASTM STP 1125) p. 945.

[16] T. Inamura, K. Takashima and Y. Higo, Philosophical Magazine **83** 935 (2003).

[17] A. J. Bogers and W. G. Burgers, Acta Met. **12** 255 (1964).

[18] S. Timoshenko and J. N. Goodier, Theory of Elasticity (MacGraw-Hill Book Company, 1951) p. 96.

[19] G. I. Taylor, The mechanism of plastic deformation of crystals, Proc. Roy. Soc. A **145** 362 (1934).

Table 4-I
Chemical composition of the alloy used in this study.

	C	Si	Mn	P	S	Cr	V	O	N	Fe
wt%	0.03	5.90	27.85	<0.003	0.009	4.88	0.490	0.0022	0.0350	Bal.

Table 4-II
Conditions for specimen preparation and the approximate grain size

Specimens	Pre-annealed at [K]	Hammered by [%]	Annealed at [K]	Grain size μ m
A	——	——	——	100
B	——	——	1073	100
C	——	6.5	1073	15
D	——	27	1073	5
E	——	30	1073	5
F	——	43	1073	5
G	——	39	1173	10
H	——	48	1173	10
I	1073	6.7	1073	15
J	——	27	——	——

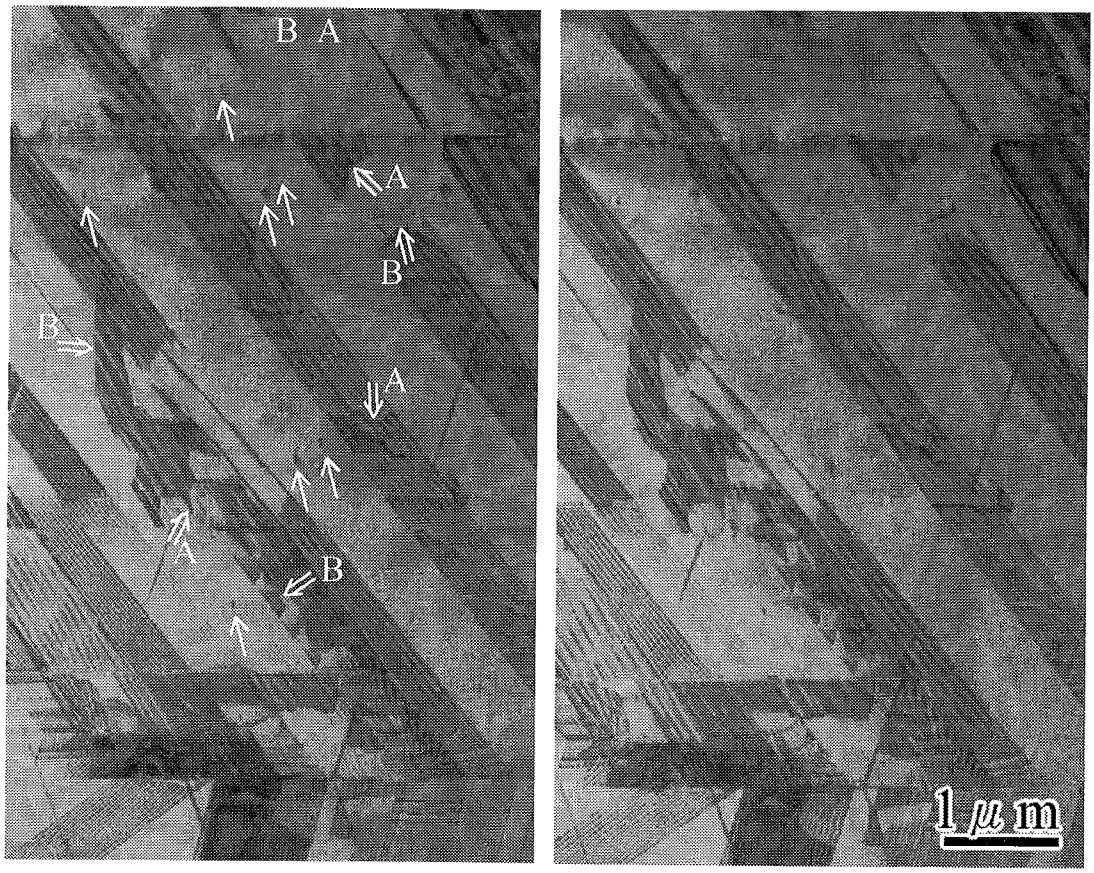
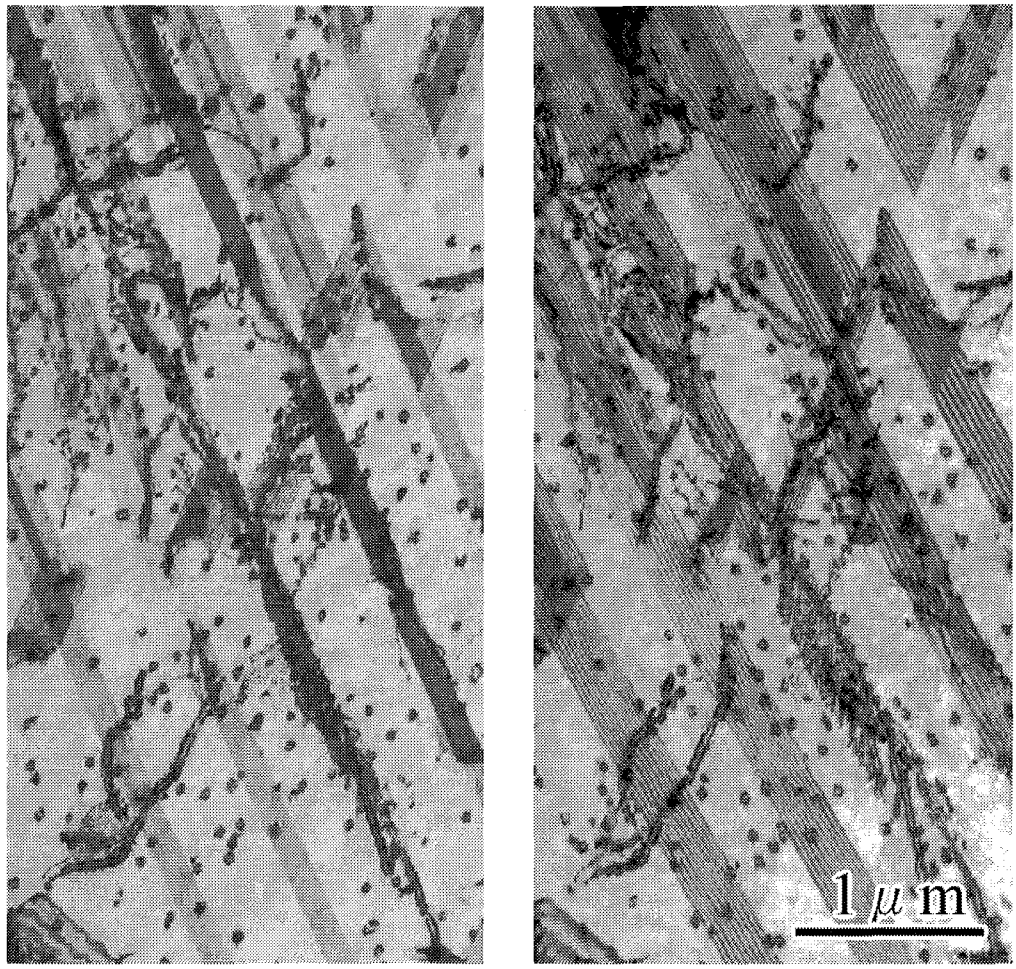


Figure 4-1

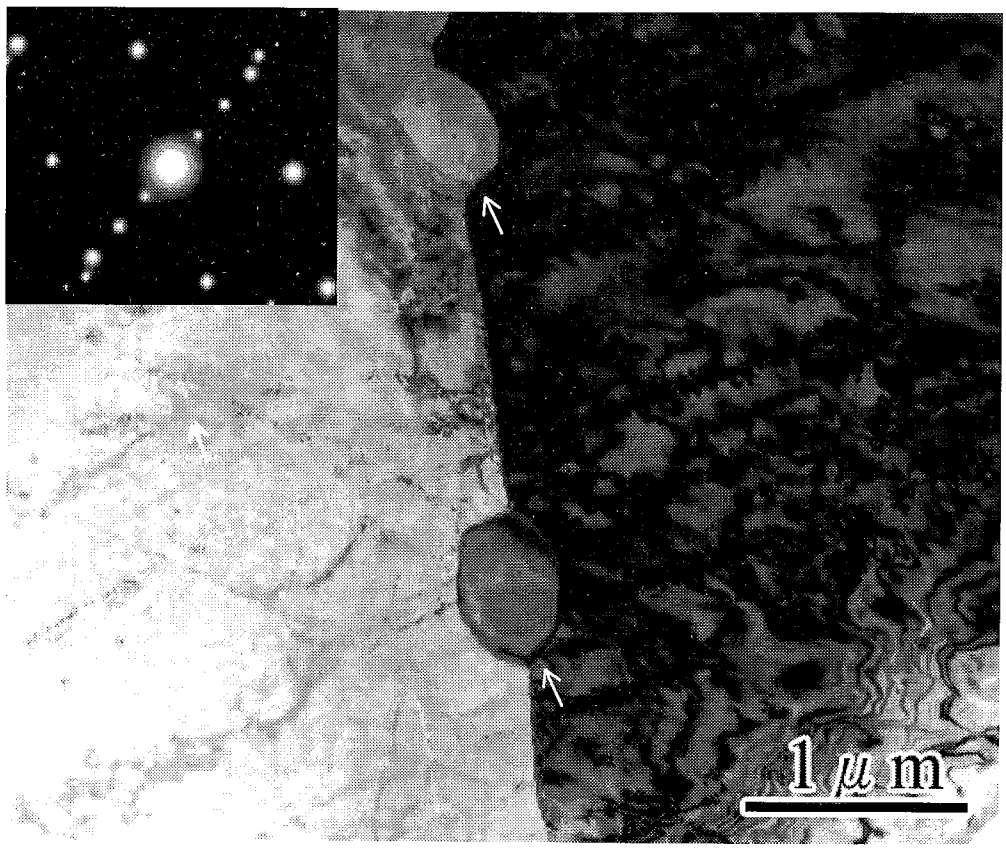
A stereo pair of micrographs showing the residual ε phase plates and small VN precipitates in the as solution treated specimen A. The double arrows note two types of partial dislocations A and B, where A is to remove and B is to form the stacking faults.



(a)

Figure 4-2

Microstructures of a specimen aged at 1073 K (specimen B), showing ε phase plates and well grown VN precipitates by a stereo pair in (a) and the hardly deformable domains formed along a grain boundary.



(b)

Figure 4-2



Figure 4-3

Introduction of the hardly deformable domains into the γ phase matrix with refined grains by the hammering and annealing in specimen F (Table 4-II).

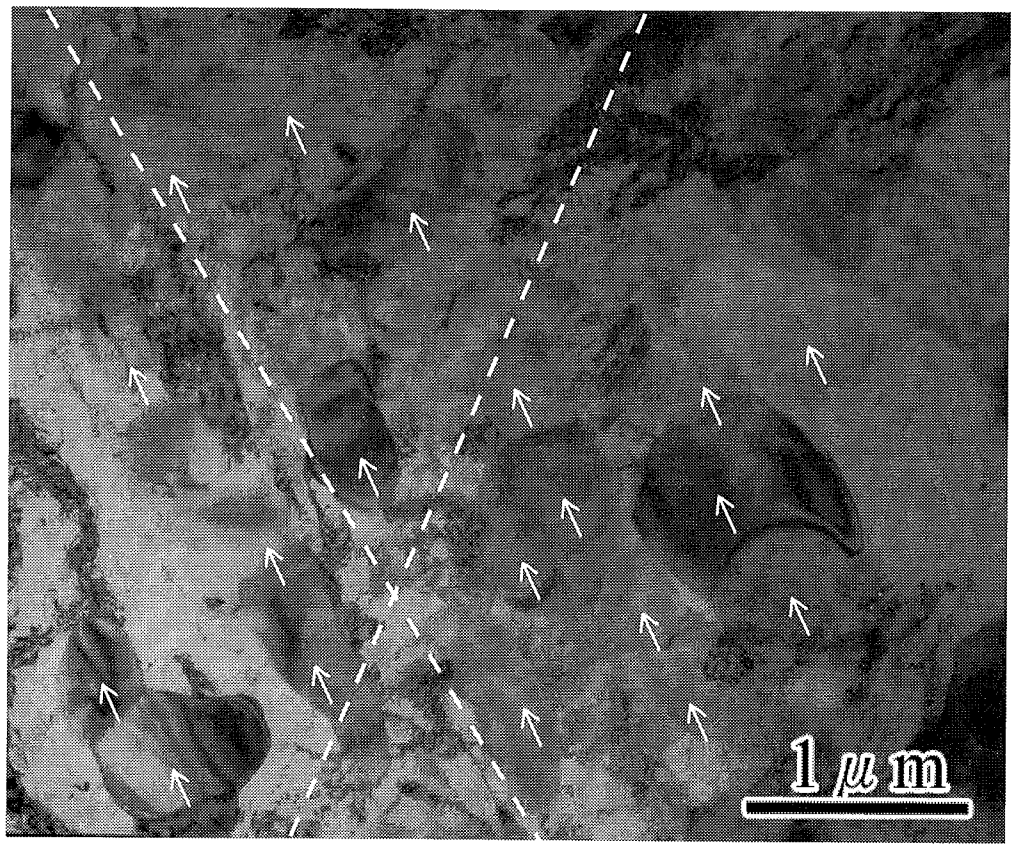


Figure 4-4

Introduction of the highly populated non-deformable domains in the same specimen F as in Figure 4-3. Preferential nucleation of the non-deformable domains is apparent at the intersections of the deformation bands, presumably existed before annealing as shown traced by dashed lines.



Figure 4-5

The cleaned γ phase matrix and the hardly deformable domains in the specimen H, annealed at 1173 K after hammering. Decrease in the strength of the specimen G is found to come mainly from the structural recovery in the matrix by dislocation annihilation.

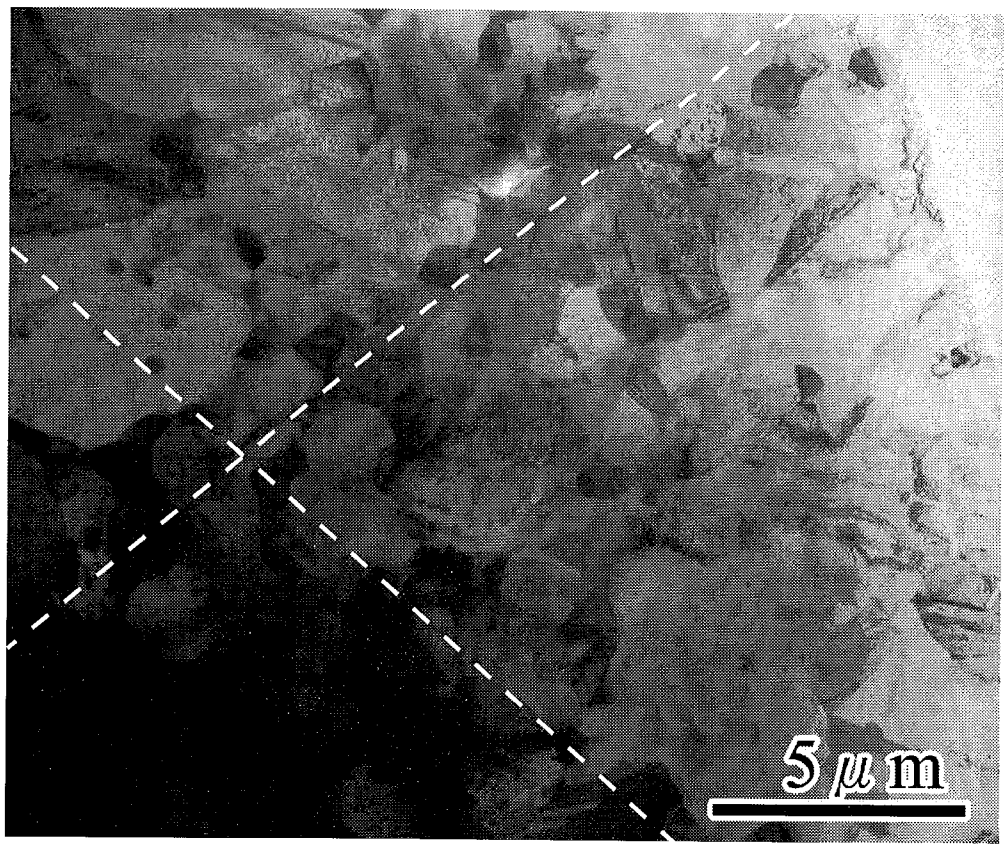
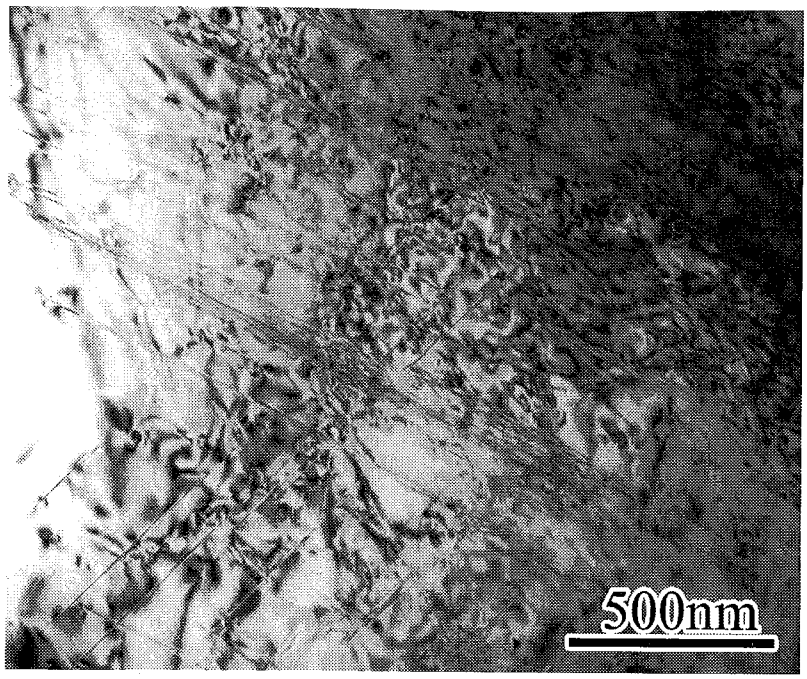
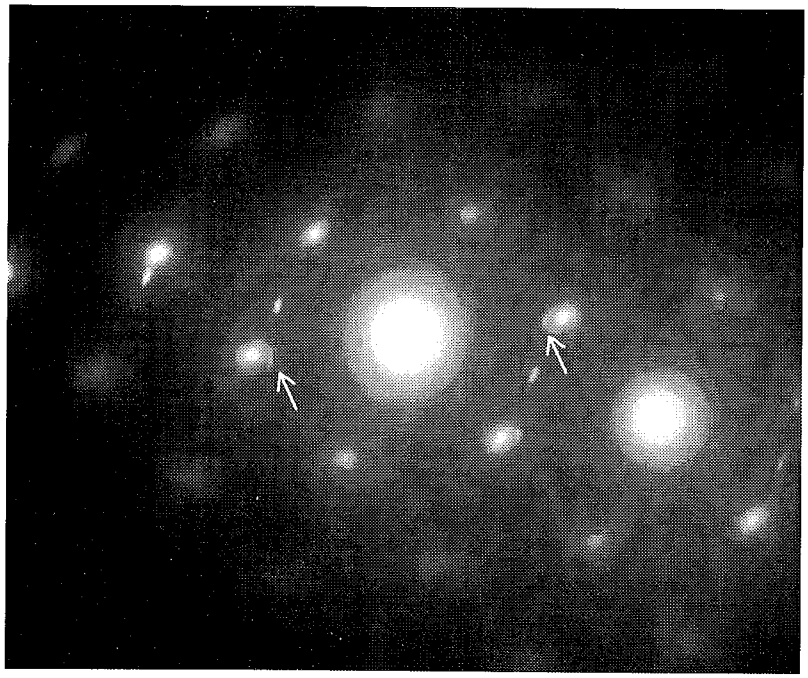


Figure 4-6

A low magnification micrograph of the specimen H, the same specimen as in Figure 4-5. Notable change was not found in the hardly deformable phase in comparison with that annealed at 1073K. Deformation bands existed before annealing are traced by dashed lines.



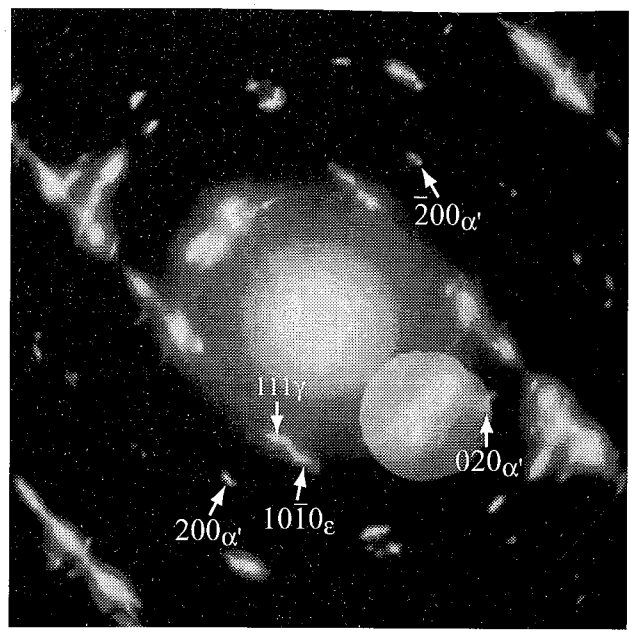
(a)



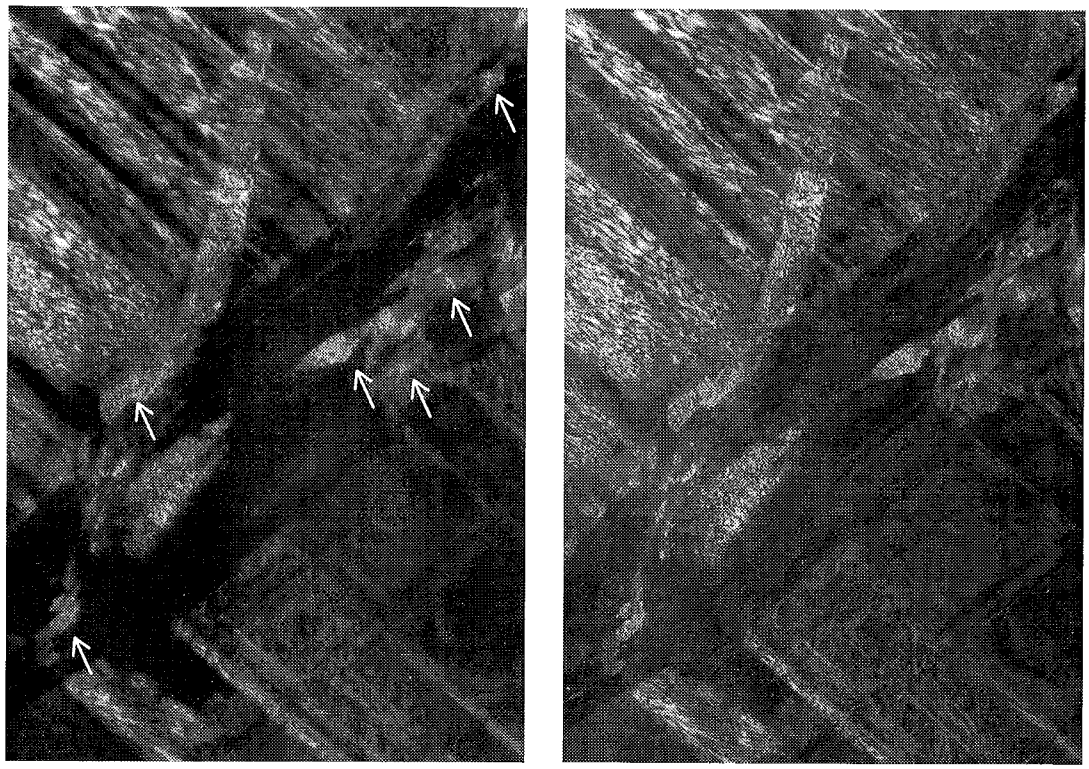
(b)

Figure 4-7

Introduction of finely distributed VN precipitates and thin ε plates in higher density, causing suppression of the formation of the hardly deformable domains in (a) in the specimen I. The small spots arrowed just inside the 200 spots in (b) are of the VN precipitates satisfying the cube-to-cube orientation relationship [6].



(a)

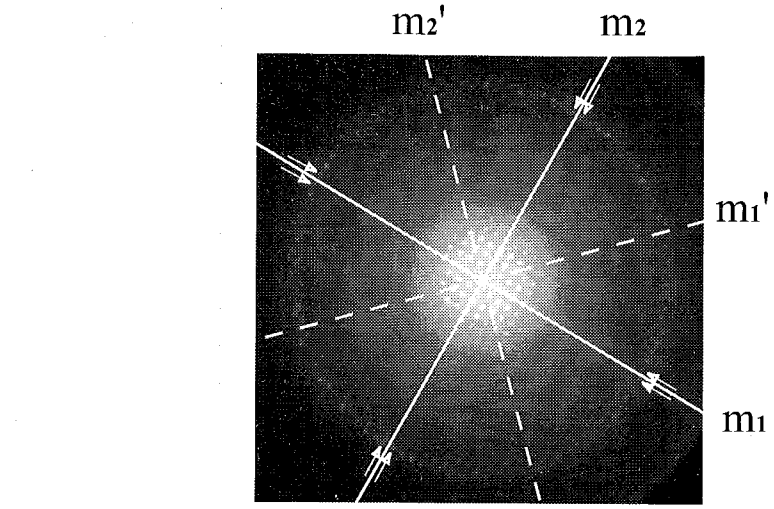


(b)

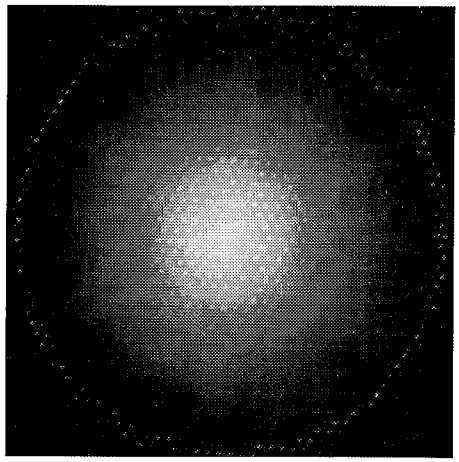
500nm

Figure 4-8

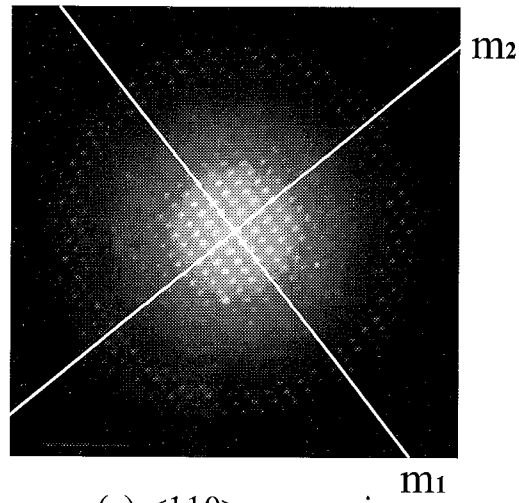
Diffraction pattern (a) and the microstructure (b) in the specimen J deformed to 27 % by hammering. The images arrowed in (b) were identified as bcc phase by the defocused pair of dark field micrographs taken by the spots marked in (a), according to the $2\frac{1}{2}$D method [5]. Some of the spots from γ (fcc), ε (hcp) and α' (bcc) are denoted with their indices.



(a) <001 > zone axis



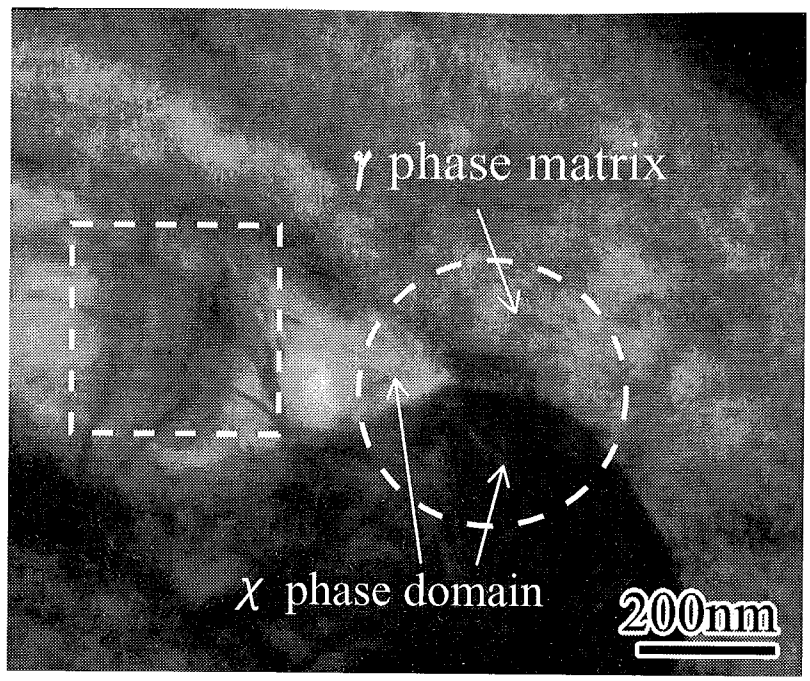
(b) <111> zone axis



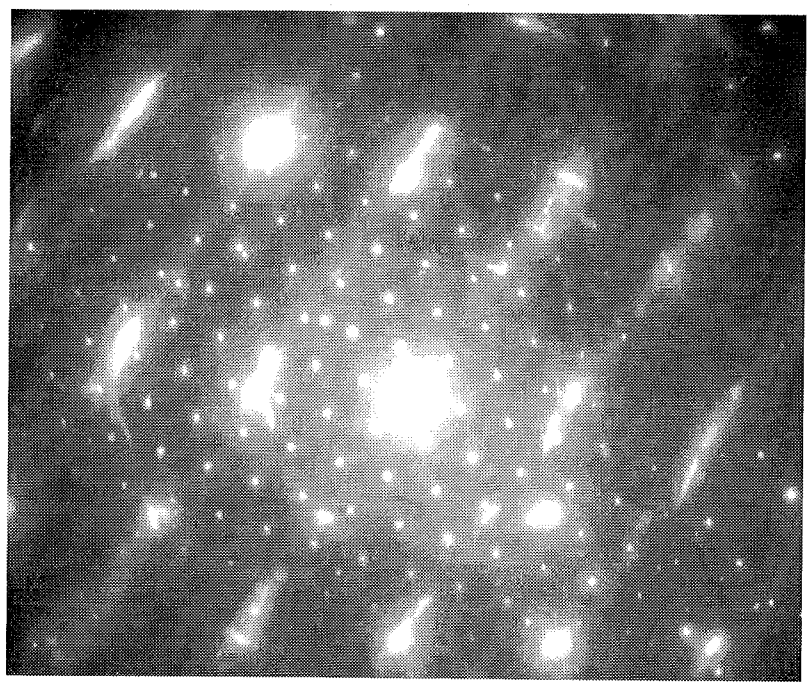
(c) <110> zone axis

Figure 4-9

Micro-diffractions obtained from the hardly deformable domains viewed along the three different zone axes <001>, <111> and <110> for (a), (b) and (c), respectively. See text for detailed explanation in identifying the space group of the $I\bar{4}3m$.



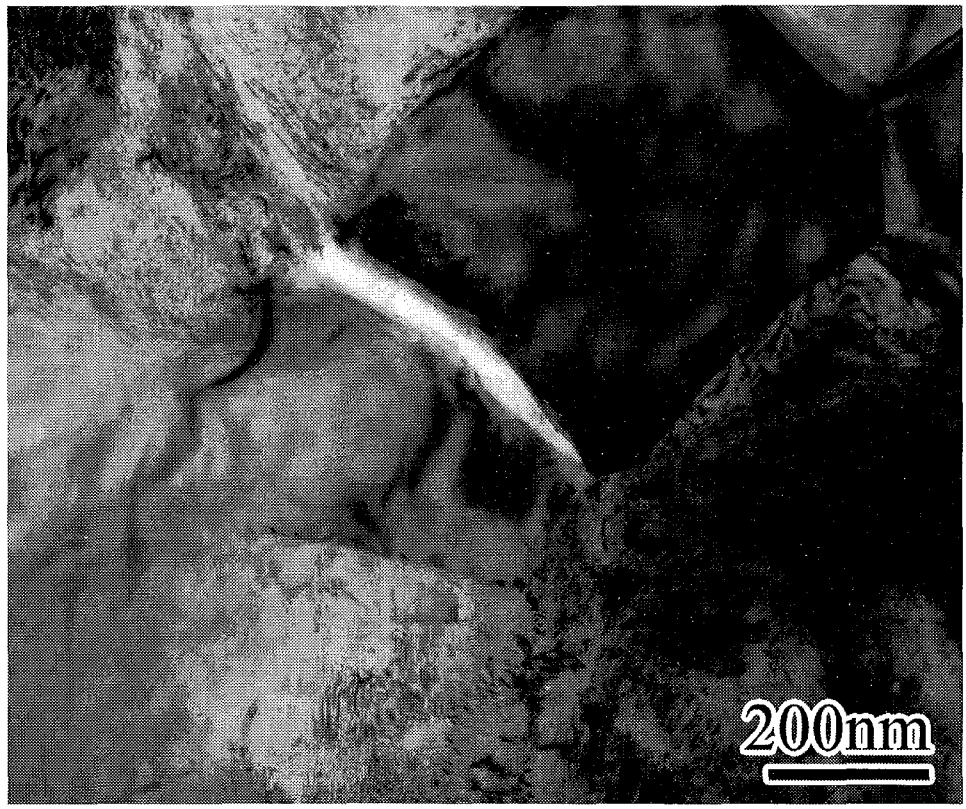
(a)



(b)

Figure 4-10

Variation in the structure at different stress levels in the semi-in-situ deformation; (a) and (b) after loading to 700 MPa and (c) to 1.2 GPa. Fine diffraction spots in (b) having a large unit cell parameter are coming from the two χ phase domains pointed by arrows in the encircled area in (a). It is apparent from the bright area surrounded by a square in (a) that the χ phase is free from dislocations. The hardly deformable χ phase was cracked at this stress level, although the stress concentration must be taken



(c)

Figure 4-10

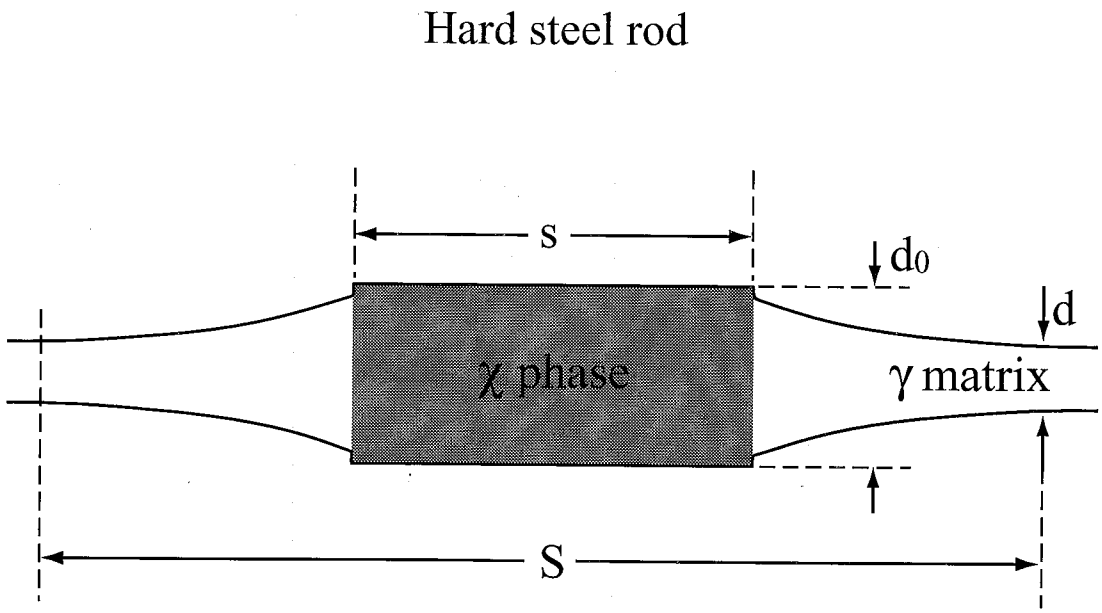


Figure 4-11

Schematic drawing of stress concentration expected at a χ phase domain in the semi-in-situ compression. Absence of the heavily deformed region in the vicinity of the non-deformable phase is important in causing the stress concentration. See text for the detailed explanation.

Chapter 5
Plastic Deformation of Al-$Al_{13}Fe_4$ Thin Foils at Room Temperature

5.1. Introduction

In general, dislocation motion is believed to contribute to the plastic deformation regardless of the crystal structure, including quasicrystals. The plastic deformation is typified by the introduction of planner faults in hardly deformable intermetallics having a large unit cell [1] and in quasicrystals [2] [3]. The dislocation generation as well as motion such a fault is imagined to be difficult and presence of such a fault would prevent motion of other dislocations to restrict the ductility even though dislocations are introduced in these hard materials. It has been demonstrated that some of them become deformable by high speed deformation possibly due to the high compressive stress imposed under constraint [4]. In the high speed deformation, since the dislocation velocity can not exceed the elastic shear wave velocity due to limitation in the increase in the energy [5], the mobile dislocation density is speculated to become extremely high during deformation [6] [7] or the deformation is hypothesized not to be governed by dislocation motion [8] [9]. Moreover, the high speed deformation leaves a question about temperature raise to change the crystal structure by local heating. For example, $Al_{14}Fe_4$ exhibits either amorphous or quasicrystal-like structure in the diffraction pattern after high speed deformation by weight dropping, bullet shooting and ultra-high speed rolling [4]. Thus, it is a difficult task to identify the plastic deformation governed by dislocation motion in a hardly deformable intermetallic compound.

Another possible way to introduce glide dislocations into a hardly deformable crystal is to compress the hardly deformable particles embedded in a ductile material directly as reported previously for Al-Al_3Ni and Al-Al_3Ti [10] [11]. The method used in this study is similar to the above method in the sense that a compressive stress is applied directly to the hard domains surrounded embedded in ductile matrix y use of a thin foil. However, the definite difference is the compression of a thin foil specimen, which has readily been thinned down to a proper thickness observable by HVEM. In the present semi-in-situ method, since the load can be applied on the hard material at a pin point, defects introduced even in the immediate vicinity along the cracked surface can be examined directly without thinning process. Compression of

a foil specimen is also advantageous in detecting the yield or fracture stress of a brittle material under an optical microscope and the deformed areas can be examined repeatedly by TEM. In practice, the HVEM observations were made after the preliminary check of the deformed structure by a 200 kV microscope of either the H-700 or the JEM-2010.

The $Al_{13}Fe_4$ composed of the familiar elements of Al and Fe has been paid some attention as the hardening entity in the Al-Fe alloys [12]. The crystal structure has been studied by several researchers [13] [14] [15] [16]. It is known to have columns of five fold symmetry in a monoclinic unit cell consisting of (13+4) x 6=102 atoms as shown in Figure 5-1. When the monoclinic $Al_{13}Fe_4$ is viewed along the [010] axis, the monoclinic angle is imagined to come from preservation of the four columns with 5-fold symmetry as shown in Figure 5-1(b) in close relation to the 5-fold symmetry of a quasicrystal. Several researchers have reported a method of the Burger vector analysis and the possible directions are considered to be two-, three- or fivefold symmetry axes [17] [18] but without having the periodicity in the three dimensional physical space. Then, dislocation motion without involving diffusion is known to leave phason strain as observed by Takeuchi and Hashimoto [19] [20]. Analogous to such a quasicrystal, the $Al_{13}Fe_4$ having the five fold symmetry columns is speculated to require short range diffusion because of the local disturbance in the periodicity.

Consequently, the deformability must be poor at a low temperature. Nevertheless, it is hoped to be able to detect the plastic deformation at room temperature in the monoclinic $Al_{13}Fe_4$ embedded in Al matrix by means of the semi-in-situ method. A thin foil specimen was compressed to a high stress level and rather uniformly in the small area by use of the thin foil and examined directly without involving thinning process as explained above.

5.2. Experimental Procedures

Compression was given by a special method, semi-in-situ deformation, using a thin foil specimen ready for TEM observation as shown in Figure 2-1. Thin foils were prepared by electrical polishing to perforation in a cooled mixture of perchloric acid and methyl alcohol typically at 243 K. Prior to the final polishing, specimens were jet polished from one side of the surfaces, so that they can be set flat on a polished smooth platform made of Zr_2O. The pressing rod was sharpened to proper size and the area of contact was adjusted by placing a steel foil of proper thickness above the specimen as shown in Figure 2-1. The deformed foils were

examined by a high voltage electron microscope H-1250S equipped with a double-tilt holder capable of tilting by 50°. In this duplex material, the thinning speed in each phase is slightly different and the final thickness varies in a specimen. Moreover, compressive stress tends to act on the thicker area preferentially prior to the thinner area. An electron beam accelerated to 1000 kV enables one to observe such thicker areas when deformed by proper amount. In order to avoid formation of secondary defects by electron irradiation, observation was made at a relatively low magnification of x10000 and cross over condition was avoided in brightness control.

The Al-8wt% Fe alloys were prepared by Sumitomo Light Metals Co. Ltd by means of spray-forming under semi-liquid condition and hot-extrusion to 1/10 in the diameter reduction at 773 K. The chemical composition of the rod was Al - 8.3mass%Fe - 0.1mass%Si - 0.01mass%Cu with its diameter 30 mm. The extruded rods contain high density of small $Al_{13}Fe_4$ particles of 10 nm in diameter in fine-grained Al matrix. Since these small particles were not deformable even by compression of a thin foil under a high stress, it was further annealed at 973 K just above a eutectic temperature of 928 K for 3 hr to grow the $Al_{13}Fe_4$ particles to (2~3) x 10 x 100 μm^3 in the typical size. The thin foil specimens for HVEM observation were prepared by cutting and grinding the annealed rod into 3 x 3 x 0.1 mm^3, jet polishing from one side of the sheet and finally polishing to perforation in a mixture of one part of perchloric acid and 9 parts of methyl alcohol at 60~25 V and at 217 K.

5.3. Experimental Results and Discussions

5.3.1. *Atomic structure of $Al_{13}Fe_4$*

Unit cell of a common intermetallic compound of $Al_{13}Fe_4$ (Al_3Fe) is reported to contain (13+4) x 7=102 atoms belonging to a space group of C2/m [15]. Two unit cells connected along the x-axis are viewed along the three basic axes in Figure 5-1. Note that the plane perpendicular to the z axis drown by broken lines is not parallel to the x-y plane. The lattice parameters of the monoclinic structure are given by a=1.549 nm, b=0.808 nm, c=1.247 nm and $\beta = 107.7°$ As shown in Figure 5-1(b), the structure is composed of atom clusters forming a five symmetry when it is viewed along the [010] direction. Then, the angle β formed by x and z axes makes approximately $(\pi - \beta) \approx 2\pi/5$.

This compound has a quasicrystal like structure with faulted periodicity [21], having five

symmetry columns in Figure 5-1(b). The factor of 5 in β has an important meaning. Dislocation motion in such a crystal with a large unit is expected to be difficult at room temperature in absence of sufficient thermal assistance and is of present interest. It has been demonstrated that an Al_5Fe_2 phase having low symmetry with a base centered orthorhombic structure has been shown to deform by dislocation motion above 873 K, but is brittle below 773 K [12]. Although $Al_{13}Fe_4$ of a monoclinic structure is brittle at room temperature, it is shown that plastic deformation certainly takes place prior to fracture in the semi-in-situ experiments of a foil specimen.

5.3.2. *Dislocations and planner faults induced by heat treatments*

The $Al_{13}Fe_4$ particles grown in the annealed specimens were often composed of twinned variants as shown in Figure 5-2. The low magnification picture in (a) shows an example of the $Al_{13}Fe_4$ particle with the (010) face oriented nearly along the foil surface. As it is apparent from the V shaped facets at the top, the crystal is composed of twin related portions separated by the (100) plane starting at the bottom of the V mark and running vertical in the figure.

In general, the $Al_{13}Fe_4$ particles were composed of planner faults as shown in (b) viewed nearly along the [010] direction at the different particle. The faults and twinned variants are directed mutually at an angle of the multiple of $\pi/5$ as in the low magnification micrograph in (a). It has become apparent from the twins viewed edge on in the figure that there is wide distribution in the thickness reaching as thick as 1~5 μm. The diffraction pattern taken at the boundary marked by a circle in Figure 5-2(b) is shown in Figure 5-2(c). The twines introduced in the heat treatment for growing the $Al_{13}Fe_4$ contain planner faults, which are frequently curved in zigzag form as in Figure 5-2(d) with different width at the steps, indicating cross slipped structure. At the ends of the faults, partial dislocations are attached as shown in Figure 5-2(e) with weak and straight contrasts. The weak and straight images differ from the other dislocations introduced by plastic deformation shown later. The fault planes in the $Al_{13}Fe_4$ composed some of the (100), (001), $(\bar{2}01)$, (605) and $(50\bar{7})$ planes forming the typical angle of $\pi/5$ as shown schematically in Figure 5-2(f).

Except the planner faults and partial dislocations stopped at other faults, neither the concentric dislocation loops reported in the previous study [22] nor the grown in perfect dislocations were found in the as annealed specimen. For the purpose of comparison with the

dislocations introduced by deformation shown later, the set of circular loops found in the previous study are shown in Figure 5-3. They are speculated to be introduced under special condition by thermal stress upon cooling after annealing at 973 K. The dislocations shown below after deformation were quite different in the configuration as well as in the contrast from the circular loops shown in Figure 5-3.

Similar sets of circular dislocations have also been observed in the hardly deformable intermetallic compound of Al_3Ni after high-speed deformation [4]. Although circular dislocations were not observed in $Al_{13}Fe_4$ after high-speed deformation of a bulk Al-$Al_{13}Fe_4$ composite, dislocations contributed to the high-speed deformation in $Al_{13}Fe_4$ were analyzed to lie on a (110) plane with the Burgers vector along $[1\bar{1}4]$ as shown in Figures 5-4(a) and (b) [23]. The small Burgers vector can also be visualized in Figure 5-4(b) where atomic rows aligned vertical are spaced regularly along the $[1\bar{1}4]$ direction parallel to the horizontal axis in Figure 5-4(b).

5.3.3. *Deformation at 300 K*

An example of HVEM observation of $Al_{13}Fe_4$ deformed in a thin foil is shown in Figures 5-5(a) and (b). Although the micrographs of the same area before deformation are not presented, neither deformation bands nor cracks except planner faults shown in Figure 5-5 were present before the semi-in-situ compression. The stress applied in this test was estimated to be 120 MPa on average from the over all area of contact. The practical stress at the strongest contact must be much higher due to delicate roughness on the surfaces. The slip steps of various heights in the wide range up to 40 nm formed in (a) demonstrate that the $Al_{13}Fe_4$ is deformable at room temperature. Shear planes are viewed edge-on in Figure 5-5(a) and they are (010) planes as indexed in the inset. When the slip plane is inclined with respect to the beam, dislocations become visible as shown in Figure 5-5(b). The fact that they were introduced along the slip planes implies that dislocations tend to be introduced at some sources but not randomly at specimen surfaces. It is general trend that once dislocations are generated somewhere slip proceeds along the slip plane to form a shear band even in a thin foil. For example, the shear planes induced in this type of tests were confirmed to be same as that in a bulk specimen, such as {001} planes for Fe_3Ge [24].

Plastic deformation of the monoclinic $Al_{13}Fe_4$ is typified by the mode II crack in the semi-in situ compression made at 300 K [22]. Figure 5-6 shows the typical structure of the

sheared off region after the semi-in-situ loading to 9 GPa at 300 K. The shear plane contributed to the mode II crack was found by tilting the specimen so as to align the shear planes viewed edge on. Furthermore, in the case of Figure 5-6, it was revealed by examination of the orientation relationship between the separated crystals located top and above the sheared off line that the sheared off plane corresponds to a macroscopic twin boundary similar to that shown in Figure 5-2(a). The type of the sheared-off plane was identified as $(50\bar{7})$ belonging to one of the planes forming the pentagonal column but different from the (001) shown in Figure 5-2(f). The planner faults observed after deformation at 300 K such as shown in Figure 5-6 were judged to be exclusively the ones existed prior to the deformation as found in Figure 5-2. These observations indicate that the crack takes place preferentially along the macroscopic twin boundary and prevents the homogeneous deformation at 300 K.

In Figure 5-6, concentric dislocation-like images were often observed locally along the sheared-off planes. The dislocations, if preserved in the crystal, may be identified by changing the Bragg condition with knowledge of the contribution of the deviation vector **s** to the images [25]. That is, the contrasts coming from the strain field must be differentiated from the phase contrasts such as moiré fringes, bend contours and equal thickness contours (extinction fringes). With this in mind, the images were taken at slightly different tilt angles as shown in the Figures 5-6(a) ~ (c). According to these observations, the concentric circular images, changing the intervals and the positions for the different **s** vector are judged to be of phase contrasts but not of dislocations preserved in the crystal. The dislocation-like images are, therefore, the consequence of the sever displacements took place along the shear planes, presumably carried by the dislocations generated at the center of the concentric fringes.

Strain contrasts possibly coming from dislocations were observed in high density as streams of dark bands near the cracked facets running 5-11 O'clock direction with strong contrasts in (a), loosing the contrasts for the slightly different **s** vectors in (b) and (c). The direction of the streams corresponds to the faults existed before deformation such as shown in Figure 5-2, indicating that they are the reaction products of the dislocations contributed to the deformation and stopped along the faults. However, the individual dislocations contributed to the shear deformation prior to the mode II crack at 300 K could not be identified in this uniform compression.

5.4. Conclusions

$Al_{13}Fe_4$ embedded in Al matrix has been prepared and examined before and after thin foil deformation by a HVEM. The results of observations are summarized as follows.

1) Concentric circular dislocations and planner faults were observed in the non-deformed states.
2) Partial dislocations with fine contrasts were attached to the planner faults and the well grown $Al_{13}Fe_4$ particles were composed of twinned variants with the thickness up to a few μm.
3) The twinning planes were identified to be of the (100), (001) and $(50\bar{7})$ types, among the (100), (001), $(\bar{2}01)$, (605) and $(50\bar{7})$ planes forming the pentagonal columns.
4) Plastic zone was always observed along the mode II crack formed in the semi-in-situ deformation of a thin foil specimen.
5) Dislocations were introduced by thin foil compression in the form of extremely thin slip bands without leaving the images of individual dislocations capable of analyzing the Burgers vector.
6) Cause of the luck of ductility at a low temperature is attributable to the production of a large number of dislocations on the same plane after activation of a limited number of dislocation sources.

References

[1] M. Feuerbacher, M. Heggen and K. Urban, Mater. Sci. Eng. **A 375-377** 84 (2004).

[2] M. Wollgarten, M. Bartsch, U. Messerschmidt, M. Feuerbacher, R. Rosenfeld, M. Beyss and K. Urban, Phil. Mag. Lett. **71** 99 (1995).

[3] R. Wang, M. Feuerbacher, W. Yang and K. Urban, Phil. Mag. **A 78** 273 (1998).

[4] N. Yoneyama, S. Kumai, A. Sato, M. Komatsu and M. Kiritani, Rad. Eff. & Defects in Solids **157** 109 (2002).

[5] A. H. Cottrell: Dislocations and Plastic Flow in Crystals (Oxford University Press, London, 1965, 6th Ed.) pp41.

[6] P. C. Johnson, B. A. Stein and R. S. Davis, J. Appl. Phys. **33** 557 (1962).

[7] G. E. Duval, and R., A. Graham, Rev. Mod. Phys. **49** 523 (1977).

[8] M. Kiritani, Y. Satoh, Y. Kizuka, K. Arakawa, S. Arai and Y. Shimomura, Phil. Mag. Lett. **79** 797 (1999).

[9] Y. Shimomura, K. Sugio and M. Kiritani, Computational Materials Science **14** 97 (1999).

[10] K. Yamashita, I. Fujimoto, S. Kumai and A. Sato, Mater. Trans. JIM **39** 824 (1998).

[11] K. Yamashita, I. Fujimoto, T. Murakumo, S. Kumai and A. Sato, Phil. Mag. **A 80** 219 (2000).

[12] S. Hirose, T. Ito, M. Makita, S. Fujii, S. Arai, K. Sasaki and H. Saka, Intermetallics, **11** 633 (2003).

[13] P. J. Black, Acta Crystal. **8** 43, 175 (1955).

[14] K. K. Fung, X. D. Zou and C. Y. Yang, Phil. Mag. Lett. **55** 27 (1987).

[15] J. Grin, U. Bukhardt and M. Elluner, Zeitshrift fur Kristallographie, **209** 479 (1994).

[16] C. Beeli, Mater. Sci. Eng. **A294-296** 23 (2000).

[17] M. Bourdard, M de Boissieu, C. Janot, G. Geger, C. Beeli, H-U. Nissen, H. Vincent, R. Ibberson, M. Audier and J. M. Dubois, J. Phys.: Condens. Matter **4** 10149-10168 (1992).

[18] M. Rosenfeld, M. Feuerbacher, B. Baufeld, M. Bartsch, M. Wollgarten, G. Hanke, M. Beyss, U. Messerschmidt and K. Urban, Phil. Mag. Lett. **72** 375 (1995).

[19] S. Takeuchi and T. Hashimoto, Jpn. J. Appl. Phys. **32** 2063-2066(1993).

[20] M. Wollgarten, H. Saka and A. Inoue, Phil. Mag. **A 79** 2195 (1999).

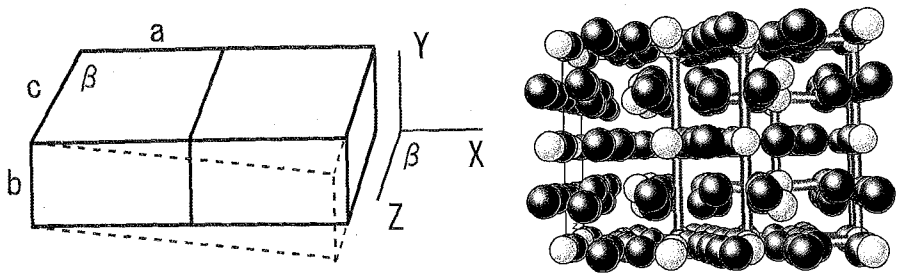
[21] K. Saitoh and M. Tanaka, J. Alloys Comp. **342** 130 (2002).

[22] S. Miyazaki, A. Kawachi, S. Kumai and A. Sato, Mat. Sci. Eng. **A 400-401** 294 (2005).

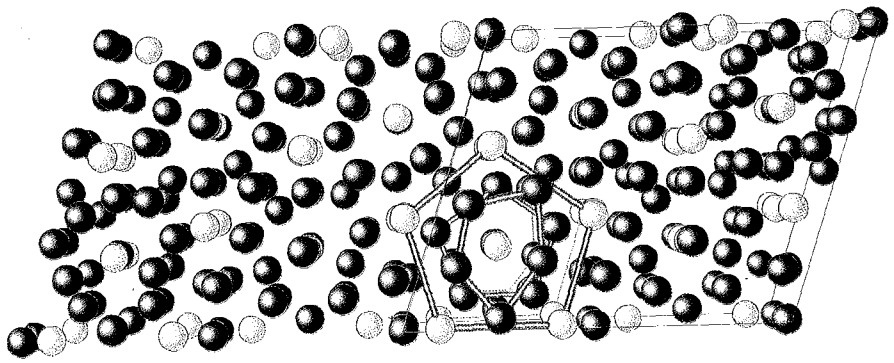
[23] N. Yoneyama, K. Setoda, S. Kumai, A. Sato, M. Komatsu and M. Kiritani, Mat. Sci. Eng. **A 350** 125 (2003).

[24] M. Taniguchi, K. Morizumi, S. Miyazaki, S. Kumai and A. Sato, Phil. Mag. (2005) in press.

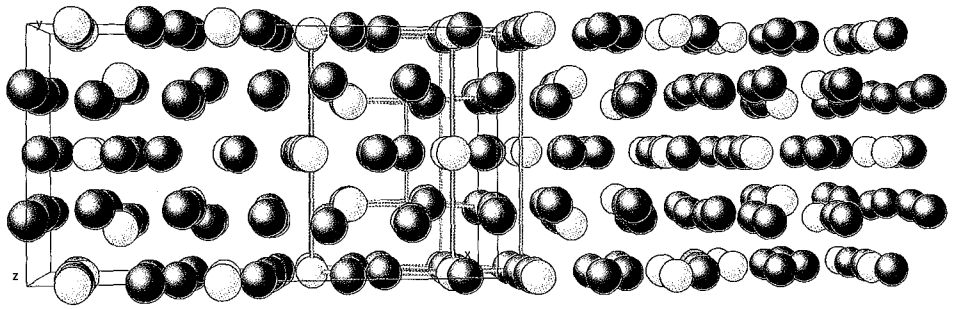
[25] P. B. Hirsch, A. Howie, R. B. Nicholson, D. W. Pashley, and M. J. Whelan, Electron Microscopy of Thin Crystals (Butterworth & Co. Ltd., London, 1971) p. 247.



(a) ⊙ X axis [100]



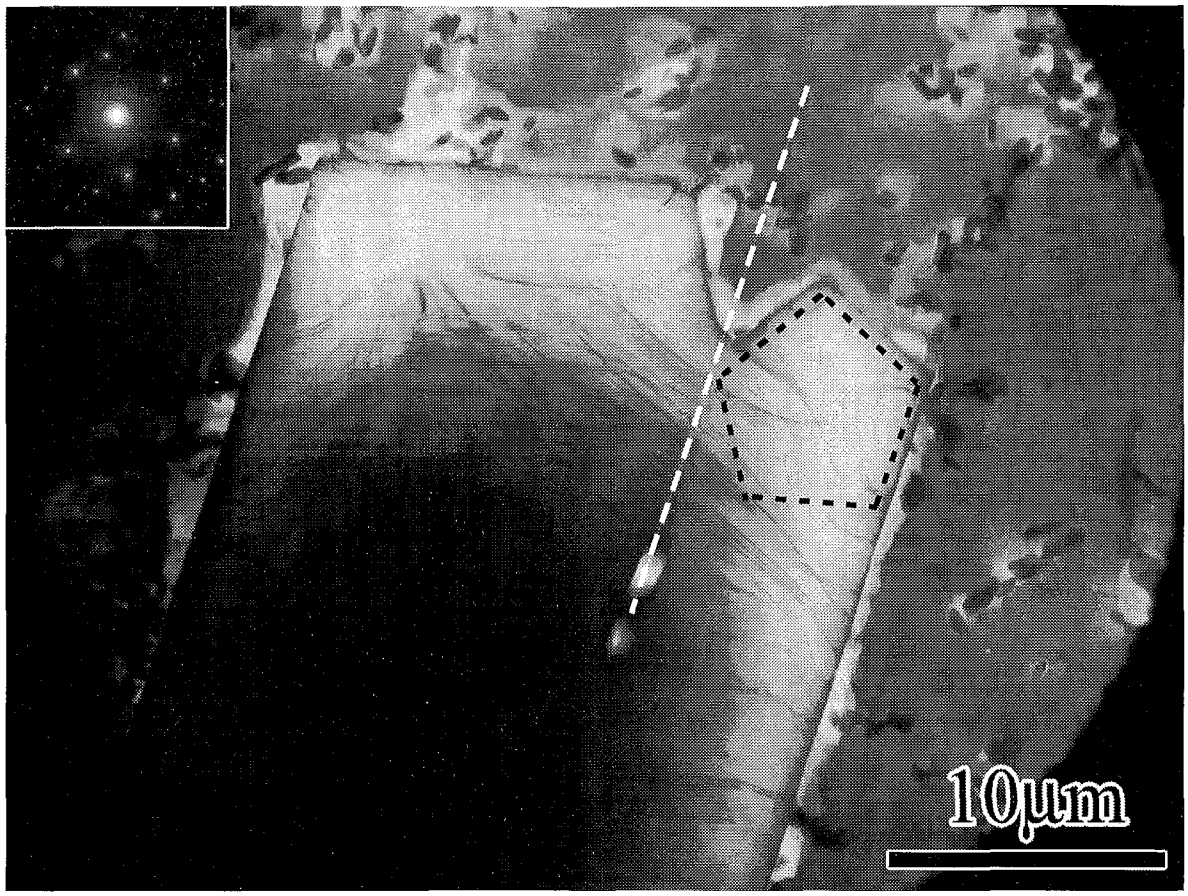
(b) ⊙ Y axis [010]



(c) ⊙ Z axis [001]

Figure 5-1

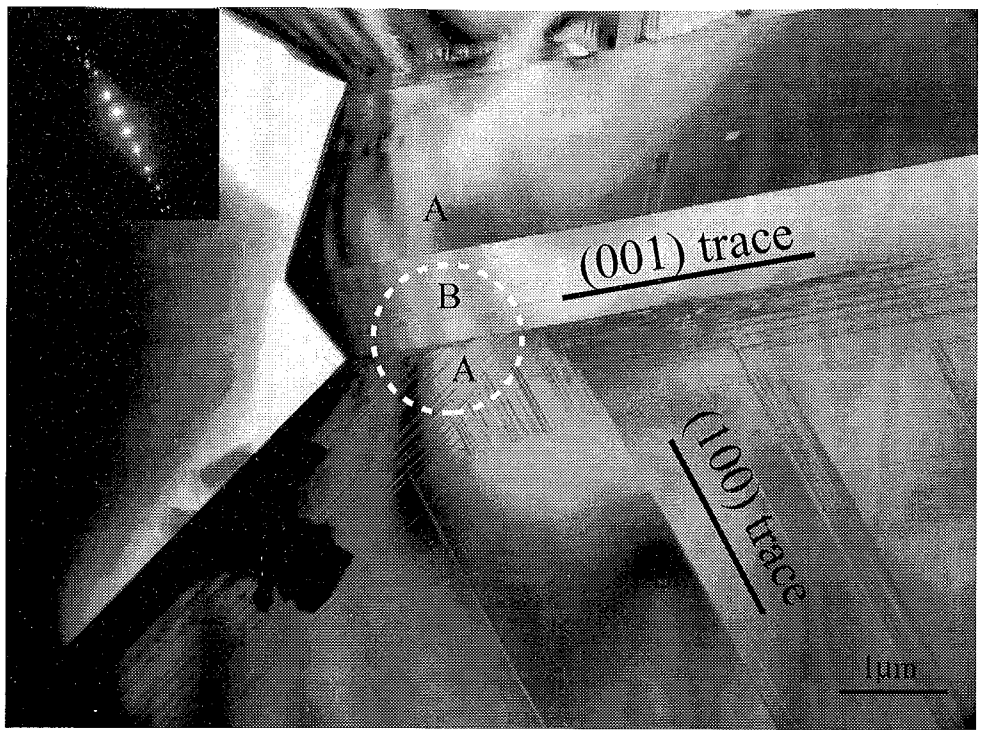
Atomistic structure of an $Al_{13}Fe_4$ belonging to C2/m space group viewed along (a) x//[100], (b) y//[010] and (c) z// [001] axes.



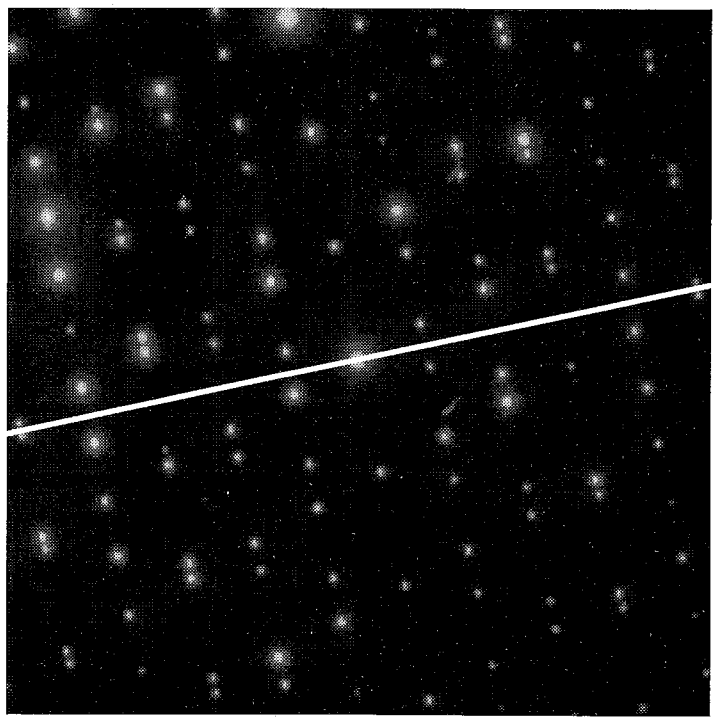
(a)

Figure 5-2

Microstructure of $Al_{13}Fe_4$ particles grown to large size by annealing at 973K. (a) Low magnification micrograph showing the facetted structure. (b) (100) twins observed in as-annealed $Al_{13}Fe_4$. (c) Diffraction patterns taken at the A/B twin boundary of (b). (d) Planar faults and zigzag steps formed by different variant of faults in the as-annealed $Al_{13}Fe_4$. (e) Sharp and faint contrasts at the ends of planner faults in the as-annealed $Al_{13}Fe_4$. (f) A model crystal is viewed along the [010] axis showing the indices of the planes forming the pentagonal columns.

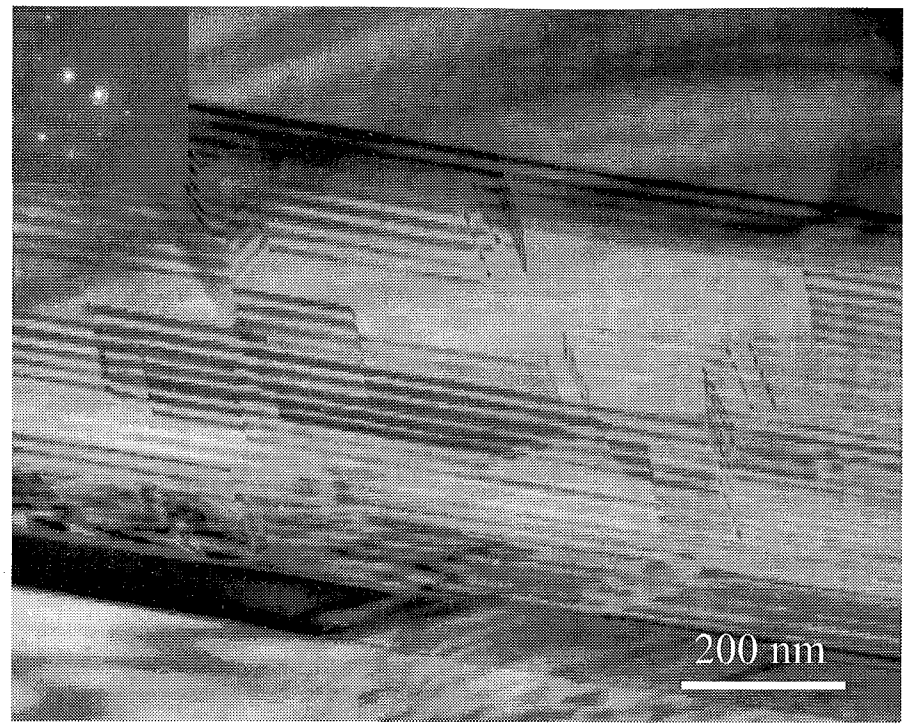


(b)

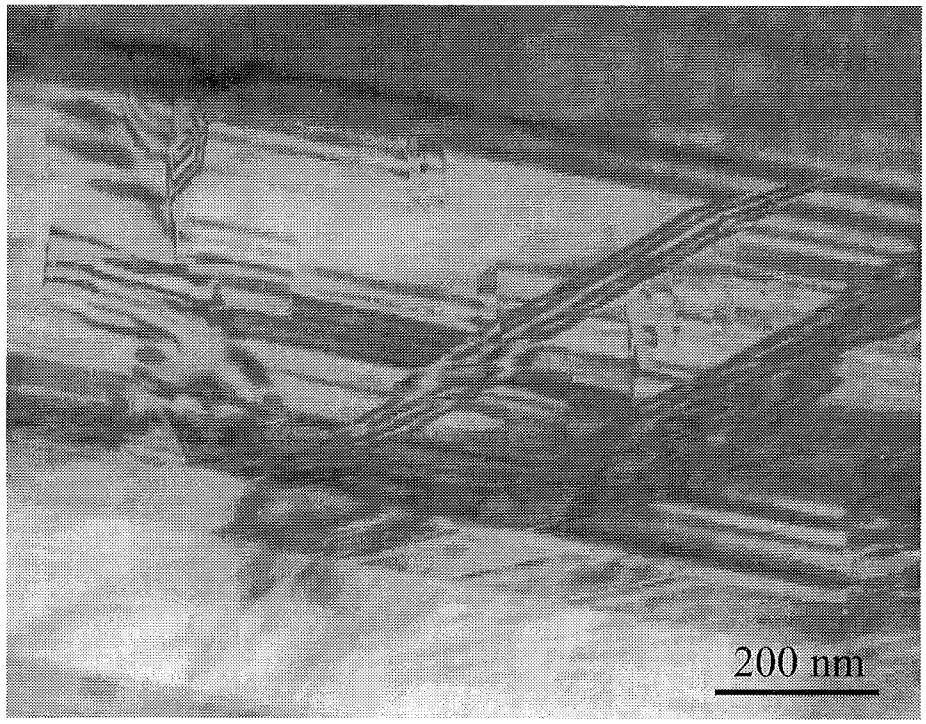


(c)

Figure 5-2

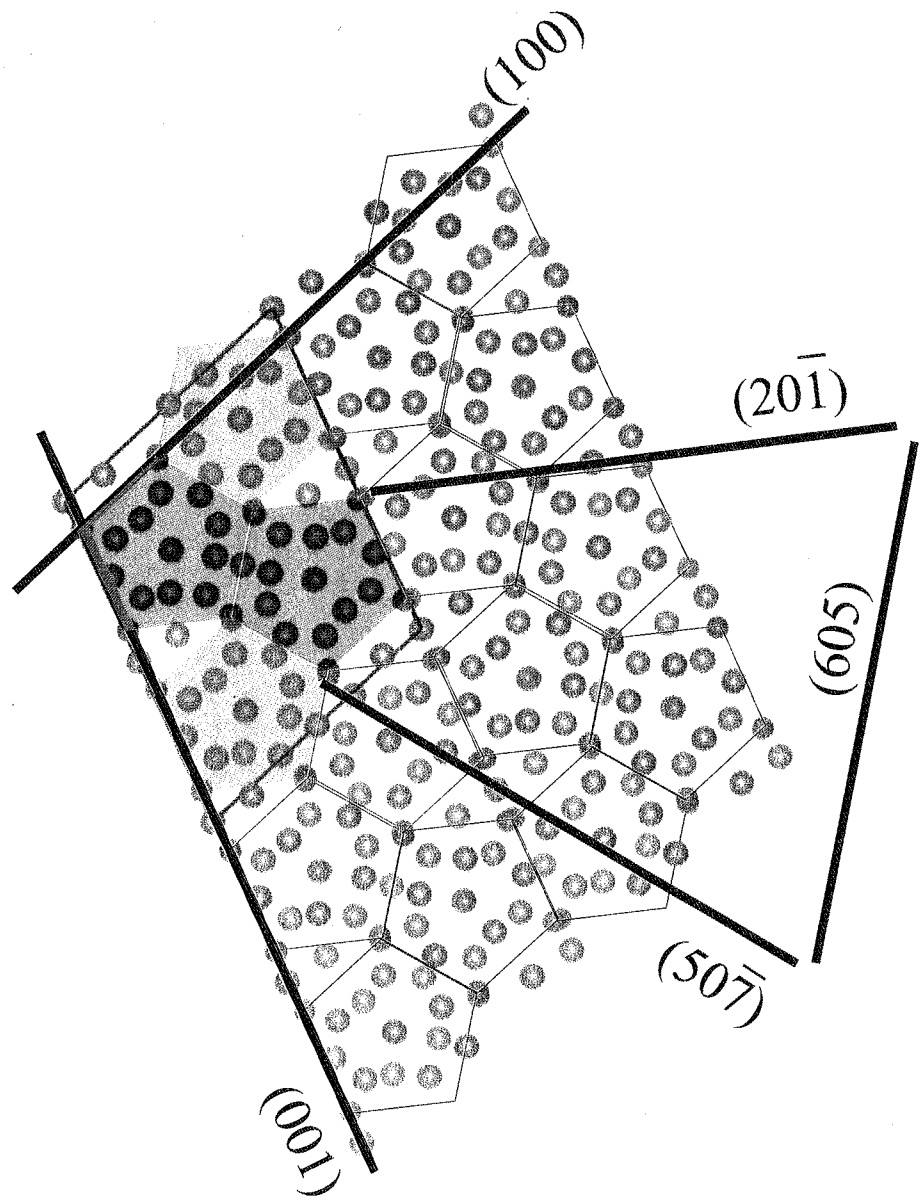


(d)



(e)

Figure 5-2



(f)

Figure 5-2

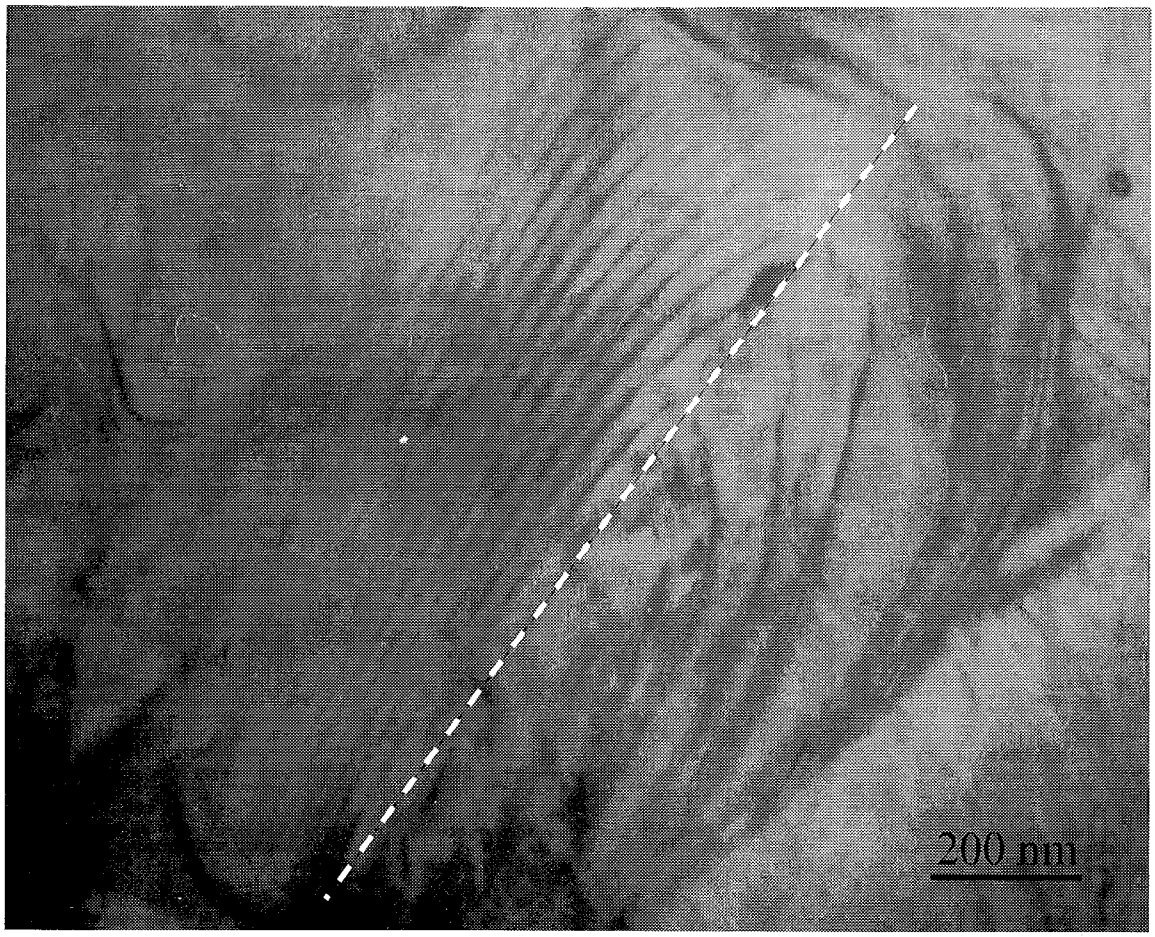


Figure 5-3

Concentric deformation loops, presumably introduced in the course of heat treatment prior to deformation. White line indicates a boundary between $Al_{13}Fe_4$ phases.

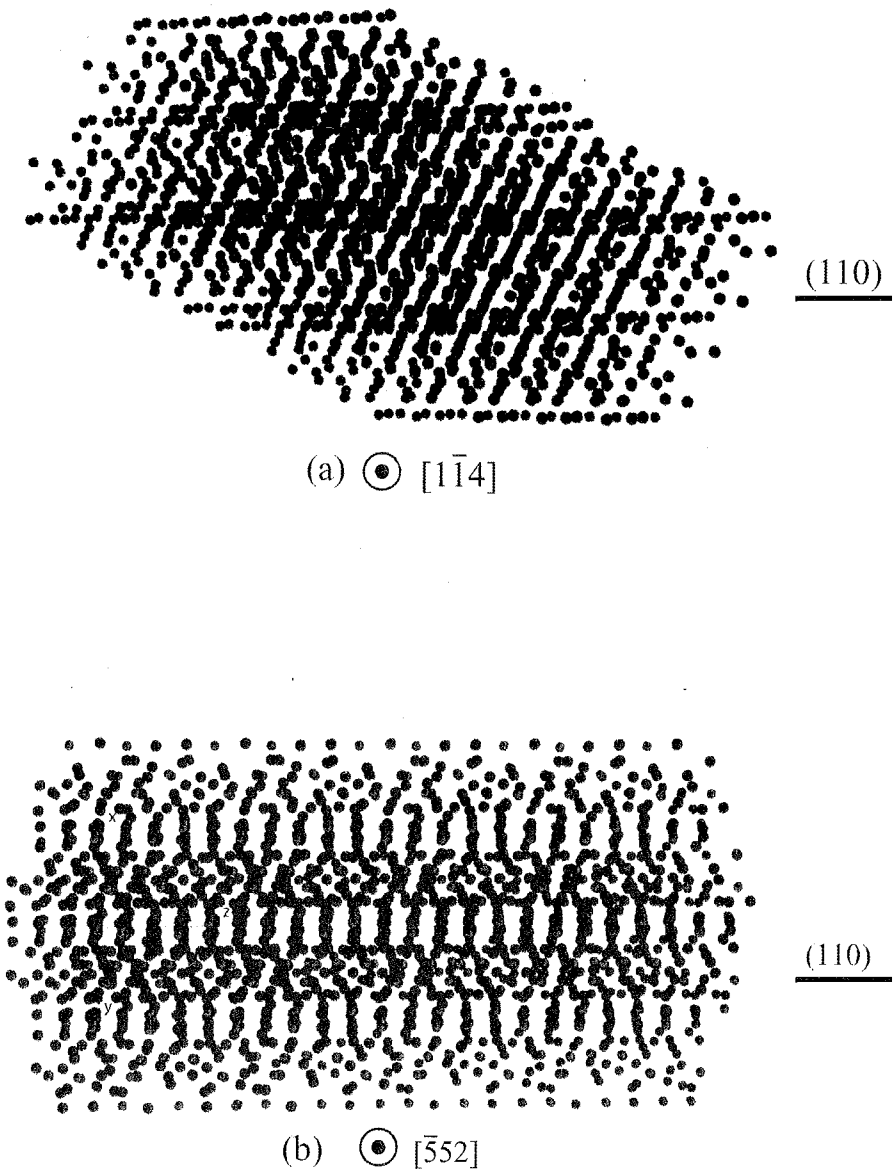
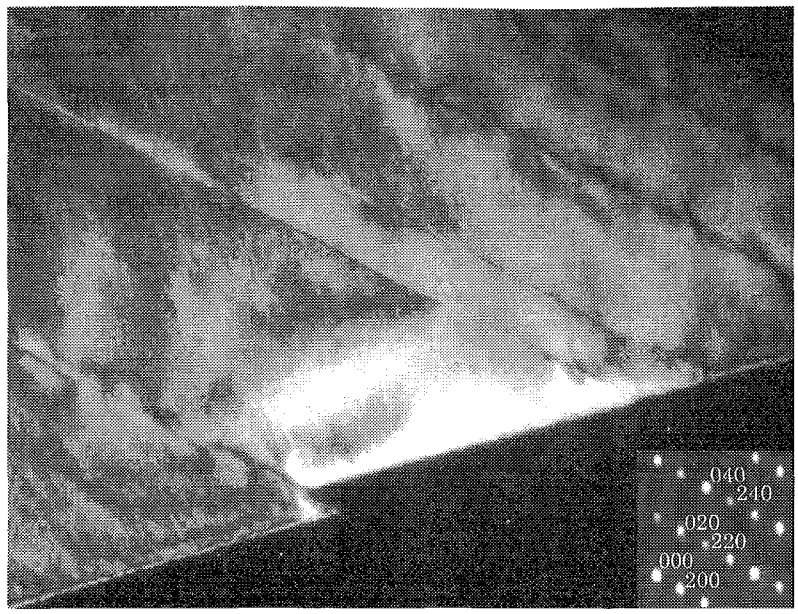
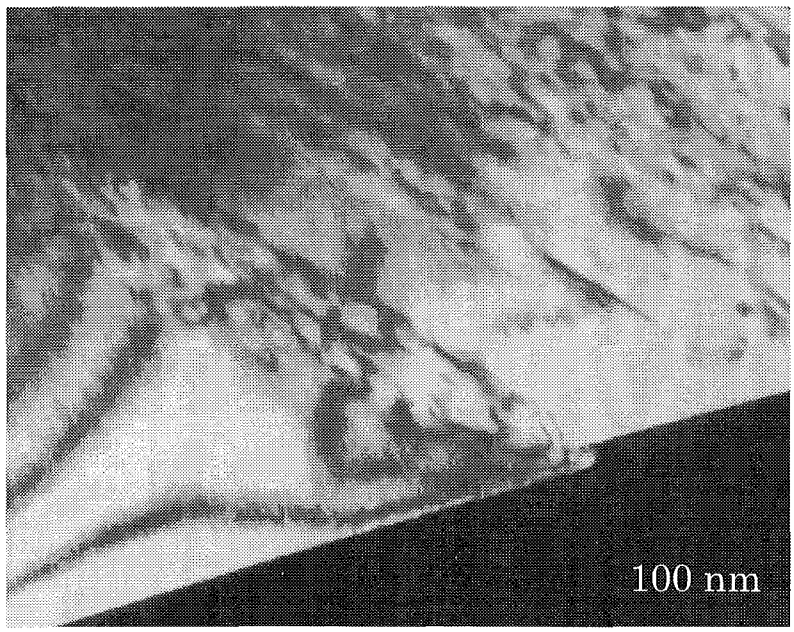


Figure 5-4

A shear system reported for an $Al_{13}Fe_4$ after high-speed deformation [23]. The atomic arrangement is viewed along (a) [1$\bar{1}$4] and (b) [$\bar{5}$52] directions, whereas the (110) slip planes are viewed edge on in both of the figures (a) and (b).



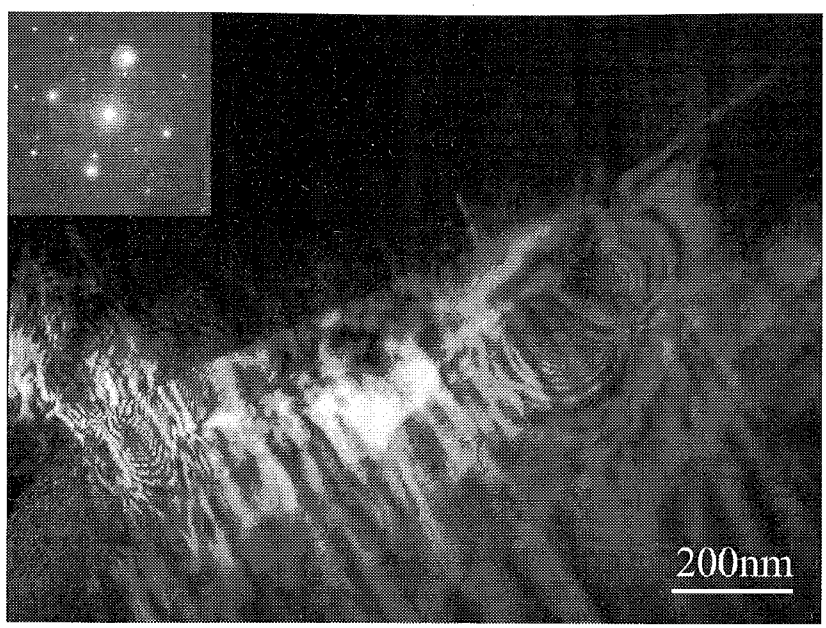
(a)



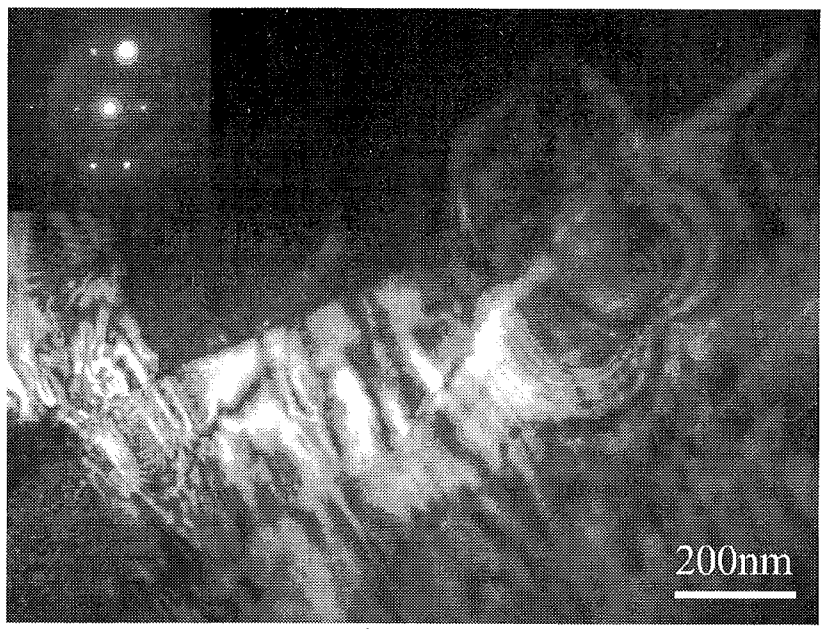
(b)

Figure 5-5

Shear deformation induced by thin foil compression. (a) Shear planes are viewed edge on and beam direction is [001]. (b) Shear planes are inclined to have width so that dislocations become visible along the shear planes.



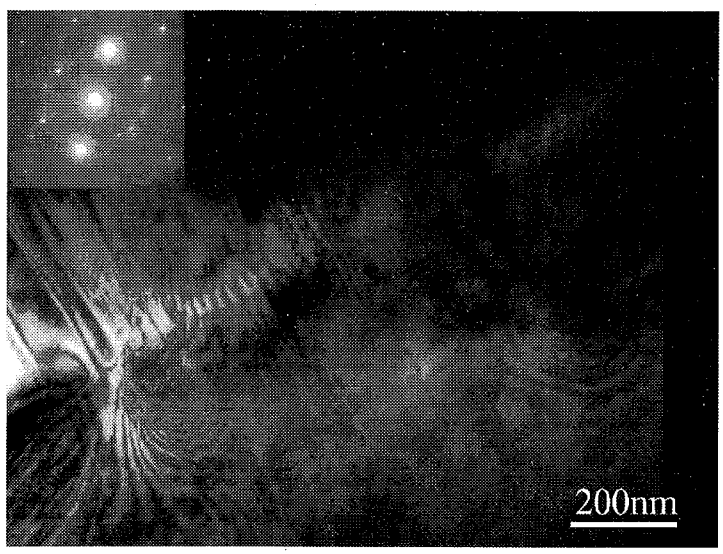
(a)



(b)

Figure 5-6

Defects structures observed along a mode II crack induced by the semi-in-situ compression made at 300 K. The nearly uniform stress applied by the apparatus shown in Figure 2-1 is estimated to be 9 GPa. Note that the small change in the s vector by tilting alters the defect images as well as the fringe patterns of the phase contrasts drastically in (a), (b) and (c). The sheared off plane inclined with respect to the beam direction was identified to be $(50\bar{7})$.



(c)

Figure 5-6

Chapter 6

Dislocation Generation and the Motion in a Monoclinic $Al_{13}Fe_4$ at 300~873 K

6.1. Introduction

In the previous chapter, the semi-in-situ compression developed in this study was applied a monoclinic $Al_{13}Fe_4$ to explore its deformability. However, the dislocations presumably contributed to the plastic deformation prior to the crack could not be resolved as the individual dislocations after deformation at room temperature as mentioned in Chapter 5. This is due to the extremely high stress needed to generate dislocations and hence they move through the crystal spontaneously. Hence, the observed strain contrasts were of the dislocation clusters even though they were preserved without escaping from the specimen. Thus, it is not easy to detect the dislocations moved under the rather uniform stress, even if they would have contributed to the deformation at a low temperature.

One of the ways adopted in the past to detect dislocation motion is to deform a specimen at a higher temperature. For example, the glide motion is known to be assisted by removal of the phason strains in quasicrystals [1] [2]. In contrast, the dislocation glide is expected to take place more easily in the present monoclinic crystal because of the periodicity in the physical space. The semi-in-situ compression test will be attempted at higher temperatures with an expectation that the dislocation glide may be assisted by atomic diffusion. It is aimed here to verify the shear systems as well as the dislocation motion involved in the plastic deformation of the monoclinic $Al_{13}Fe_4$.

Meantime, it has been shown that stress concentration due to indentation causes dislocation generation and its motion just beneath the mark at room temperature [1] [3]. The literature suggests that the semi-in-situ compression test can be improved so as to preserve the dislocations introduced at a high stress level by designing the appropriate stress condition. That is to utilize a stress concentration imposed at a small region so that the dislocations introduced under the high stress may remain in the foil specimen. A new method of the semi-in-situ compression will be described here and it is hoped that the method will be recognized as a simple but powerful way of examining any brittle materials.

Thus, the test temperature and the stress conditions are changed is this chapter for the purpose of introducing dislocations and preserving them in the semi-in-situ experiments. The

test temperatures are ranged from 300K ($0.21T_m$) to 873K ($0.61T_m$) . The results of the observation will be discussed on the ground of the shear displacements conceivable in the monoclinic $Al_{13}Fe_4$ from the view point of the crystal structure and the atomic arrangements.

6.2. Experimental procedures

An Al-$Al_{13}Fe_4$ composite examined in this chapter is the same as an object treated in the previous chapter. Use of the HVEM was advantageous in examining a thick specimen with ferromagnetic property. Particularly, in analyzing the shear systems, it is important to tilt the foil specimen by a large angle, which increases the thickness as well as the disturbance due to Lorenz force drastically. The limitation in the tilting angle for the present double-tilt specimen holder comes from the thickness of the holder as well as of the specimen. The critical angle is practically determined by the overlapping of the top and bottom pieces of the specimen holder to hide the viewing area. Tilting of a specimen by a large angle can be made by resetting it after trial observation, namely by resetting the specimen to align the tilt axis of interest coincident with the tilt axis installed on the specimen holder since there is no limitation in setting the tilt angle around this axis. In a special case, the orientation of the area of interest can be tilted at any angle by bending the foil specimen locally before resetting after preliminary observation. Since the aluminum matrix is much weaker than the $Al_{13}Fe_4$, the local bending could easily be practiced, for example, to bring the shear plane viewed edge-on.

The apparatus used for the semi-in-situ compression is shown in Figure 2-1. Because of the use of a thin foil specimen with a hole, stainless foils were placed over the specimen to apply a stress not concentrated at a pin point. In order to deform the $Al_{13}Fe_4$ located near the periphery of the hole, a Vicker's hardness tester was used as shown by a magnified view in Figure 2-1. The deformation temperature was controlled by use of a hand made small furnace capable of surrounding the compression apparatus during compression tests. The stress was estimated from the area of a dimple mark put on the specimen and the load was measured by the weighing device placed below the specimen platform (Figure 2-1).

In examining the as-deformed structure of a hardly deformable material, it is important to make the observation directly without electro polishing, since it was revealed that the deformed areas were polished away preferentially, especially near the dislocation sources. The difficulty encountered in the semi-in-situ compression was the pasting of the specimen onto the metal in contact with it. One of the procedures succeeded to overcome this difficulty was to evaporate carbon on the surfaces of the stainless foil and the ZrO_2 platform in contact with a thin foil specimen before compression at high temperatures and the other was to put a sandpaper instead of a metallic foil in contact with a thin foil specimen. In the latter case, the hard aluminum

oxide particles of less than several μm in diameter acted as dislocation sources everywhere in the compressed region so that dislocations introduced on various types of shear planes could be examined directly after deformation without electro polishing.

The present method of using a sandpaper is particularly advantageous in introducing dislocations at extremely large number of stress concentration sites of the SiC particles. As a matter of fact, dislocations were introduced into the foil by stress concentration in the areas at contact with the SiC particles and the dislocations generated remained in the region where the stress concentration diminishes at some distance. By this method, examination of the individual dislocations introduced at 300 K and 873 K has become possible.

6.3. Experimental results

6.3.1. *Deformation at 300 K with SiC particles*

After the thin foil deformation made by placing a sandpaper, dislocations emitted at various sizes of the alumina particles were observed as shown in Figure 6-1. The low magnification micrograph in (a) shows the dislocations generated at three different spots of A, B and C noted by arrows. It is apparent for the small indentations A and B that dislocations were introduced only in the immediate vicinity of the particles. In contrast, the straight line running at the top left in (a) is a sheared-off plane possibly started at a large alumina particle, which is supposed to be located far from the sight in the figure. A few groups of dislocations numbered 1~4 in (a) are judged to be generated at the bottom region marked by C under a suitable stress condition induced by the SiC particles of a proper size.

These groups of dislocations were focused and examined by changing the **g** and **s** vectors. At the same time, three-dimensional information was obtained by tilting experiments and by stereo microscopy. The Figures 6-1(b) is a pair of stereo micrographs, showing the four groups of dislocations lie on flat planes. Special care was exercised to avoid contribution of the closely spaced spots upon imaging the dislocations in the present monoclinic $Al_{13}Fe_4$ with a large unit cell. The dislocation contrasts remained rather strong against the change in the **s** vector, indicating that the strain fields of the dislocations are large and hence the magnitudes of the Burgers vectors must be as well. The dark field images taken at a relatively large **s** are shown in Figure 6-1(c). The diffraction spot used for the imaging is shown in the inset with the objective aperture by double exposure and was exposed more than other spots. The strong images observed here differ from the faint and complex images of the dislocations introduced at 873 K as shown later. In order to confirm the shear planes, the groups of dislocations numbered 1~4 were aligned edge-on in Figure 6-1(d). The crystallographic information is given by the indices of a few diffraction spots shown in the inset of the figure. The shear plane

was, thus, identified as $(1\bar{1}0)$ for the dislocations induced at 300 K.

Interestingly, the strain contrast viewed edge-on is not simple, changing the contrasts along the straight lines on the shear plane traces numbered 1~4. This is possibly due to the existence of strain components perpendicular to the slip planes. These dislocations are apparently stopped at planar faults as noted in the faint lines running along 7-13 O'clock direction in Figure 6-1(b) and 8-14 in (c). Although the contrasts are faint, the dislocations stopped at the faults are viewed nearly edge-on at four discrete positions along the shear planes numbered 2 in the figure. The change in the visibility of these dislocations for the different **g** vectors was examined under the geometrical condition adjusted to keep the shear planes viewed nearly flat. From the invisibility for $\mathbf{g}=\bar{5}07$, the Burgers vector of the dislocation operated at 300 K was identified to be directed along [775] on the $(1\bar{1}0)$ shear plane as shown by a stereographic projection in Figure 6-2. In this analysis, it is implicitly assumed that the total Burgers vector lies on the $(1\bar{1}0)$ shear plane.

6.3.2. *Deformation at 473 K*

In the area of the heavy deformation induced at 473 K, the foil specimen was occasionally sheared on multiple planes to have a hole surrounded by facets as shown in Figure 6-3. The extinction contours and moiré fringes observed in Figure 6-3(a) are quite similar to those observed after deformation at 300 K (Figure 5-6). Some increase in the ductility is, however, noted due to increase in the deformation temperature from 300 K to 473 K. One is the occurrence of the multiple shears to form a hall with facets as noted in Figure 6-3(a), instead of breaking along a straight line (Figure 5-6). Another feature is the introduction of the tangled dislocation-like contrasts near the intersection of the shear planes as shown in Figure 6-3(b). It may be related to the operation of the second shear systems, which seems to have suppressed the spontaneous propagation of the mode II type.

However, the individual dislocations contributed to the deformation prior to the type II crack could not be obtained at 473 K under a uniform stress. It is, thus, common behavior that the shear deformation initiated at some origin under a high stress propagates through the crystal spontaneously without leaving the isolated dislocations. This is in contrast to the dislocation structure induced by the SiC particles at 300 K shown in Figure 6-1. A similar but more ductile structure will be introduced at 473 K by use of a sandpaper, although it was not practiced here. In stead, such an experiment was made at 873 K in order to examine the temperature effect on the dislocation generation and the motion as described later.

6.3.3. *Deformation at 673 K*

In the region where the periphery of a hole in the foil specimen was squeezed out by plastic

deformation at 673 K, groups of dislocations contributed to the deformation were observed as shown in Figure 6-4(a). They are free from planar faults and judged to be perfect dislocations. Visibility test was made at a larger magnification for the dislocations observed in the area marked by a broken square 6-4(a) and shown in Figures 6-4(b) and (c). The dislocations accompany strong and wide strain fields in (b). These dislocation images were found to become invisible in (c) for $\mathbf{g}=\bar{1}\,\bar{1}\,0$ except near the surfaces. Another interesting observation is that the set of four dislocations are introduced to form a windmill structure composed of 4 pedal-like contrasts in the top right bound by a white broken square in Figures 6-4(b) and (c). Here again, the residual contrasts at the surfaces in (c) are rater strong in comparison with those of pure metals, indicating that the magnitude of the Burgers vector must be large.

The glide planes were also determined for these dislocations by tilting experiments. Figure 6-5 shows the results of the analysis by stereographic projection where the **g** vector of the invisible condition is given by $(\bar{1}\,\bar{1}\,0)$ and the shear plane viewed edge on is given by (001). Thus, the Burgers vector, presumably lying on the shear plane was identified to be directed along $[1\,\bar{1}\,0]$. This is a reasonable shear system for the compression axis denoted in Figure 6-5 with the Schmidt factor of 0.47. Also the present result is in agreement with the earlier report [4] [5] [6], suggesting that the shear displacement of $[1\,\bar{1}\,0]/2$ is one of the possible Burgers vectors in the monoclinic $Al_{13}Fe_4$. This point will be discussed later in more details together with the information obtained after deformation at 873 K.

6.3.4. *Deformation at 873 K*

Two types of semi-in-situ experiments were made at 873 K by avoiding the fatal damage due to pasting of the specimen. In one experiment the observation was made after electro polishing. The applied stress was 1 GPa and rather uniform in the compressed area in comparison with that given by SiC particles shown later. Although majority of the dislocations disappeared due to electro polishing, isolated dislocations were observed along the faults as shown Figure 6-6. The planes were curved in zigzag form as shown in (a), indicating that motion of the partial dislocations was assisted by cross slip. Typical images of the partial dislocations introduced by deformation at 873 K are shown in Figure 6-6(b). Geometry of the faults induced here by plastic deformation was quite different from those observed in the as annealed specimen (Figure 5-2). That is, the intensity of the dislocation images is stronger and complex in Figure 6-6 than in Figure 5-2. The contrasts may come from the insufficient recovery in the strain field even at a temperature as high as 873 K in comparison with the diffusion assisted structural change observed in the as annealed specimen (Figure 5-2). The shear planes contributed to the deformation were identified as the ones composing the five fold symmetry columns. Although the Burgers vectors could not be identified in these observations,

it is clearly resolved in Figure 6-6(b) that some the partial dislocations are not isolated possibly stopped by the pre-existing faults running along the 10-16 O'clock direction.

Another tests made at 873 K were the observation of the deformed specimen directly without electro polishing. A sandpaper placed over the specimen enabled to preserve the thin foil surfaces clean without contamination even after deformation at 873 K. The stress applied through the sandpaper was 400 MPa and an order of magnitude smaller than 4.0 GPa applied in the case of 300 K (Figure 6-1). This method was especially powerful in introducing dislocations and in preserving them in the immediate vicinity of the dislocation sources. Actually, a quite large number of the SiC particles acted as the stress concentration sites to induce glide dislocations. Figure 6-7 shows several groups of dislocations emitted from the dislocation sources presumably located just beneath the SiC particle of a dark contrast noted in the micrograph.

The shear planes of these dislocations were examined by stereo microscopy and found to lie on the (100) planes for those attached to the faults. The Burgers vectors were determined for some of the dislocations, which exhibited clear change in the contrasts by the visibility tests such as shown in Figures 6-7(a)~(f). The typical feature is that the intensity of the dislocation contrasts is much weaker than those observed at 300 K (Figure 6-1) and 673 K (Figure 6-4). Some of the dislocations were composed of partial dislocations lying on definite different planes from the (100) fault planes as confirmed by stereo microscopy in Figures 6-8(a) and (b). In view of the stress concentration and disturbance by the SiC, it is not surprising that the partials lie on the fault planes nearly vertical to the foil surfaces in the Figures 6-7(a)~(f). Operation of the partial dislocations eliminating the pre-existed faults seems to have contributed to the generation of perfect dislocations as suggested by the stereo microscopy shown in Figures 6-8(a) and (b). This is in contrast to the groups of perfect dislocations generated seemingly independent of the faults at lower temperatures 300 K and 473 K. The crystallographic information about the dislocation segments A~G in Figure 6-7 is given in Table 6-I. The morphology is complicated because some kinds of dislocation reactions were occurred.

6.4. Discussion

6.4.1. *The plasticity detected prior to crack by semi-in-situ experiments*

The semi-in-situ experiments provided evidence that the monoclinic $Al_{13}Fe_4$ is deformable by dislocation motion in the temperature range, 300 K ~ 873 K. In general, it is known that a large stress is needed to generate dislocations in the intermetallic compound by some means [7] [8]. Then, once dislocations are generated, they tend to sweep away the shear

planes spontaneously without involving interaction with other defects under the high uniform stress. Lack of ductility in this crystal may, thus, be attributed to the lack of work hardening against dislocation motion or even weakening along the shear planes due to shearing of the pre-existed obstacles at a high stress level. In order to observe dislocations remaining after deformation, therefore, the high stress needed to generate dislocations must be localized as in the present study, especially at low temperatures. Such an experiment was realized by placing a sandpaper as described in the preceding sections. The present semi-in-situ method is superior to other sophisticated techniques developed recently [3] in its simplicity.

At a higher temperature, say above 673 K, the dislocations introduced under a uniform stress became observable rather easily in the thin foil specimen, although the compression was given under a constraint on a thin foil specimen to avoid the spontaneous fracture. In the thin foil specimens, the dislocations introduced at one side of the specimen surfaces will bow out to the other side. Then, the dislocations penetrating from top to bottom of the surfaces will remain along the shear planes after deformation unless they move out of the foil from the periphery of the hole. The four dislocations observed as a set inside the white square area in Figures 6-4(b) and (c) are considered to be the dislocations capable of contributing to the macroscopic strain by operation a kind of the pole mechanism [9].

It is important to note that the stress concentration at the small SiC particles less than several μm can generate dislocations and at the same time the stress acting on the dislocations decreases rapidly as the dislocations leave the immediate vicinity of the particle site to stop the spontaneous motion. For the purpose of detecting the dislocations induced prior to the mode II crack, the present method is simple and useful. Moreover, it is fortunate that the paper burns at high temperatures leaving the SiC particles to induce deformation and at the same time the chemical reaction of the burning appears to have prevented growth of the oxides on the foil specimen to preserve it clean. Based on the various trials attempted to detect dislocations in the monoclinic $Al_{13}Fe_4$, it is found to play a key role to make observation directly without electro polishing. In such a study use of the HVEM is particularly advantageous in increasing the possibility of finding something new in a thicker specimen.

6.4.2. *The shear systems in the monoclinic $Al_{13}Fe_4$*

The lattice imperfections observed before and after the semi-in-situ deformation are summarized in Table 6-II. In order to visualize the crystal structure and the atomic arrangements in conjunction with the shear planes, shear directions and the Burgers vectors detected in the present study, the crystal structures viewed along the different crystal axes are shown in Figure 6-9. The three types of the shear systems are focused in these model crystals: In (a) and (b), the (110) shear planes are viewed edge on; likewise, in (c) and (d) the (001)

planes and in (e) and (f) the (310) planes, corresponding to the shear systems identified after deformation at 300 K, 673 K and 873 K respectively.

In general, dislocations are called either perfect (complete) or partial (incomplete) types depending on whether they are attached to faults or not. Focusing on the partial dislocations, the typical feature is that the fault planes in the as-annealed specimen were completely flat and the intersections with the foil surfaces were straight in the smoothly polished areas. The partial dislocations attached to these faults are judged to be the reaction products of the partial dislocations moved to release the thermal stress upon cooling. In order to be compatible with the thermal stress, which usually originates from the difference in the thermal expansion coefficients between the particles and the matrix, multiple shear systems must operate as found in Figure 5-2(d) and (e) lying on pentagonal planes (e). Furthermore, the dislocation contrasts in the as-annealed specimen (Figure 5-2) are weaker and finer compared to those introduced by plastic deformation (Figure 6-6). This facts indicate that some dislocation reaction such as Cottrell-Lomer locking [9] may have occurred upon cooling to release the elastic energy. The flattening of the faults as well as the weakening of the dislocation contrast may have been assisted by atomic diffusion in the complex ordered structure. In contrast to the fact that the internal stress caused by the difference in the thermal expansion generates glide dislocations in the usual ductile metals, the thermal stress might not be sufficient to generate perfect dislocations with a larger Burgers vector in the monoclinic $Al_{13}Fe_4$.

Focusing on the perfect dislocations, the shear systems operated at 300 K, 673 K and 873 K were identified as $[557](1\bar{1}0)$, $[110](001)$ and $[\bar{5}\ 15\ \bar{2}](310)$ as listed in Table 6-II. Considering the shear displacements governed by dislocation motion, it has been well known that the smaller the Burger vector is and the larger the plane spacing is the stress required for the glide motion is lower by a factor proportional to ~exp(-h/b) where b is the magnitude of the Burgers vector and h is the shear plane spacing [10]. In good accordance with this recognition, the shear planes are confirmed to be well separated when they are viewed edge on as shown in Figure 6-9. The Burgers vectors were identified to be directed along the [557], [110] and $[\bar{5}\ 15\ \bar{2}]$. In the case of [110] type observed after deformation at 673 K, the Burgers vector is hypothesized to be [110]/2 with its magnitude of 0.87 nm in accordance with the suggestion given in the earlier report for quasicrystal approximant [5] [6]. According to the results of the Burgers vector analyses (Table 6-II) and the crystal structure viewed perpendicular to the Burgers vectors in Figure 6-9.

As a matter of fact, the intensity of the images, which vary with the magnitude of the Burgers vector, can be judged rather easily without making calculation as far as the direction is known, since the intensity represents the integrated property of the strain field around the dislocation [11]. In another words, the intensity varies approximately proportional to b^2 while b

is proportional to the discrete multiple of the atomic distance. Once the Burgers vector direction is determined, therefore, it is an easy task to select the most likely magnitude from the image intensity on the bases of the model crystals viewed along special direction such as shown in Figure 6-9. That is, the image intensity of a dislocation varies drastically depending on the crystal structure, namely depending on the magnitude of the Burgers vector. Although it is usual procedure to control the **s** vector so as to make the dislocation contrast sharp, difference in the contrast can still be recognized easily by comparing the images with knowledge of the **s** vectors known easily from the Kikuchi-lines. For example, comparison of the dislocations in FeAl of B2 [12], Ni_3Ge of $L1_2$ [13], Al_3Ni of $D0_{20}$ [14] and Al_3Ti of $D0_{22}$ [15] may be helpful in this regards.

Another point to be cautioned in examining the dislocation images in the ordered compound of a large unit cell is the overlapped images coming from the nearly spaced diffraction spots. In this study such spots were avoided to contribute to the imaging by trials and errors. However, some question remained about identification of the dislocation images. Further study is needed to make complete correspondence between the images and the diffraction condition which requires computer simulation, although it is beyond the scope of the present study.

6.4.3. *Temperature dependence and atomic diffusion*

Another point is the introduction of the perfect dislocations at lower temperatures in contrast to the partials with the smaller Burgers vectors contributed to the deformation or generation of perfect dislocations at 873 K. The partials are always attached to planar faults but in deferent manner presumably depending on the contribution of the stress and atomic diffusion at different temperatures. It may be hypothesized that the partial dislocation motion involving elimination of the planar faults (Figure 6-7 and 6-8) becomes possible owing to the reduction in the energy, the process of which is likely assisted by atomic diffusion at a higher temperature. The dislocation motion leaving such faults is similar to those observed in quasicrystals [16]. Otherwise, generation of the perfect dislocations and their conservative motion in the complex monoclinic crystal must require extremely large stress. Once such dislocations are generated, their motion must be spontaneous under a uniform stress as pointed out in chapter 5. Preservation of the perfect dislocations in the hardly deformable materials such as in the present $Al_{13}Fe_4$, thus, requires special condition in the stress concentration as observed in the present study. Nevertheless, it is gratifying to know that the plastic deformation takes place by dislocation motion prior to the mode II cracking even at 300 K.

6.5. Conclusions

The monoclinic $Al_{13}Fe_4$ embedded in Al matrix was examined at different temperatures in the range 300 K ~ 873 K by means of the semi-in-situ compression of a thin foil specimen. Two types of experiments were made to protect the specimen from cracking: One was to give compressive stress on a thin foil specimen by placing deformable metal foils and the other was to put a sandpaper on the foil specimen to induce dislocations by stress concentration and yet to protect the dislocations move out of the specimen spontaneously. The HVEM observations made at 1000 kV have revealed the following characteristic properties depending on the test temperature.

1) The size of the plastic zone increased rapidly with increase in the test temperature under a uniform stress.
2) Dislocations contributed to the plastic deformation were identified after deformation both at 300 K and 873 K by use of a sandpaper.
3) The stress applied rather uniformly over the considerably larger region exceeding the size of the foil thickness induced dislocations in discrete manner at 673 K and 873 K.
4) The Burgers vector directions and the shear planes activated at 300 K, 673 K and 873 K were identified as [557]$(1\bar{1}0)$, [110](001) and $[\bar{5}\ 15\ \bar{2}]$ (310), respectively.
5) The $[\bar{5}\ 15\ \bar{2}]$ (310) type of dislocations were judged to be formed by a dislocation reaction involving atomic diffusion among the partial dislocations, whereas the [557]$(1\bar{1}0)$ and the [110](001) types of dislocations were judged to be generated directly at foil surfaces under the high stress.

References

[1] S. Takeuchi and T. Hashimoto, Jpn. J. Appl. Phys. **32** 2063 (1993).

[2] M. Wollgarten, M. Bartsch, U. Messerschmidt, M. Feuerbacher, R. Rosenfeld, M. Beyss and K. Urban, Phil. Mag. Lett. **71** 99 (1995).

[3] M. Wollgarten, H. Saka, and A. Inoue, Phil. Mag. **A 79** 2195 (1999).

[4] P. J. Black, Acta Crystallogr. **8** 43, 175 (1955).

[5] K. Saitoh and M. Tanaka, J. Alloys Comp. **342** 130 (2002).

[6] M. Feuerbacher, M. Heggen and K. Urban, Mater. Sci. Eng. **A 375-377** 84 (2004).

[7] N. Yoneyama, S. Kumai, A. Sato, M. Komatsu and M. Kiritani, Rad. Eff. & Defects in Solids **157** 109 (2002).

[8] N. Yoneyama, K. Setoda, S. Kumai, A. Sato, M. Komatsu and M. Kiritani, Mat. Sci. Eng. **A 350** 125 (2003).

[9] J. Weertman and J. R. Weertman, Elementary Dislocation Theory: (Macmillan Co., New York, 1964).

[10] F. R. N. Nabbaro: Theory of Crystal Dislocations (Oxford Univ. Press, 1967).

[11] P. B. Hirsch, A. Howie, R. B. Nicholson, D. W. Pashley, and M. J. Whelan, Electron Microscopy of Thin Crystals (Butterworth & Co. Ltd., London, 1971) p. 247.

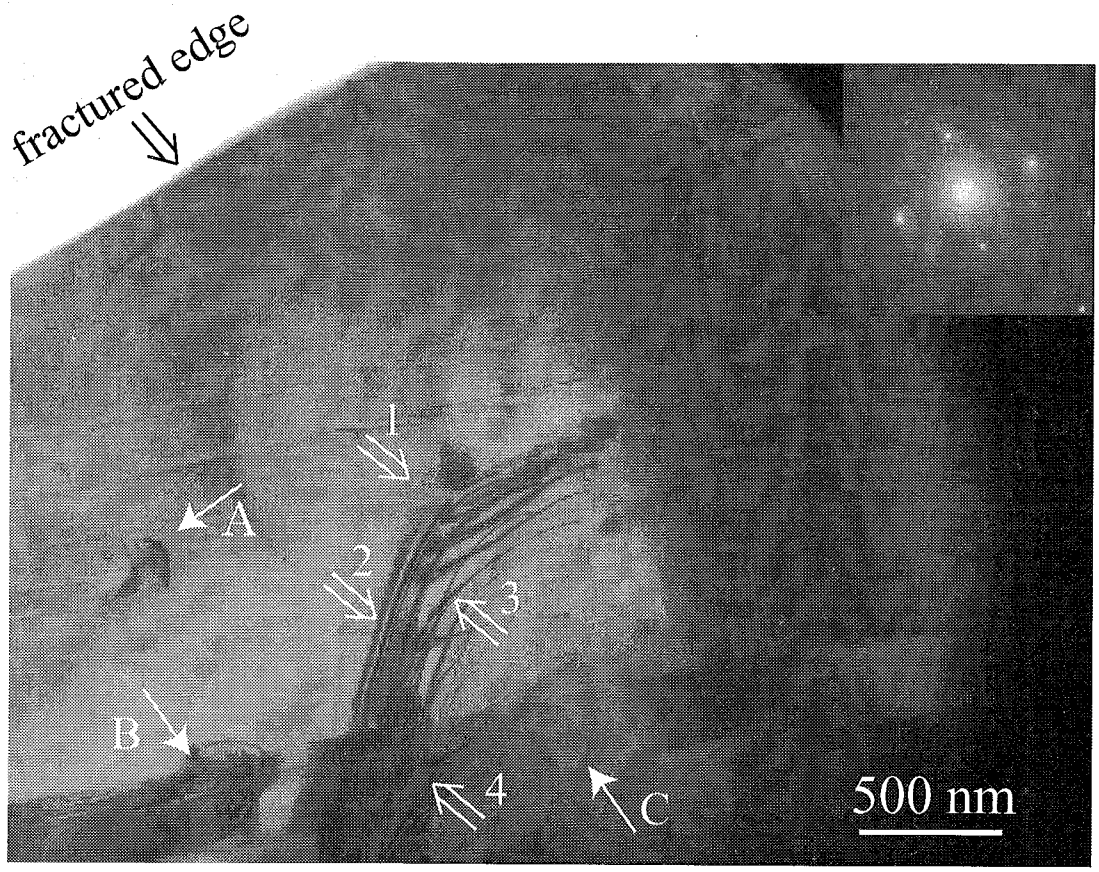
[12] K. Yamashita, M. Imai, M. Matsuno and A. Sato, Phil. Mag. **A 78** 285 (1998).

[13] T. Murakumo, K. Haruta, N. Yoneyama and A. Sato, J. Microsc. **203** 57 (2001).

[14] K. Yamashita, I. Fujimoto, T. Murakumo, S. Kumai and A. Sato, Phil. Mag. **A 80** 219 (2000).

[15] K. Yamashita, I. Fujimoto, S. Kumai and A. Sato, Mater. Trans. JIM **39** 824 (1998).

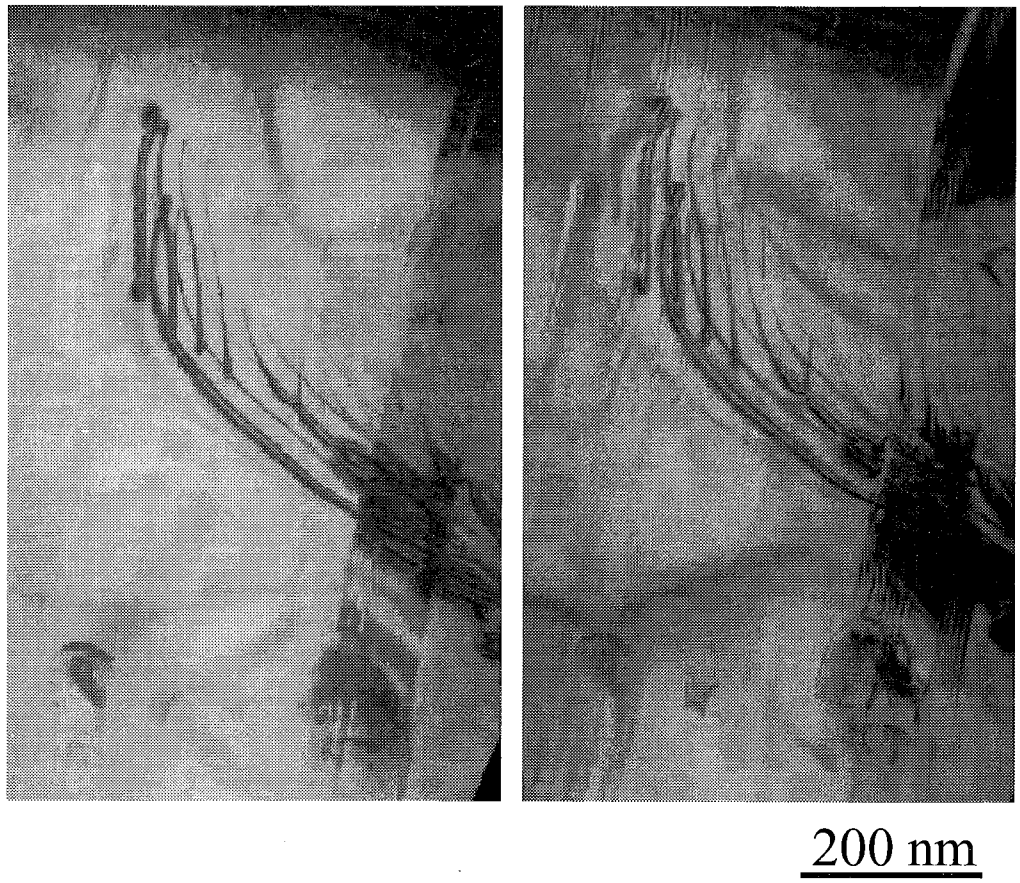
[16] F. Mompiou and D. Cailard, Mat. Sci. Eng. **A 400-401** 283 (2005).



(a)

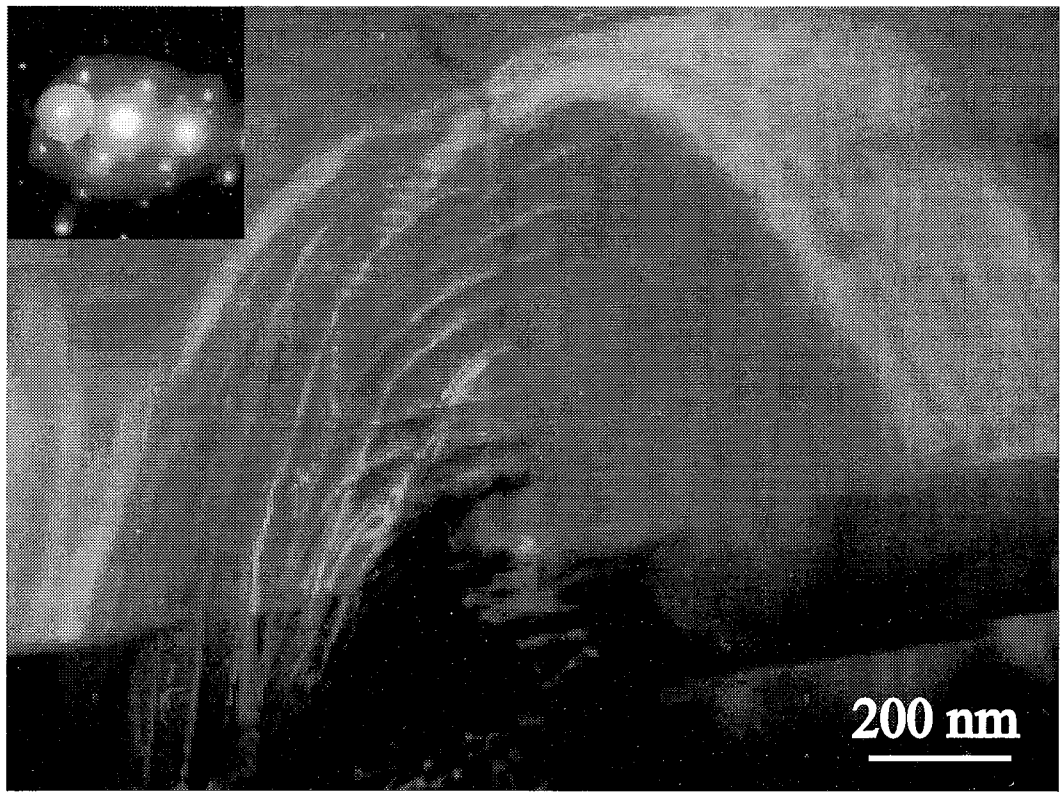
Figure 6-1

Groups of dislocations introduced at 300 K in the immediate vicinity of the Al_2O_3 particles by using a sandpaper in the semi-in-situ deformation. The numbers 1, 2, 3, and 4 in (a) identify the four groups of dislocations examined under various diffraction conditions in (a) ~ (d). (b) shows a stereo pair of micrographs. (c) A dark field micrograph taken by a diffraction spot marked in inset. (d) The groups of dislocations 1 ~ 4 are viewed along the slip planes aligned edge on with the indices of diffraction patterns to identify the slip plane.



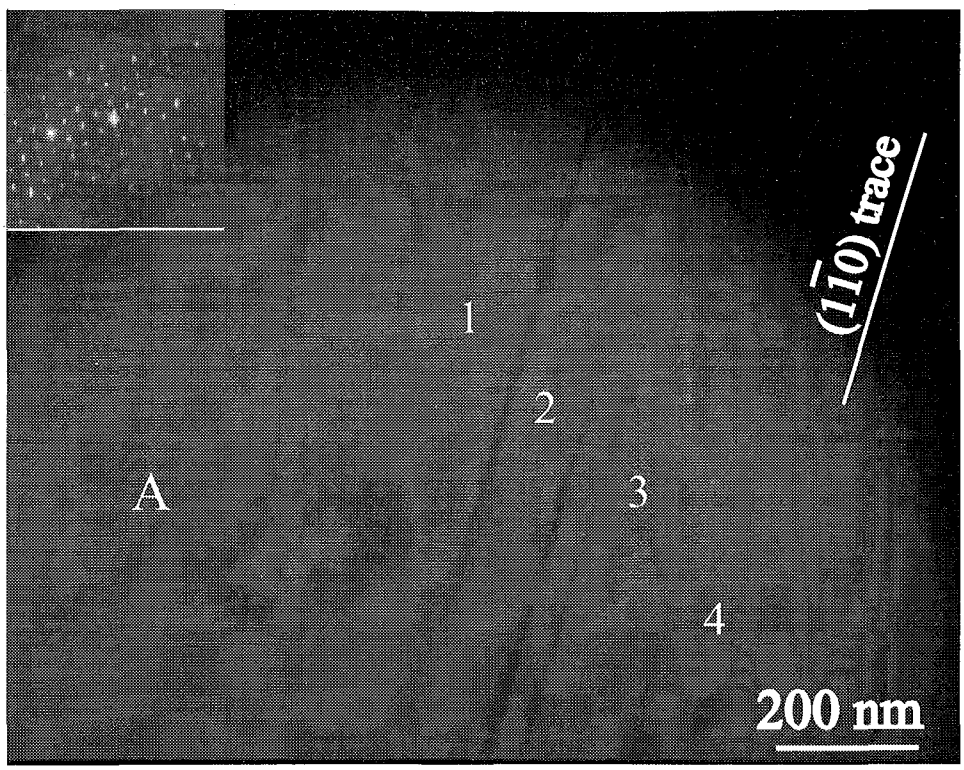
(b)

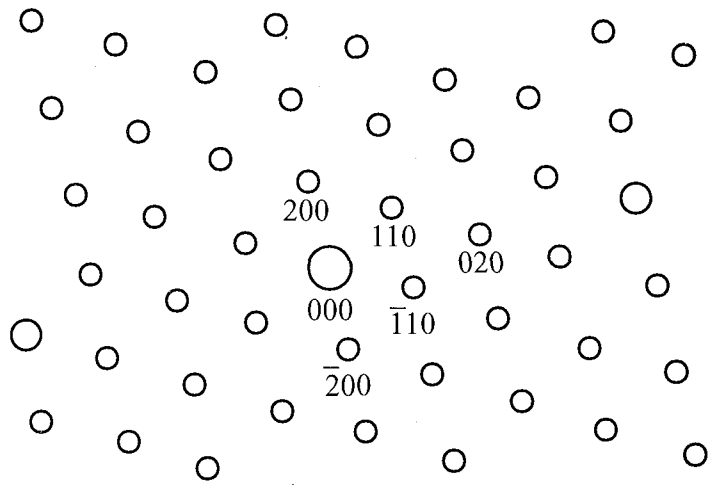
Figure 6-1



(c)

Figure 6-1





Beam Direction: [00$\bar{1}$]

(d)

Figure 6-1

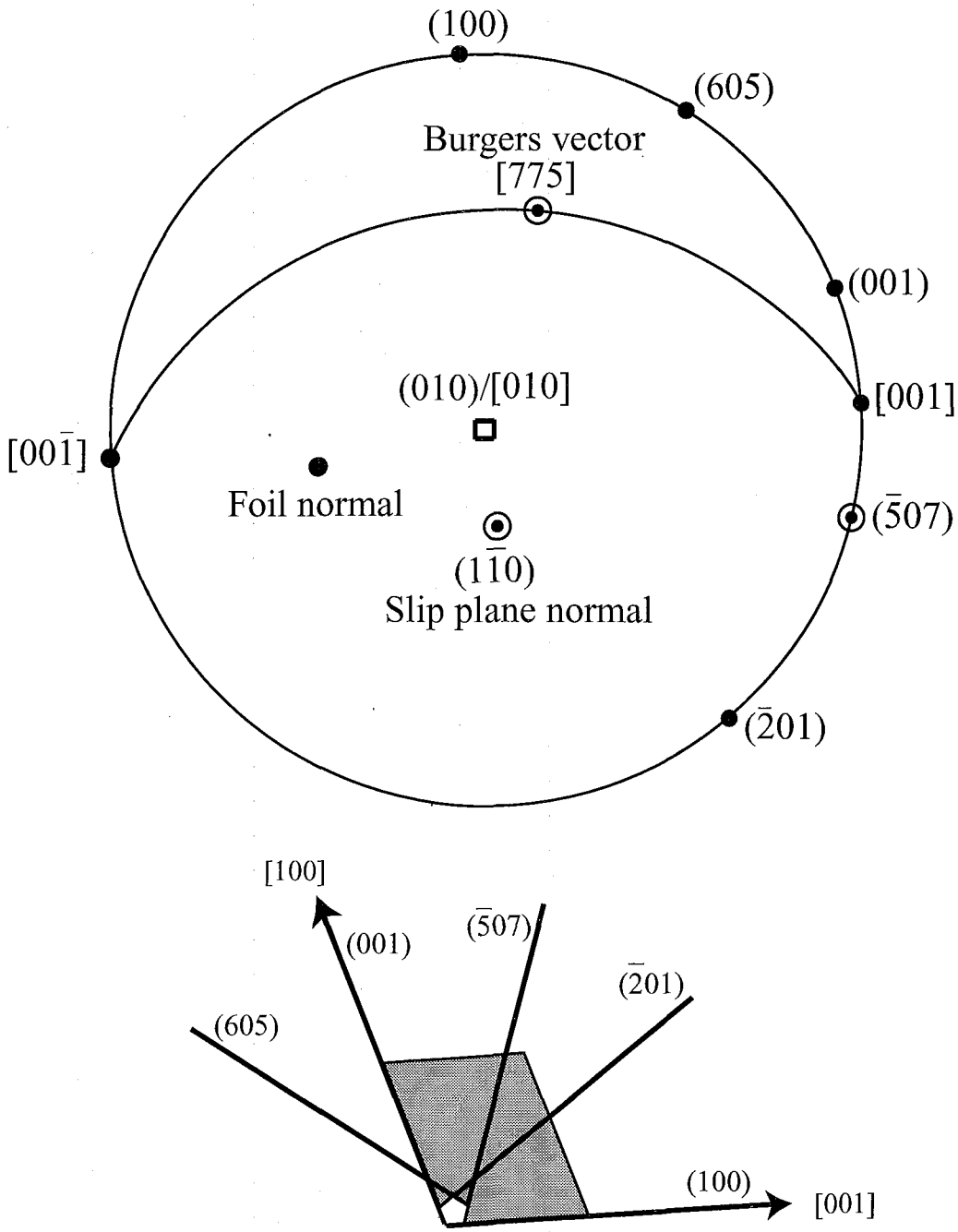
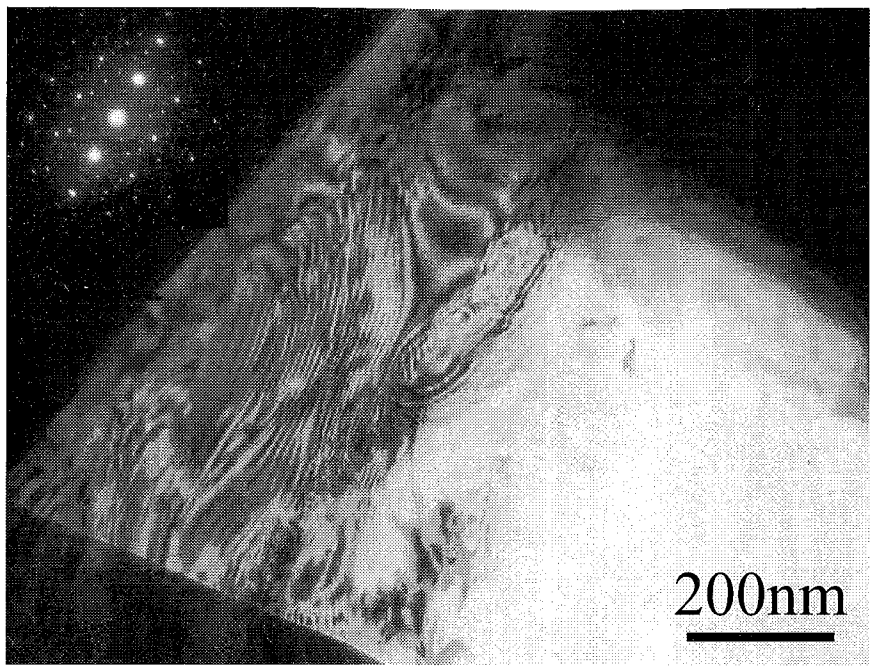
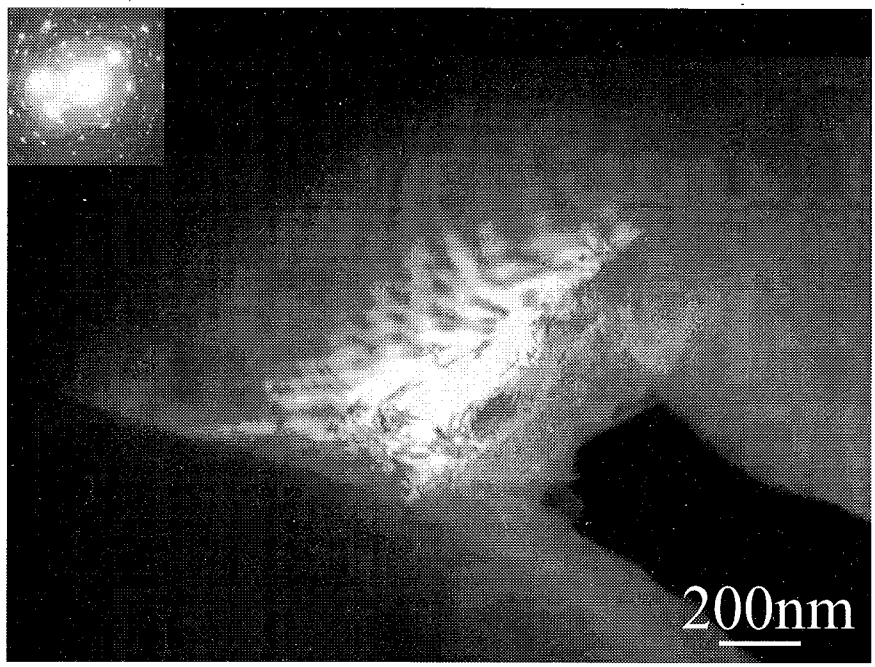


Figure 6-2

Stereographic projection showing the specimen geometry of the observation in Figure 6-1 with additional information of the invisibility of the dislocations for **g**=$\bar{5}$07. The Burgers vector, perpendicular to the plane normal ($1\bar{1}$0) and ($\bar{5}$07) was determined as [775].



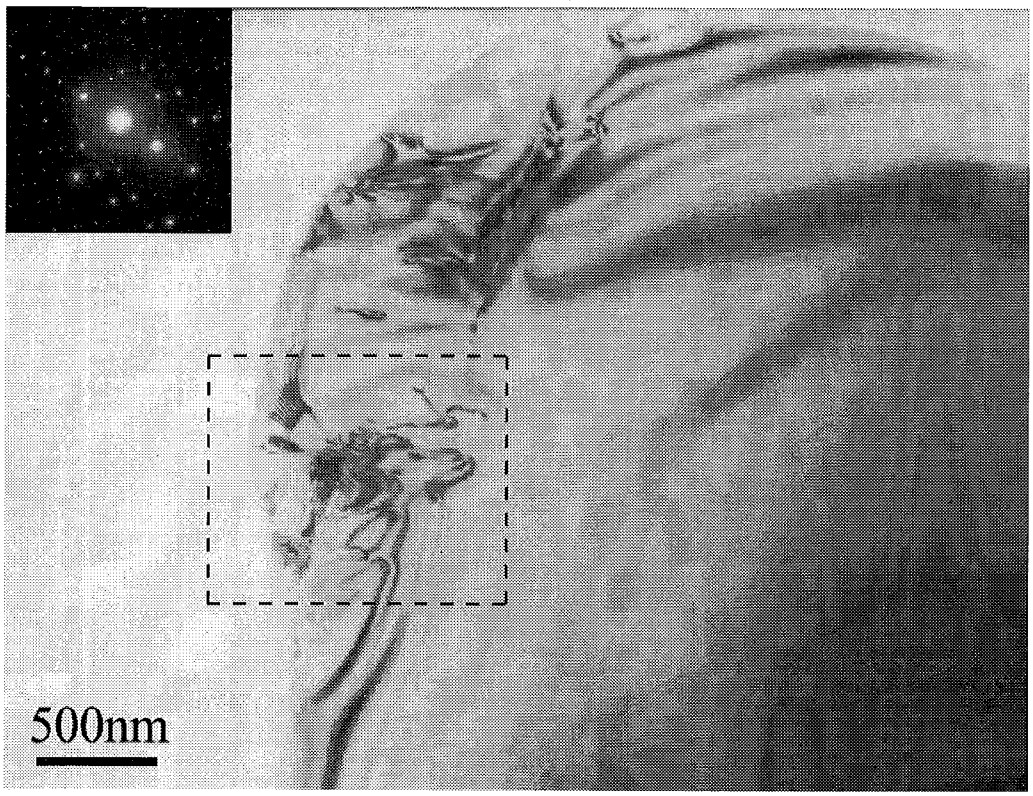
(a)



(b)

Figure 6-3

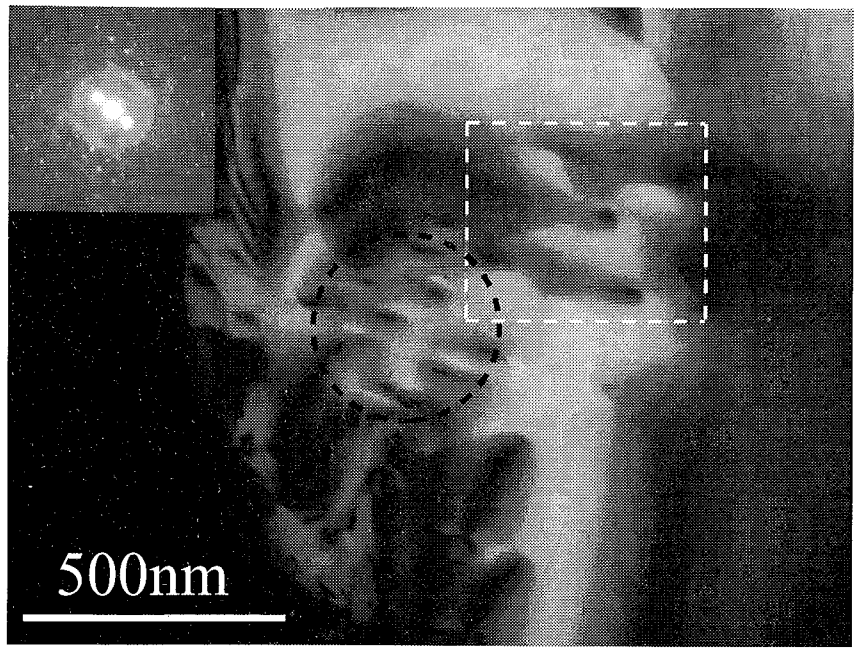
Defect structures observed along the sheared off planes after deformation at 473 K. Evolution of complicated fringes in (a) are quite similar the Figure 5-6 and dislocation clusters were observed under a suitable diffraction condition in (b).



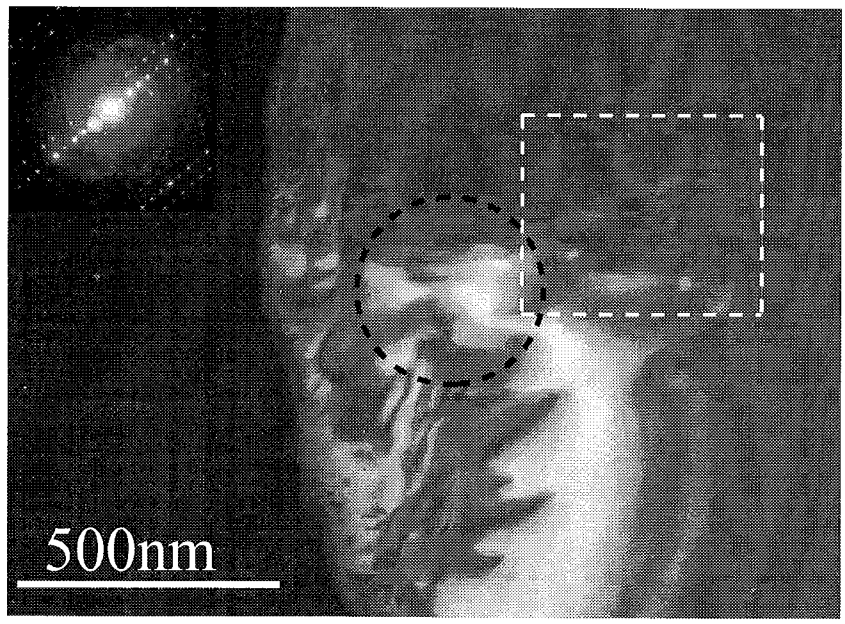
(a)

Figure 6-4

Dislocations introduced at 673 K by nearly uniform compression of 74 GPa. The clean and smooth periphery was squeezed to preserve dislocations and the area bound by a square mark was examined under different diffraction conditions by dark field imaging in (b) and (c). The dislocations observed in a circle in (b) are invisible in (c) for $\mathbf{g}=\bar{1}\bar{1}0$. Note that a group of dislocations with an windmill structure are composed of 4 dislocations.



(b)



(c)

Figure 6-4

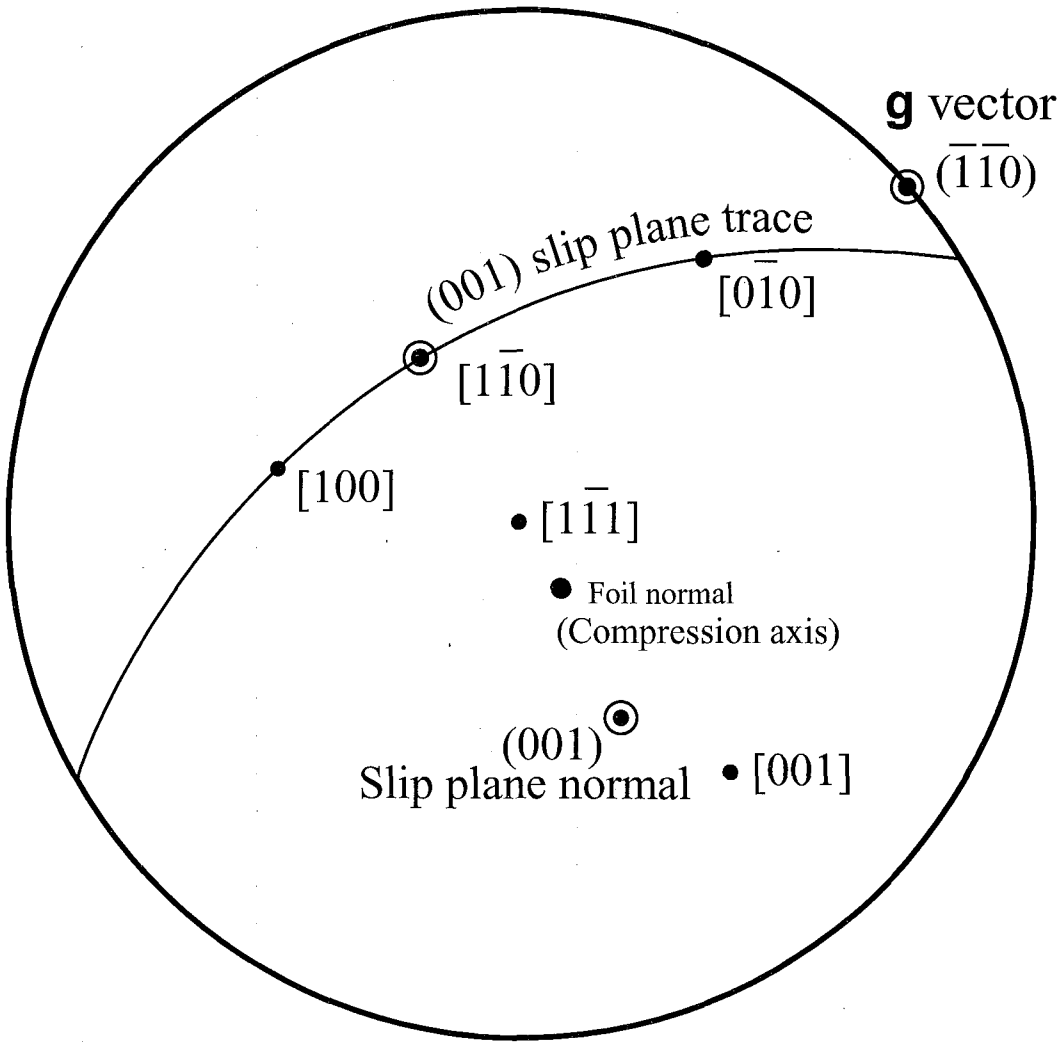
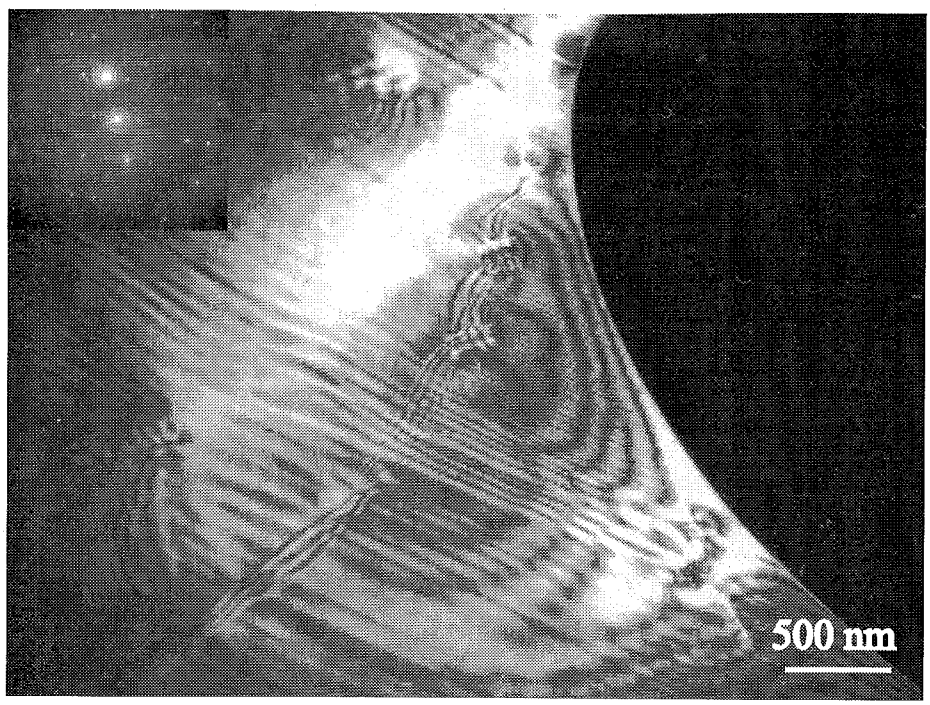
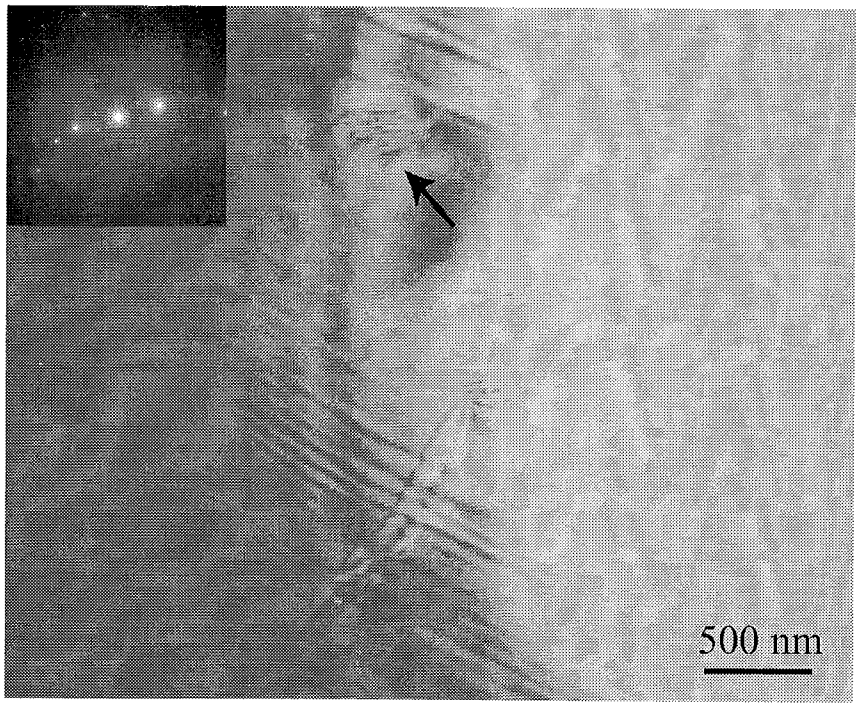


Figure 6-5

The stereographic projection showing the specimen geometry for the observation in Figure 6-4. The Burgers vector was determined from the information of the slip plane and the invisibility for **g**=$\bar{1}\bar{1}0$



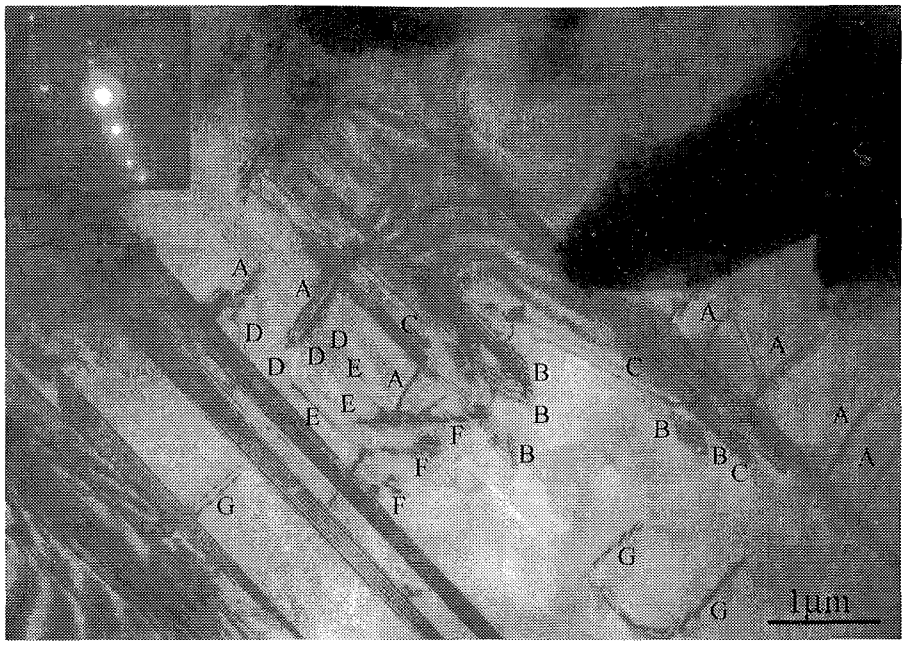
(a)



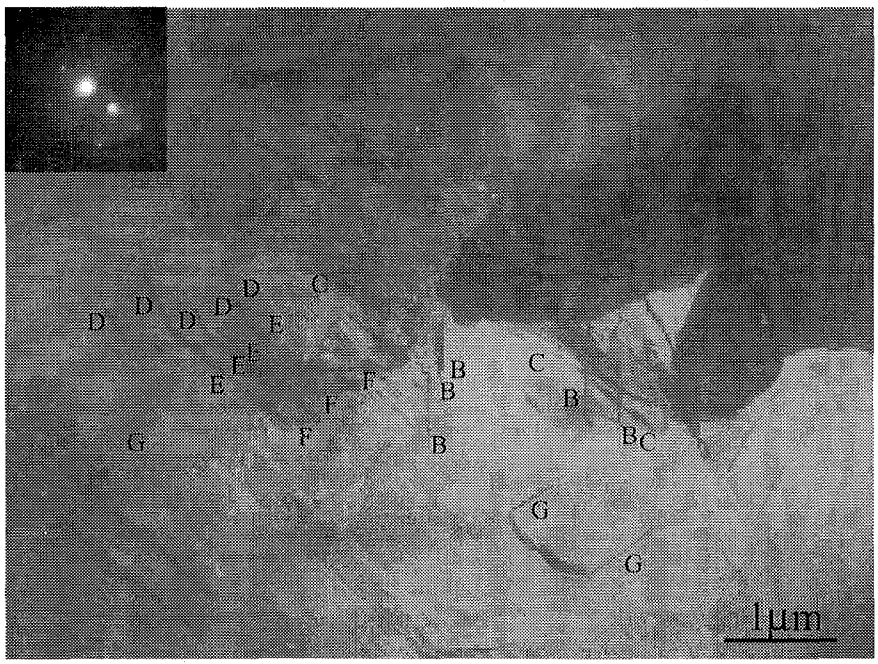
(b)

Figure 6-6

Partial dislocations observed in the electro polished specimen after the nearly uniform deformation of a foil made at 873 K. Note that the faults contributed the deformation are curved gradually in (a) and partial dislocations are resolved to be composed to be of multiple dislocations in (b).



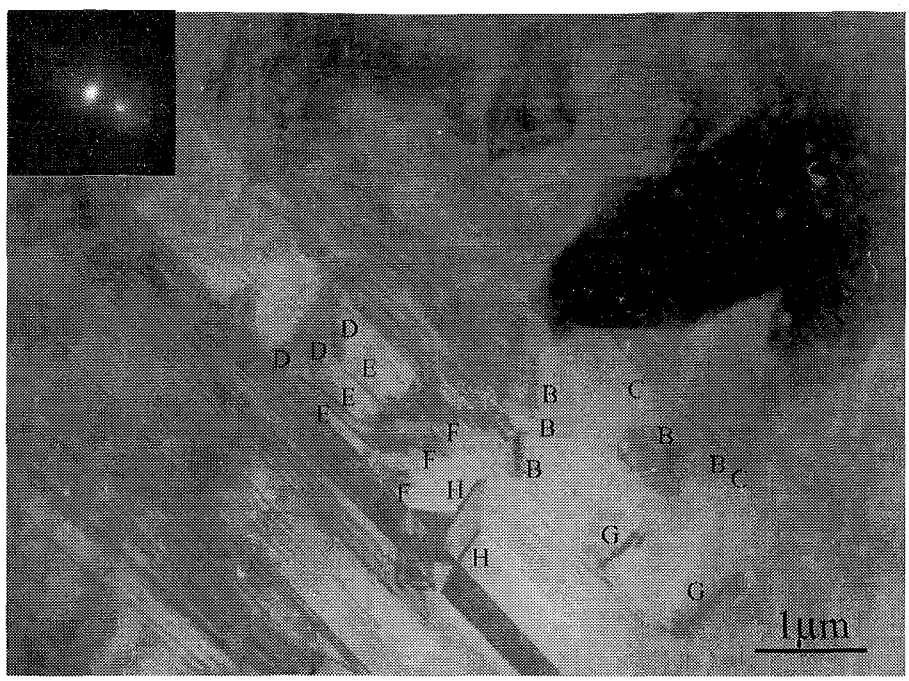
(a)



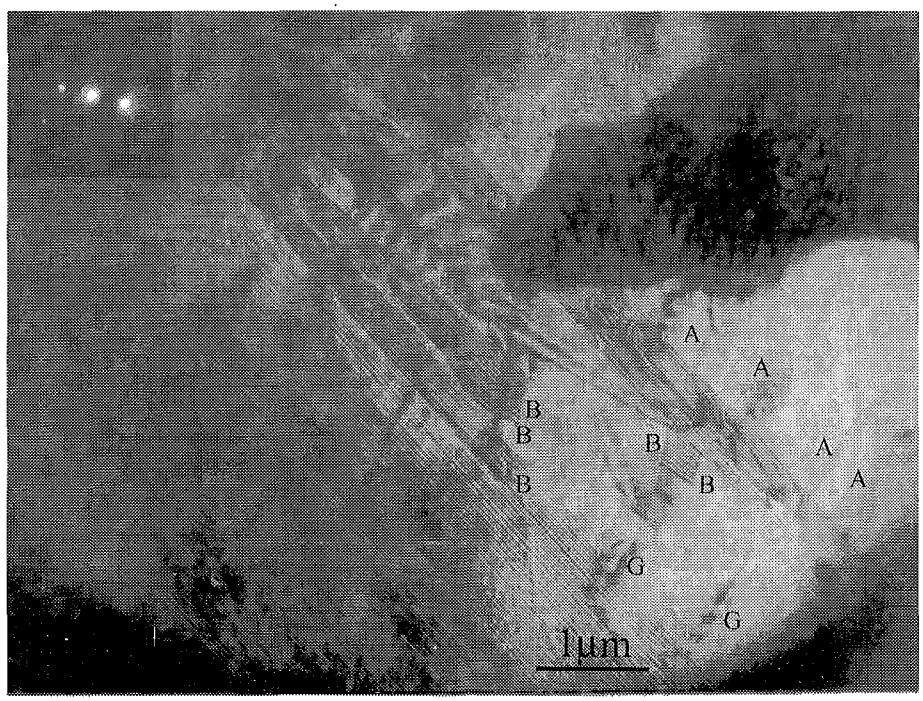
(b)

Figure 6-7

Dislocations introduced near the Al_2O_3 particle examined under various diffraction conditions in (a) ~ (f). The individual dislocation segments are identified by the alphabet in every photographs. The geometrical information of the each group of dislocations is given in Table 6-I.

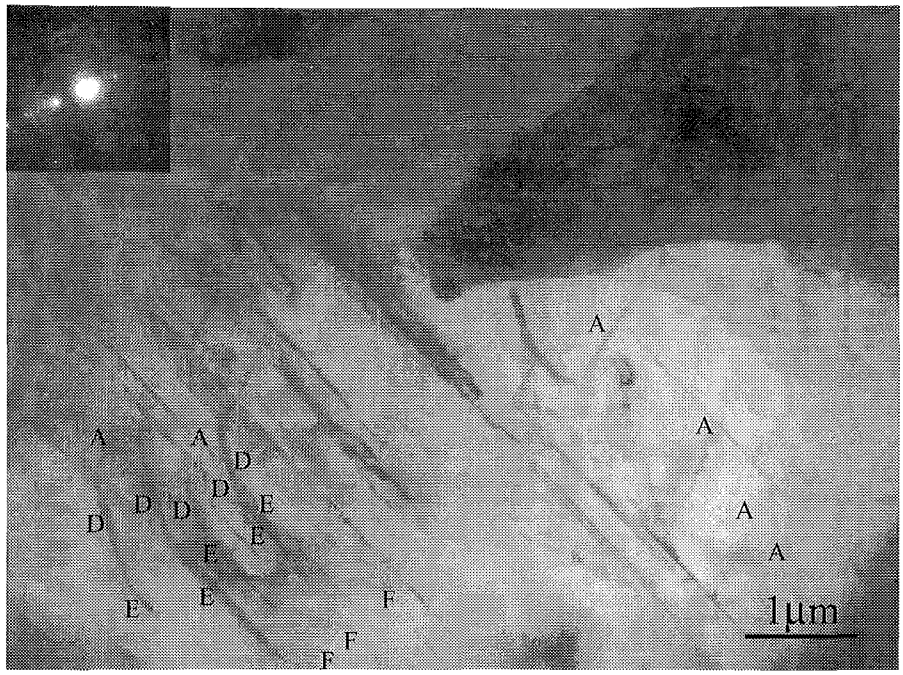


(c)

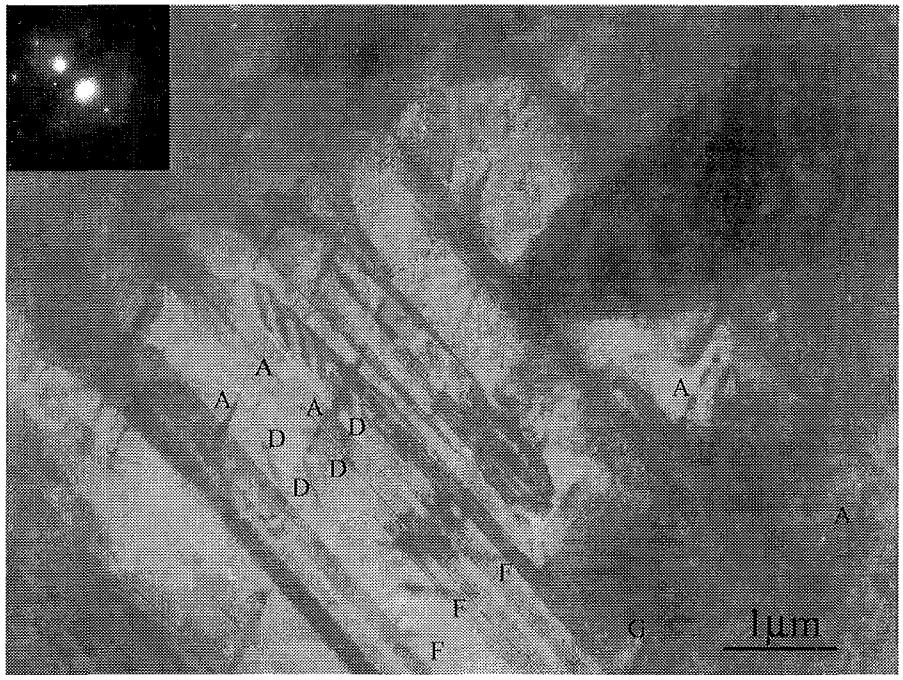


(d)

Figure 6-7

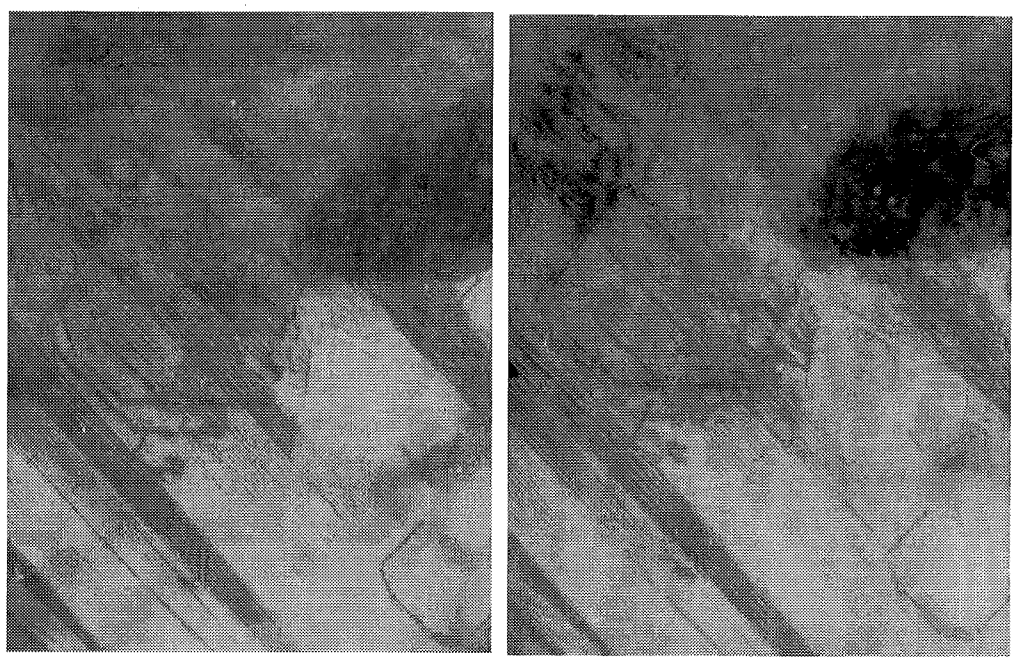


(e)



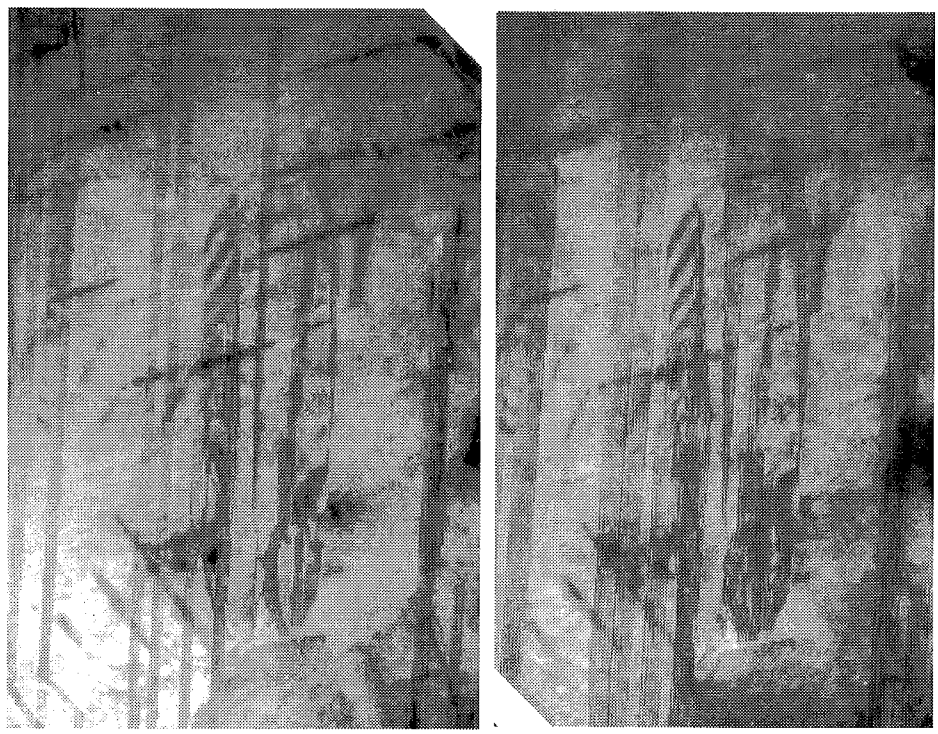
(f)

Figure 6-7



(a)

Figure 6-8
(a) and (b) are stereo pairs of a middle area in Figure 6-7. Pre-existed faults have been eliminated by movement of partial dislocations. Some perfect dislocations tend to be emitted from those areas.



(b)

Figure 6-8

Table 6-I

The morphology and shear planes of the dislocations (A ~ G) examined in Figure 6-7.

	A	B	C	D	E	F	G
shear plane	—	(100)	(100)	(310)	(310)	(310)	—
direction of straight dislocation	nearly along [110]	[010]	curved	segmented	segmented	segmented	[110]
comments	slightly off from a unique shear plane	terminated at planner fault	observed at periphery of a planner fault	D, E, and F segments are connected at corners to compose a bowed out configuration			connected in similar manner as D, E and F

Table 6-II

Lattice defects and slip systems observed at various temperatures. The validity of the slip systems will be examined with adequately designed atomic models of the monoclinic $Al_{13}Fe_4$.

	as-annealed	deformed at 300 K	deformed at 673 K	deformed at 873 K
stress condition	thermal stress	concentrated at Al_2O_3 particles (4 GPa)	nearly uniform (74 GPa)	concentrated at Al_2O_3 particles (400 MPa)
lattice defects and slip system	• thick twin plates • zigzag shaped stacking faults • partial dislocations with small |**b**|	• perfect dislocations were introduced • slip system [557] $(1\bar{1}0)$	• perfect dislocations were introduced • slip system [110] (001)	• partial dislocations combined to generate parfect dislocations • slip system $[\bar{5}\ 15\ \bar{2}]$ (310)

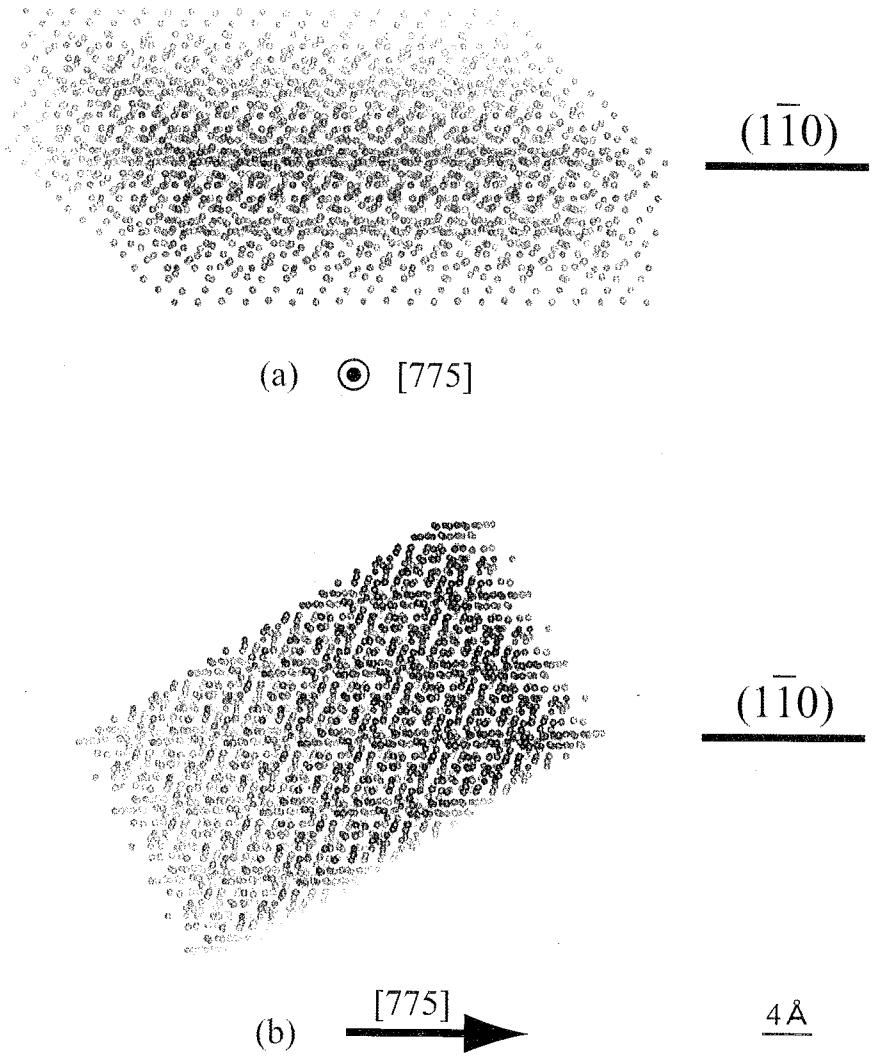
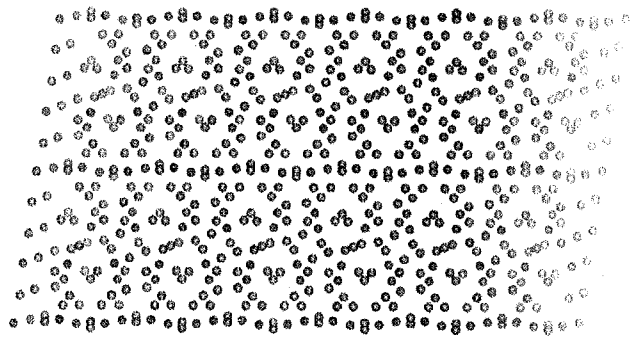


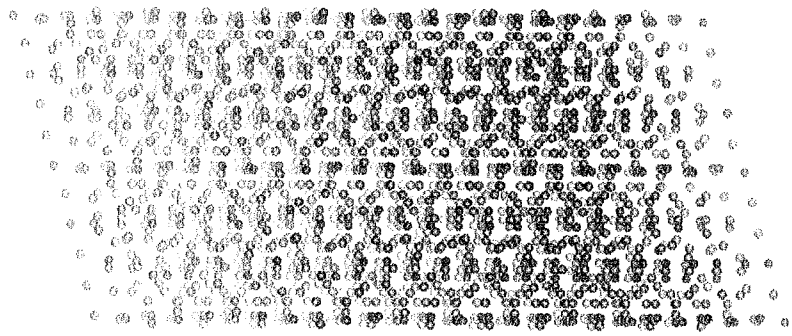
Figure 6-9

Three dimensional information for the two examples of the shear systems determined in the present study. A model $Al_{13}Fe_4$ lattice is viewed along the Burgers vector direction of [557] in (a) and perpendicular to the Burgers vector in (b) corresponding to the deformation at 300 K. The same lattice is viewed along the Burgers vector direction of [1 1 0] in (c) and perpendicular to the Burgers vector in (d) corresponding to the deformation at 673 K, and viewed along the Burgers vector direction of [$\bar{5}$ 15 $\bar{2}$] in (e) perpendicular to the Burgersvector in (f) corresponding to the deformation at 873 K.



(001)

(c) ◉ [110]

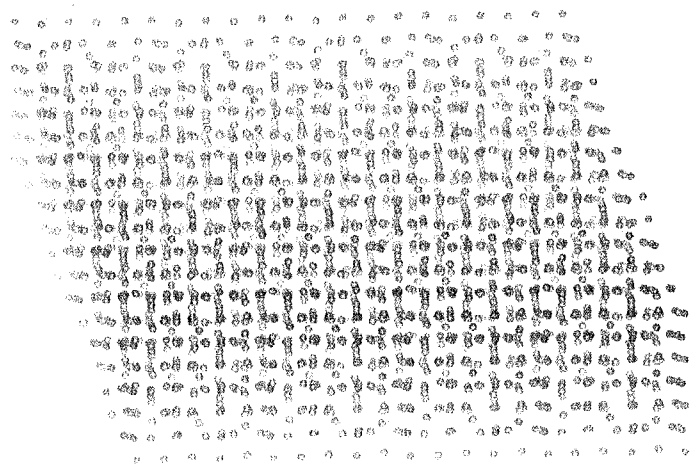


(001)

4 Å

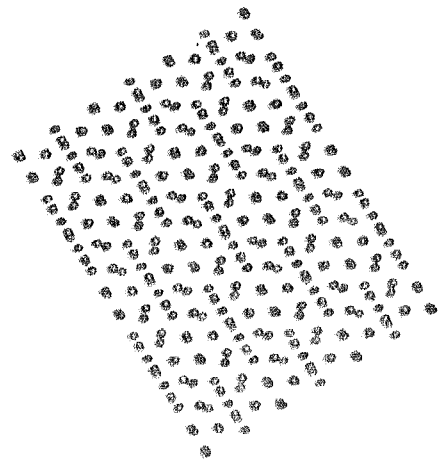
(d) [110]

Figure 6-9



(310)

(e) ⊙ [$\bar{5}$ 15 $\bar{2}$]



(310)

(f) [$\bar{5}$ 15 $\bar{2}$] → ⊙ [001]

4Å

Figure 6-9

Chapter 7

Plasticity of $Al_{65}Cu_{20}Fe_{15}$ Quasicrystals Embedded in Al_2Cu

7.1. Introduction

Plastic deformation of a quasicrystal with fivefold symmetry axes [1] is known to accompany so-called "phason-strain" in addition to usual strain observed in three dimensional space [2]. Therefore, in order to release the phason-strain, dislocation motion has been examined at high temperatures [3] [4] [5] and their motion has been confirmed directly by in-situ experiments conducted at a high temperature [6]. It has also been suggested that a force necessary to move a dislocation increases with decreasing deformation temperature [7] [8]. Burgers vectors in a quasicrystal of icosahedron are denoted by using 6 basic vectors composed of $\tau=(1+5^{1/2})/2$ and unit vectors in real space [9]. Several researchers have reported the Burger vector analysis [10] [11]. The possible directions are considered to be two-, three- or fivefold axes.

Takeuchi and Hashimoto have observed dislocations accompanying planer faults under an indentation mark [12]. One of the purposes here is to determine the Burgers vector of the dislocations introduced by deformation at a room temperature in a quasicrystal of $Al_{65}Cu_{20}Fe_{15}$ embedded in Al_2Cu matrix. In this chapter deformation tests are made at intermediate temperatures, 650K and 550K, in bulk and at room temperature in thin foil. The semi-in-situ method is applied to a thin foil specimen of quasicrystals. As mentioned in chapter 2, it is achieved by using a common double tilting specimen holder without polishing after compression and is a primitive but powerful way to examine the hardly deformable quasicrystal under a large stress.

7.2. Experimental Procedures

A composite alloy of Al_2Cu/ $Al_{65}Cu_{20}Fe_{15}$ was prepared by arc-melting the elements of Al, Cu and Fe with the purity better than 99.9 %. According to a phase diagram reported by Tsai [13], Al-29.1at%Cu-3.3at%Fe was chosen so that small quasicrystals of $Al_{65}Cu_{20}Fe_{15}$ are introduced and bound by Al_2Cu of a body centered tetragonal structure.

Compression tests were made at 650K and 650K→550K in bulk. Al_2Cu matrix shows sufficient ductility in this temperature region [14]. Specimens with the dimension $2.5\times 2.5\times 3.5$ mm^3 were cut and polished mechanically. The specimens were compressed in an Ar

atmosphere with an Instron-type testing machine at a crosshead speed of 0.05mm/min ($\varepsilon = 2.4\times10^{-4}s^{-1}$). Thin foils were prepared from the deformed specimens.

Since Al_2Cu shows no ductility at room temperature, deformation of the quasicrystals embedded in Al_2Cu could not be examined by usual tensile or compression tests made in bulk. Pre-strain was given to the composite at a higher temperature to increase deformability of the material by introducing mobile dislocations [15]. In addition, thin foils observable by TEM were prepared from the pre-strained specimens, deformed by a Vickers indenter as shown in Figure 2-1 and examined directly by a transmission electron microscope (TEM).

Specimens were thinned down to 100 μm mechanically and then jet polished from one side of the surfaces, so that they can be set flat on a polished smooth platform made of ZrO_2 as shown in Figure 2-1. Electrical polishing to perforation was made in a cooled mixture of perchloric acid and methyl alcohol at 213 K.

Since thinning speed was slightly faster for quasicrystal than for Al_2Cu matrix, the quasicrystals of observable thickness were distributed in wide area and surrounded by somewhat thicker Al_2Cu matrix. Therefore compression by a Vickers indenter through a steel foil (Fig. 2-1) was especially useful in stressing a small quasicrystal at a pin point.

The foils deformed as mentioned above were examined directly without electro polishing by JEM-2010 and H-1250S equipped with a double tilt specimen holder capable of tilting by 50°. In order to avoid formation of secondary defects by electron irradiation, observation was made at a relatively low magnification x10,000. For Burgers vector determination, a small objective aperture was used in dark field microscopy so that closely spaced diffraction spots can be differentiated in a quasicrystal.

7.3. Experimental Results and Discussions

7.3.1. *Non-deformed Quasicrystal*

Figure 7-1 shows quasicrystals embedded in Al_2Cu before deformation. Electrically polished specimen surface is shown in (a). Quasicrystal particles of a few micrometers are distributed forming trees with leaves of $Al_{65}Cu_{20}Fe_{15}$ particles embedded in Al_2Cu matrix. Some of the trees viewed nearly along the trunk appear as a set of flower petals in (a). A quasicrystal with flower petal like structure was, further, examined in (b) by HVEM. It is viewed along the direction of a fivefold symmetry at a low magnification. Since the foil plane is inclined with respect to the beam direction, petals cut by the foil surfaces do not show the five-fold symmetry. The selected area diffraction from one of the petals is also shown in (b). The uniform darkness of the image in (b) demonstrates the fact that orientation of the quasicrystal is same for all of the petals. The micrograph (c) shows dislocation distribution in

a quasicrystal particle. These dislocations were introduced during solidification locally to form complicated tangles.

A representative structure in Al_2Cu matrix surrounding an $Al_{65}Cu_{20}Fe_{15}$ quasicrystal is shown in Figure 7-2. Matrix has a group of dislocations along a small angle boundary, and has no dislocations inside the sub-grains. It will be shown below that a large number of dislocations are introduced homogeneously by bulk deformation at 650K to make the Al_2Cu reasonably ductile even at lower temperatures 550K and room temperature.

7.3.2. *Deformation at 650K and 550K*

Figure 7-3 shows microstructure of a composite specimen $Al_2Cu/Al_{65}Cu_{20}Fe_{15}$ deformed to several percent at 650K. A large number of dislocations were introduced homogeneously in Al_2Cu matrix as shown in (a). Stereoscopic observations have revealed that each dislocation line takes a complicated three-dimensional shape. It is obvious from the curved structure that atomic diffusion has assisted the dislocation motion in the Al_2Cu with a body-centred tetragonal structure at 650K. An example of a deformed $Al_{65}Cu_{20}Fe_{15}$ quasicrystal is shown in (b). Dislocations were introduced preferentially at roots of petal arms. Stress concentration at the roots induced local deformation in the particle and the total deformation was accomplished mainly by accommodation strain of ductile Al_2Cu matrix.

Deformation at 550K was made after pre-strain at 650K. Introduction of plenty of mobile dislocations in Al_2Cu enabled the composite specimen to deform without cracking. Figure 7-4 shows a microstructure of a quasicrystal after the additional deformation by a few percent at 550K. The Bragg condition is not uniform and its contrast varied in the interval of several hundreds of nm within a quasicrystal as shown in (a). A large number of dislocation tangles were created implying that dislocations moved individually in the same manner each other in a domain under a proper Bragg condition as shown in (a). Several planar faults pointed by arrows were also observed in this area. Bright field images of (b) and (c) were taken from the other $Al_{65}Cu_{20}Fe_{15}$ particle under different diffraction condition in the same area. Whereas (b) shows clear contrast of planar defect and several dislocations forming a deformation band, (c) shows no contrast of planar defect. This phenomenon was reported in high temperature deformation of an $Al_{70}Pd_{20}Mn_{10}$ icosahedral quasicrystal [16]. A long straight-line contrast pointed by an arrow in both (b) and (c) was examined by using of a convergent beam electron diffraction (CBED) method.

The line contrast in Figure 7-5 (a) is the same one shown in Figure 7-4 (b) and (c) and divided into 5 regions as marked by A-E. CBED patterns were taken at the 5 positions using a convergent beam of 50nm in diameter depicted by a solid circle with an arrow. When the circle is located in the area free from defects, a CBED pattern shows pairs straight lines

composed of bright and dark fringes as shown in the first picture in (b). Each pair of fringes appears in a defocused circle corresponding to a $g_{\|}$. When a dislocation line having a Burgers vector $b_{\|}$ across a pair of fringes, they twist to increase the number of fringes by $| g_{\|} \cdot b_{\|}|=n$. Direction of the twist is determined from its sign. Dislocations at A and D showed the same type of twists implying that these dislocations have the same Burgers vector components. It seems natural since they both lie on a deformation band. Dislocations at B and C show exactly opposite type of twists compared to A and D. Thus, majority of the dislocations in quasicrystal have remained as reaction products, making it difficult to determine the Burgers vector of an isolated dislocation. Further examination is needed to find proper dislocations in future study.

7.3.3. *Room temperature deformation*

Room temperature deformation was achieved after pre-strain at 650K by means of pin point compression explained in Figure 2-1. Microstructure of a deformed quasicrystal is shown in Figure 7-6. Slip bands were formed and several dislocations were observed in the bands as pointed by arrows. These slip bands were mostly formed on planes with the normal directed along a fivefold axis as identified by tilting experiments. From visibility criteria, Burgers vectors of dislocations in the band were determined to have a twofold direction in physical space as shown by a stereographic projection in Figure 7-7. The <twofold> {fivefold} slip systems are the ones mainly observed after high temperature deformation of icosahedral quasicrystals [17] [18]. Dislocation motion is, thus, shown to occur in the same slip system at both high and low temperatures. The morphology is, however considerably different and localized at a low temperature. This is possibly attributed to the phason strain remained after dislocation motion [19], which presumably makes the following dislocation motion easier and leads to fracture without exhibiting macroscopic ductility.

7.4. Conclusions

$Al_{65}Cu_{20}Fe_{15}$ icosahedral quasicrystal was deformed at lower temperatures by embedding it in Al_2Cu matrix by means of a semi-in-situ method. The results obtained are summarized as follows.

1) Dislocations accompanied planar defects on their paths at 550K and room temperature.

2) The lack of atomic diffusion induced local deformation prior to crack at room temperature, leaving slip bands.

3) The slip system operated at room temperature was confirmed to be the same as that reported for high temperature deformation.

References

[1] D. Schectman, I. Blech, D. Gratias and J. W. Carhn, Phys. Rev. Lett. **53** 1951 (1984).

[2] J. E. S. Socolar, T. C. Lubensky and P. J. Steinhardt, Phys. Rev. **B 34** 3345 (1986).

[3] T. Shibuya, T. Hashimoto and S. Takeuchi, Jpn. J. Appl. Phys. **29** L349 (1990).

[4] L. Bresson and D. Gratias, J. Non-Cryst. Solids **153&154** 468 (1993).

[5] F. Semadeni, N. Baluc and J. Bonneville, Proc. 6th Int. Conf. On Quasicrystals 513 (1998).

[6] M. Wollgarten, M. Bartsch, U. Messerschmidt, M. Feuerbacher, R. Rosenfeld, M. Beyss and K. Urban, Phil. Mag. Lett. **71** 99 (1995).

[7] S. Takeuchi, Mat. Res. Soc. Symp. Proc. **553** 283 (1999).

[8] M. Wollgarten, H. Saka and A. Inoue, Phil. Mag. **A 79** 2195 (1999).

[9] J. W. Cahn, D. Schectman and D. Gratias, J. Mater. Res. **1** 13 (1986).

[10] R. Wang and M. X. Dai, Phys. Rev. **B 47** 15326 (1993).

[11] J. Feng and R. Wang, Phil. Mag. Let. **69** 309 (1994).

[12] S. Takeuchi and T. Hashimoto, Jpn. J. Appl. Phys. **32** 2063 (1993).

[13] A. P. Tsai, Bulletin of the Japan Institute of Metals Materia Japan **39** 629 (2000).

[14] B.N. Dey and W. R. Tyson, Phys. Stat. Sol. (a) **9** 215 (1972).

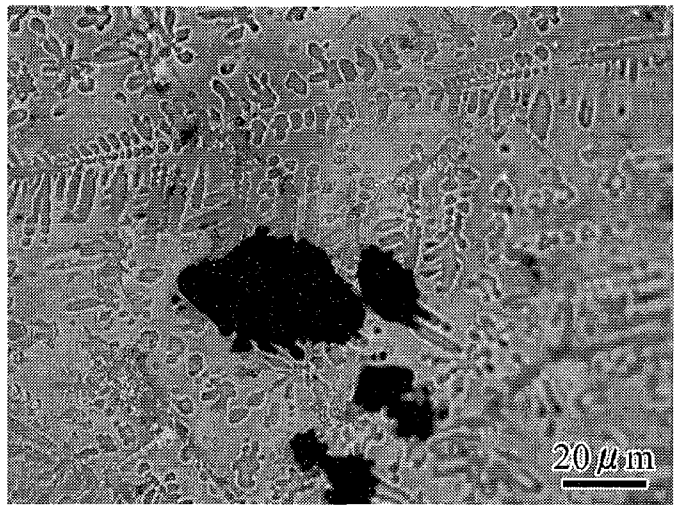
[15] C. J. McMahan, Jr., Advances in Materials Research volume 2, Microplasticity (Interscience Publishers, John Wiley & Sons Inc. 1968) p.121.

[16] R. Wang, M. Feuerbacher, W. Yang and K. Urban, Phil. Mag. **A 78** 273 (1998).

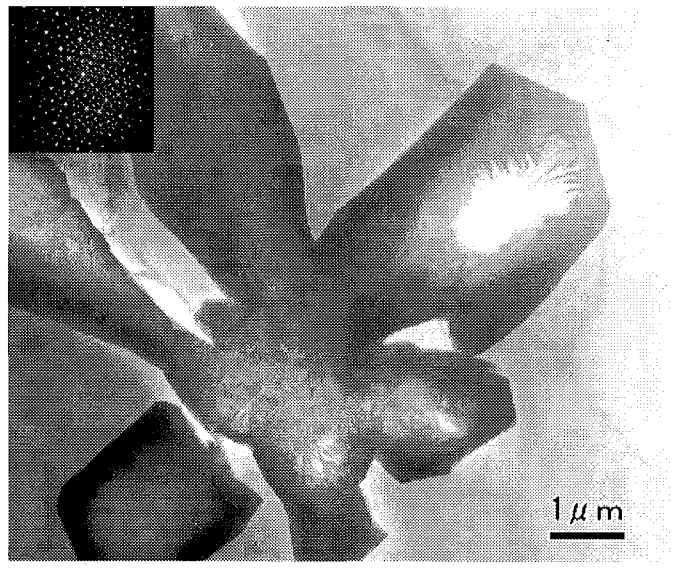
[17] J. Feng and R. Wang, Phil. Mag. **A 69** 981 (1994).

[18] R. Rosenfeld, M. Feuerbacher, B. Baufeld, M. Bartsch, M. Wollgarten, G. Hanke, M. Beyss, U. Messerschmidt and K. Urban, Phil. Mag. Lett. **72** 375 (1995).

[19] S. Takeuchi, K. Shinoda and K. Edagawa, Phil. Mag. **A 79** 317 (1999).



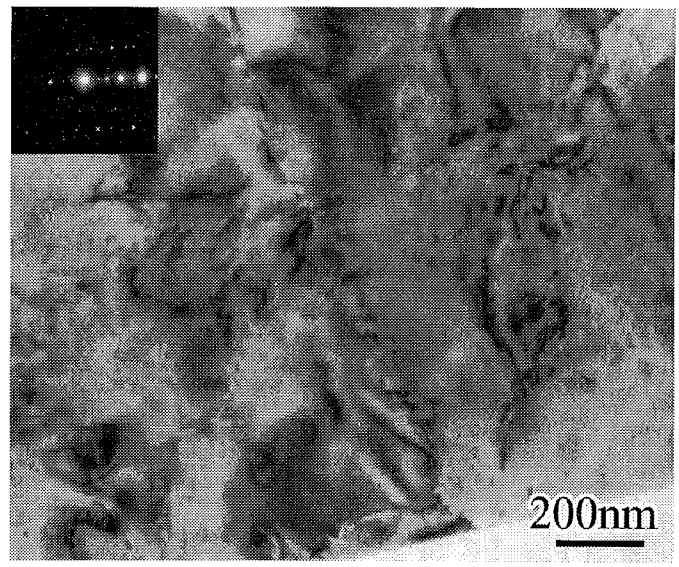
(a)



(b)

Figure 7-1

Optical micrograph (a) shows quasicrystals embedded in Al_2Cu matrix. A TEM micrograph (b) shows a quasicrystal surrounded by Al_2Cu viewed along the fivefold symmetry axis and the diffraction pattern. Microstructure of a quasicrystal particle was observed at a higher magnification in (c).



(c)

Figure 7-1

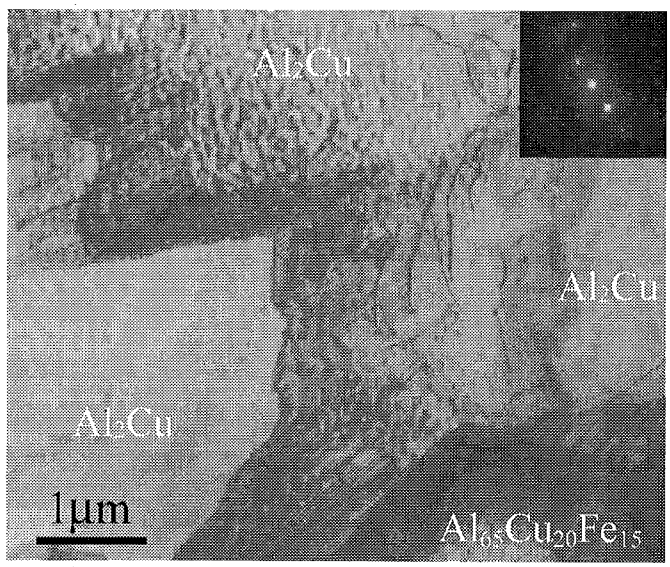
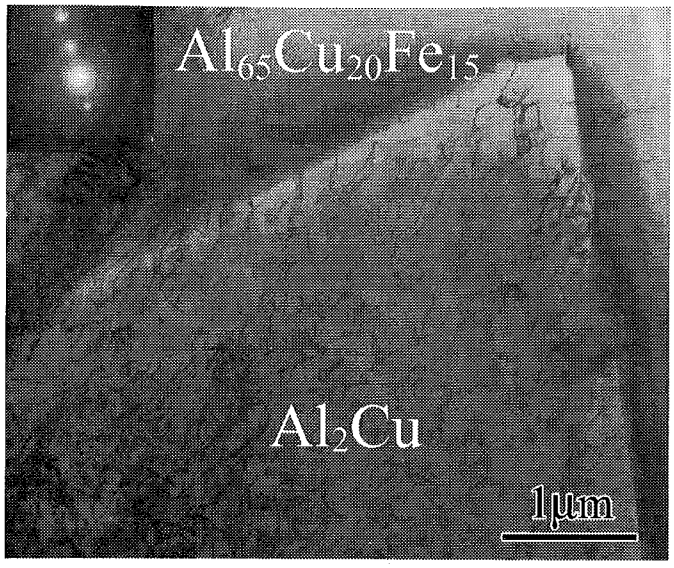
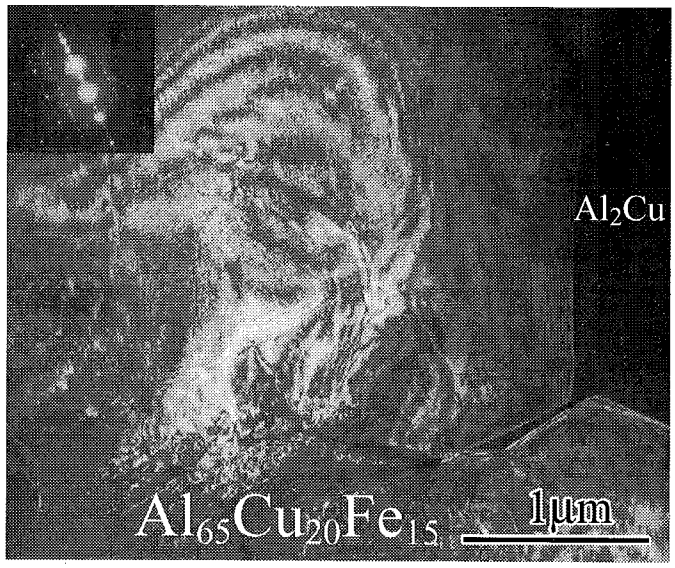


Figure 7-2

A group of dislocations are observed along small angle boundary in Al_2Cu matrix. Dislocations are absent inside the sub grains.



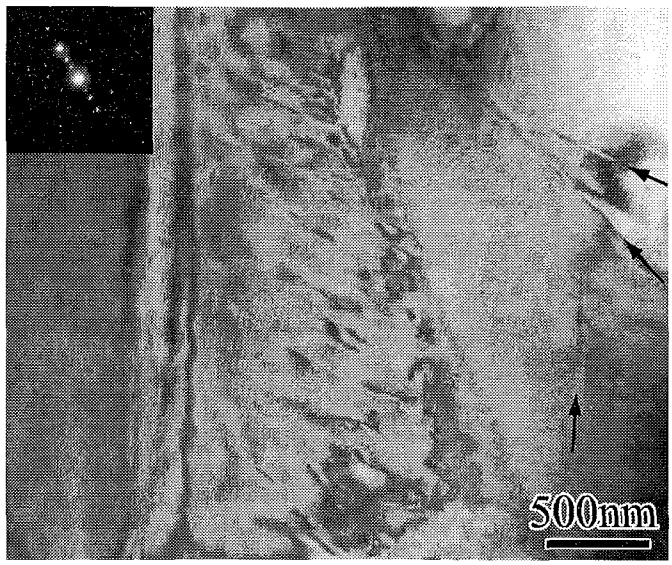
(a)



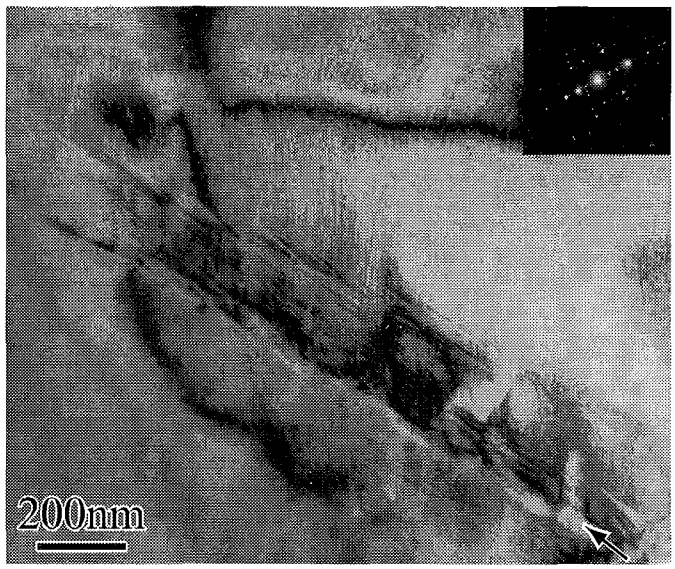
(b)

Figure 7-3

Al_2Cu matrix deformed at 650K contains a large number of dislocations distributed homogeneously inside a grain in (a). On the other hand, $Al_{65}Cu_{20}Fe_{15}$ quasicrystal in (b) showed local deformation at the roots of petal arms.



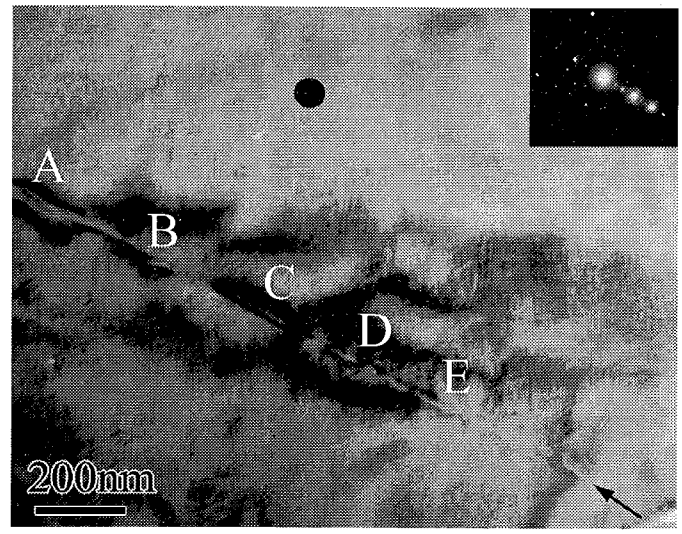
(a)



(b)

Figure 7-4

Tangled dislocations created in a quasicrystal deformed at 550K (a). Several planar defects having projection width of about 200nm are pointed by arrows was in (b). They disappeared in (c).



(c)

Figure 7-4

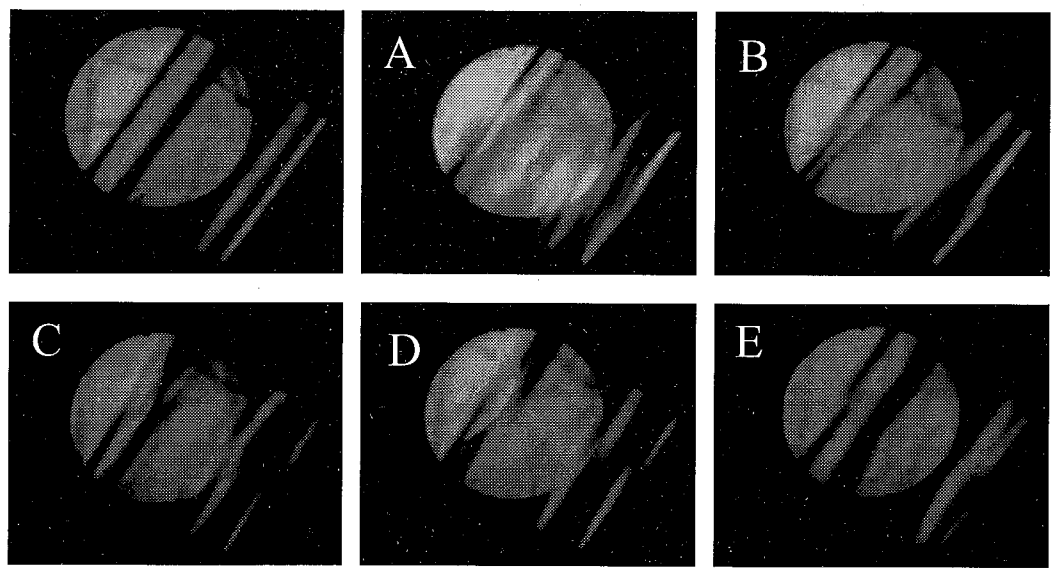


Figure 7-5

Five parts of a line contrast marked by A-E in (a) were examined by a CBED method. A small closed circle in (a) gives a beam size used to take CBED micrograph shown in (b). The first pattern in (b) was obtained from a defect free area. A-E corresponding to the five parts in (a) showed different types of twists: A and D showed the same type of twist but B and C showed opposite type of twist.

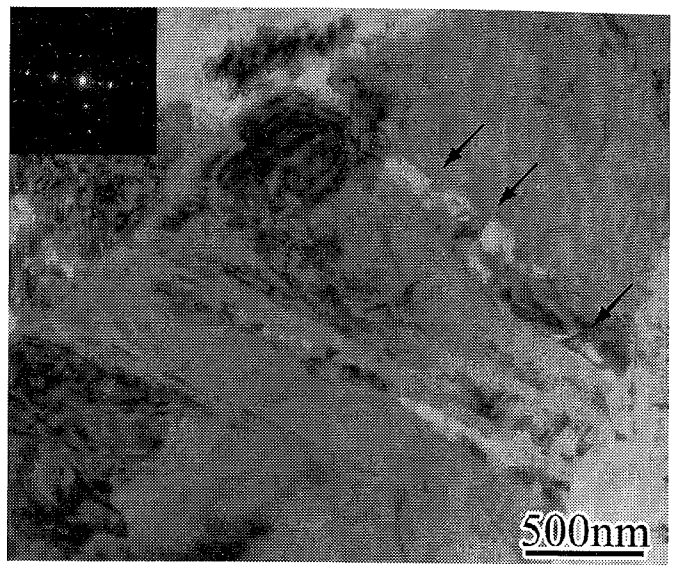


Figure 7-6

Slip bands in an $Al_{65}Cu_{20}Fe_{15}$ quasicrystal deformed at room temperature. Several dislocations are pointed by arrows in the slip bands.

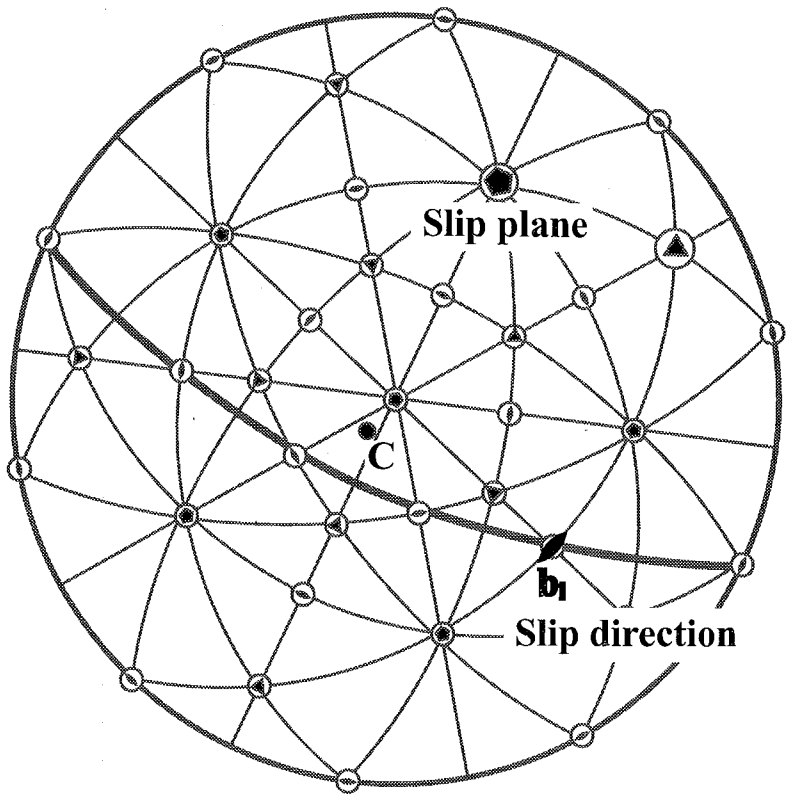


Figure 7-7

A stereographic projection showing an observed shear system after deformation at a room temperature. C (foil normal) shows a compression axis.

Chapter 8

Summary and Conclusions

In the present work, microstructure of the four high strength intermetallic compounds, namely Fe_3Ge, χ phase in Fe-Mn-Si alloy, $Al_{13}Fe_4$ and $Al_{65}Cu_{20}Fe_{15}$ quasicrystal, are investigated by means of transmission electron microscopy. The observations of the dislocations in the less ductile and hard specimens are made possible by development a special type of "semi-in-situ deformation method" and by using a composite material. The following description summarizes the accomplishments made in revealing the new facts about the plasticity of the hardly deformable materials mentioned above with the crystal structures, $L1_2$, $I\bar{4}3m$, monoclinic and quasicrystal lattices.

In chapter 2 entitled "Experimental procedures", the common parts of procedures in examining the four types of the hardly deformable materials are described with the particular focuses on the method of deformation and the analyses of the observations. The advantages in using composite materials and in applying the semi-in-situ compression tests are explained with detailed explanations of the apparatus and the newly developed skill for the thin foil compression. Also, the special TEM methods applied for the micro-structural analyses and the characterization of the complicated crystal structures are explained briefly.

In chapter 3 entitled "Dislocation motion on octahedral and cube planes in Fe_3Ge polycrystals", the mechanism of {001} slips in the $L1_2$ ordered Fe_3Ge was studied by means of bulk and thin foil deformation. According to the three-dimensional analyses of the dislocation structures and the Burgers vectors by visibility tests coupled with the equal thickness contour method and the CBED method, the {001} slips in the $L1_2$ ordered Fe_3Ge was verified to be responsible for absence of the anomalous temperature dependence in the temperature range from 77 K to 900 K with rapid decrease in the yield stress above 600 K. Furthermore, it was clarified that the sudden increase in the strain rate sensitivity above 600 K is caused by transition in the mechanism of the generation of the perfect <110> dislocations involving atomic diffusion, which is verified to involve climb of the <110>/2 partials above 600 K.

In chapter 4 entitled "Identification of the χ phase in Fe-Mn-Si based SMA and the estimation of its strength", the crystal structure of the hardly deformable phase introduced by the beating and heating of the SMA was determined to have a bcc based unit cell of $I\bar{4}3m$, called χ phase of the α-Mn type, by analyzing the ZOLZ and FOLZ micro diffraction patterns. Concurrently, the strength of the χ phase domain was estimated to be in the range of 3~5 GPa from the semi-in-situ deformation of a thin foil specimen and the introduction of the VN

precipitates into the Fe-Mn-Si based SMA was found to improve the ductility by proper combination of the high speed deformation and the heat treatment.

In chapter 5 entitled "Plastic deformation of Al-$Al_{13}Fe_4$ thin foils at room temperature", $Al_{13}Fe_4$ embedded in Al matrix was prepared and examined before and after the semi-in-situ deformation by a HVEM. The microstructure in the non-deformed state was examined carefully with a special interest on its change by the deformation. Partial dislocations with fine contrasts attached to planner faults and the twinned variants with the thickness up to a few μm were of the general constituents where the twinning planes were identified to be the three among the five types of the planes forming the pentagonal columns. The plastic zones were always observed along the mode II crack after deformation at 300 K and dislocations were introduced by the thin foil compression, but without leaving the individual dislocations capable for analyzing the Burgers vector.

In chapter 6 entitled "Dislocation generation and the motion in a monoclinic $Al_{13}Fe_4$ at 300~873 K", the monoclinic $Al_{13}Fe_4$ embedded in Al matrix was examined at different temperatures in the range 300 K ~ 873 K by means of the semi-in-situ compression of a thin foil specimen. The two types of experiments made to protect the specimen from cracking spontaneously, were to give a compressive stress on a thin foil specimen through a thin foil mental and through a sand paper, resulting in the success of determining the shear systems operated at 300 K, 673 K and 873 K as $[557](1\bar{1}0)$, $[110](001)$ and $[\bar{5}\ 15\ \bar{2}]\ (310)$, respectively. The dislocations were judged to be formed by a dislocation reaction involving atomic diffusion among the partial dislocations at 873 K, whereas the $[557](1\bar{1}0)$ and the $[110](001)$ types of dislocations were judged to be generated mechanically at foil surfaces under the high stress.

In chapter 7 entitled "Plasticity of an $Al_{65}Cu_{20}Fe_{15}$ quasicrystal embedded in Al_2Cu", the $Al_{65}Cu_{20}Fe_{15}$ icosahedral quasicrystal was deformed at the temperatures lower than 0.8 T_m by embedding the quasicrystal in the Al_2Cu matrix. The dislocations were found to accompany planar defects at 550K and room temperature in absence of the sufficient atomic diffusion, leading to the local deformation prior to the crack, confirming that the slip system operated at the low temperature is the same as the one reported in the literatures for the high temperature deformation apart from the residual phason strain.

Acknowledgement

I would like to express my deep gratitude to Professor Shinji Kumai, for his precious comments and hearty encouragement.

I am deeply grateful to Professor Masaharu Kato, Professor Yoshinao Mishima, Associate Professor Masanori Kajihara, Professor Susumu Onaka, Associate Professor Toshiyuki Fujii, and Research Associate Yoshisato Kimura, for their helpful comments and hot discussions in our group seminar.

I am indebted to Professor Naoki Yamamoto, for permitting me to use the HVEM for five years. The present thesis could not be made without the HVEM. I am grateful to Professor Yoshio Nakamura, for helping me when we hold an exhibition of the "Nano-World."

I am grateful to Dr. Natsuki Yoneyama, for his kind coach for using the HVEM. I have been running to get up to his place, but the way become longer than before.

Other persons to whom I owe this thesis are as follows:

Mr. Makoto Taniguchi (Toyota Mortar Co.)
Mr. Atsushi Kawachi (Sumitomo Steel Co.)
Ms. Yukiko Yamaguchi (Nippon Steel Co.)

Dr. Kenta Suzuki	Dr. Kwang-Jin Lee
Mr. Mitsuhiro Watanabe	Mr. Takeshi Ookawa
Mr. Hideyuki Futatsugi	Mr. Takeshi Miyazaki
Mr. Akira Mukaiyama	Mr. Akiko Ishihara
Dr. Noriko Kobayashi	Dr. Toshio Takenaka

Mr. Takashi Izumi (Fanuc Co.)
Members of our seminar group
Former members of our laboratory

I would like to express my deep gratitude to Emeritus Professor Akikazu Sato for his advice and guidance that made me to know a lot throughout my master and doctor courses. This work could have never been finished without his guidance.

Finally, I wish to express gratitude to my parents for their support not only economical but also mental. I promise to permit my future children to choose their ways of life, like my parents have done for me.

December 2005
Shinya Miyazaki

宮崎信弥